2017

Mechanics Of Colloidal Assemblies

Daniel James Strickland
University of Pennsylvania, dstric@seas.upenn.edu

Mechanics Of Colloidal Assemblies

Abstract

Amorphous solids -- solids that lack long-range order of their constituent particles -- are common in both nature and industry. Window glass, dense polymers, and food grains are three examples of amorphous solids familiar to us. In many amorphous solids, shear banding -- plastic deformation in which strain is accumulated in a thin band of the material -- is common. Consequently, many amorphous solids are brittle, a trait which has limited the technological adoption of otherwise promising materials such as metallic glasses. Therefore, a fundamental understanding of shear banding -- i.e., the progression from particle level plastic events to a macroscopic shear band, identification of the sites in the material from which shear banding is most likely to originate, the effect of structural modifications on shear banding, and mechanisms that arrest shear band operation before failure -- is crucial for predicting failure and engineering ductility in amorphous materials.

This dissertation describes efforts to illuminate elements of plasticity in amorphous solids using model systems of colloidal particles. The bulk of the results focuses on colloidal pillars subjected to uniaxial compression. Results from instrumented compression experiments reveal that the pillars exhibit a scaling of strength with stiffness that is similar to the scaling found in metallic glasses, which we interpret in the context of the energetics and kinematics of a critical shear band nucleus. In 4D \emph{in-situ} compression experiments we are able to observe the microscopic evolution of a shear band and the associated mechanical response in and around the shear band. The results from this experiment lend credence to the interpretation of shear banding as localized, anisotropic glass transition.

In addition to the pillar geometry, we perform confined compression experiments on a confined colloidal glass to investigate the structural fingerprints of the particles that are most likely to rearrange in an amorphous solid. The results from these experiments are interpreted in the context of a recently introduced machine-learning based approach to the identification of particles most susceptible to rearrangement termed "softness". We report preliminary application of softness to the shear banding pillars.

Degree Type
Dissertation

Degree Name
Doctor of Philosophy (PhD)

Graduate Group
Materials Science & Engineering

First Advisor
Daniel S. Gianola

Keywords
amorphous solids, colloidal mechanics, shear banding

Subject Categories
Mechanics of Materials

MECHANICS OF COLLOIDAL ASSEMBLIES

Daniel James Strickland

A DISSERTATION

in

Materials Science and Engineering

Presented to the Faculties of the University of Pennsylvania

in

Partial Fulfillment of the Requirements for the

Degree of Doctor of Philosophy

2017

Supervisor of Dissertation

_____

Daniel S. Gianola, Skirkanich Assistant Professor of Innovation

Graduate Group Chairperson

_____

David J. Srolovitz, Joseph Bordogna Professor of Materials Science and Engineering

Dissertation Committee
Zahra Fakhraai, Professor of Chemistry
Daeyeon Lee, Professor of Chemical and Biomolecular Engineering
David J. Srolovitz, Joseph Bordogna Professor of Materials Science and Engineering

To my dad and grandfather

ACKNOWLEDGEMENTS

I am indebted to a great many people who have, in one way or another, contributed to the completion of this dissertation.

Foremost, I thank my parents, Lynne and Robert Strickland, whose love, support, and sacrifices and support have afforded me opportunities for which I will always be grateful.

To my grandparents, Mary and Clyde Orr and Venus and Bud Turner, I thank you for all of your love and support. I am particularly grateful to my Grandfather Clyde Orr, who instilled in me from a young age an interest in the "way things work".

To my extended family – my aunts, uncles, and cousins – thank you for all of the love, support, and encouragement you've provided to both me and my parents.

To my dissertation advisor, Prof. Daniel Gianola, I thank you for fostering a graduate school experience with a unique combination of stimulating and challenging science and a collegial and fun environment. The joy you find in science and exploring the unknown is contagious.

To my lab mates – Lisa Chen, Kate Murphy, Brian Piccione, Mo-rigen He, Daniel Magagnosc, and Paul Shin – your consistent dedication to excellent research encouraged my best while your humility made the graduate experience enjoyable. I also thank Sasha Klebnikov for his contributions to the confocal experiments.

I thank the entire DISCONAP research group for the many useful suggestions I received over the course of my graduate experience. I thank Prof. Daeyeon Lee for lending his creativity and imagination to the advancement of my research. I am particularly indebted to Prof. Lee's lab members Lei Zhang, Yun-Ru Huang, and Jyo Lyn Hor for their patience with my many requests for samples. None of my experiments would have been possible without your assistance. I thank Prof. Andrea Liu, Prof. Doug Durian, and Dr. Jennifer Rieser for their insightful critiques of my work. I am also grateful to Dr. Carlos Ortiz, whose generosity in sharing his particle finding code and assisting me in its implementation greatly improved the analysis of the confocal experiments. I thank Robert Ivancic for numerous fruitful discussions.

I thank Steve Szewczyk for his generosity in lending his time, knowledge, and lab equipment, which contributed to almost all of my experiments. To Vicky Lee, Pat Overend, and Irene Clements, I thank you for everything that you do to keep the wheels of the MSE department turning smoothly and your unfailing smiles and kind words.

To my MSE colleagues – Spencer Thomas, Emmabeth Parrish, Cathy Yang, Rob Middleton, Nick Greybush, Frank Streller, Jacob Berger, Daksh Agarwal, Mike O'Reilly, Rob Ferrier, Vicky Doan-Nguyen, and Ted Trigg– thank you for making the

whole experience a lot more fun.

ABSTRACT

MECHANICS OF COLLOIDAL ASSEMBLIES

Daniel James Strickland

Daniel S. Gianola

Amorphous solids – solids that lack long-range order of their constituent particles – are common in both nature and industry. Window glass, dense polymers, and food grains are three examples of amorphous solids familiar to us. In many amorphous solids, shear banding – plastic deformation in which strain is accumulated in a thin band of the material – is common. Consequently, many amorphous solids are brittle, a trait which has limited the technological adoption of otherwise promising materials such as metallic glasses. Therefore, a fundamental understanding of shear banding – i.e., the progression from particle level plastic events to a macroscopic shear band, identification of the sites in the material from which shear banding is most likely to originate, the effect of structural modifications on shear banding, and mechanisms that arrest shear band operation before failure – is crucial for predicting failure and engineering ductility in amorphous materials.

This dissertation describes efforts to illuminate elements of plasticity in amorphous solids using model systems of colloidal particles. The bulk of the results focuses on colloidal pillars subjected to uniaxial compression. Results from instrumented compression experiments reveal that the pillars exhibit a scaling of strength with stiffness that is similar to the scaling found in metallic glasses, which we interpret in the context of the energetics and kinematics of a critical shear band nucleus. In 4D *in-situ* compression experiments we are able to observe the microscopic evolution of a shear band and the associated mechanical response in and around the shear band.

The results from this experiment lend credence to the interpretation of shear banding as localized, anisotropic glass transition.

In addition to the pillar geometry, we perform confined compression experiments on a confined colloidal glass to investigate the structural fingerprints of the particles that are most likely to rearrange in an amorphous solid. The results from these experiments are interpreted in the context of a recently introduced machine-learning based approach to the identification of particles most susceptible to rearrangement termed "softness". We report preliminary application of softness to the shear banding pillars.

TABLE OF CONTENTS

LIST OF TABLES

LIST OF FIGURES

Chapter 1
Introduction

Amorphous solids – solids that lack the long range order found in their crystalline counterparts – are both common in nature and technologically important[1]. Window glass, dense polymers, and food grains are three examples of amorphous solids familiar to us. The ubiquity of amorphous solids arises in part because they can be formed from a broad array of constituent particles. These particles span orders of magnitude in size, giving rise to a spectrum of amorphous solids with very different characteristic length scales and particle-particle interactions (see Figure 1.1). Two examples from the extremes of the spectrum are metallic glasses (MGs), which are composed of metallic elements (particle size of angstroms) that are disordered at the atomic scale, and a sand castle, which is composed of silica grains (particle size of microns) that are disordered at the granular scale.

Despite their abundance, a fundamental understanding of plasticity – or irreversible deformation – in amorphous solids remains elusive. While one may expect that the mechanisms underlying the deformation of an MG are completely unrelated to those underlying the deformation of a sand castle, there appears to be some similarity between the two. One piece of evidence for a connection between the mechanisms is that shear banding, or plastic deformation in which strain is accumulated in a thin band of the material, is a common mode of failure in both MGs and sand pillars

	atoms	nanoparticles	colloids	grains
	4 nm	200 nm	10 µm	3 mm
particle size	1-3 Å	1 - 100 nm	100 - 1000 nm	1 - 1000 µm
temperature	thermal	thermal	thermal	athermal
	metallic	Van der Waals capillary electrostatic magnetic solvation/depletion frictional steric	Van der Waals capillary electrostatic magnetic solvation/depletion frictional steric	capillary magnetic frictional steric

attractive / mixed / repulsive

Figure 1.1: From left, a $Zr_{59}Ta_5Cu_{18}Ni_8Al_{10}$ metallic glass alloy, whose disordered structure is evident in the transmission electron micrograph (image reprinted from Ref. 2 with permission). Next, an SEM image of an amorphous film of nearly-spherical, 25 nm TiO_2 particles (image reprinted from Ref. 3 with permission). Thermal effects are important in nanoparticle assemblies and, depending upon the solvent and colloid material, multiple types of particle-particle interactions may be present[4]. Third, a confocal micrograph of a colloidal glass composed of a mixture of 2.4 and 3.0 μm diameter poly-methyl methacrylate particles (image reprinted from Ref. 5 with permission). Colloidal particles are delineated from nanoparticles by their size; the particle-particle interactions found in nanoparticle systems are also present in colloidal systems. Finally, an image of an amorphous granular packing composed of mustard seeds (image courtesy of the Jaeger Lab, University of Chicago). In granular packings, the large particle size makes temperature unimportant.

(see Figure 1.2). Additional support is found in the intermittent stress fluctuations

observed in flowing MGs[6], foams[7], and grains[8] and the strain-softening behavior

observed in MGs[9], colloids[10], and granular materials[7]. While these observations alone

are not sufficient to conclude that the mechanisms underlying plasticity in amorphous

solids are universal, they do motivate researchers to search for commonalities.

In this Introduction, we will review the properties of glasses [1] and some observa-

---

[1]For brevity, the terms "amorphous solid", "disordered solid", and "glass" will be used inter-
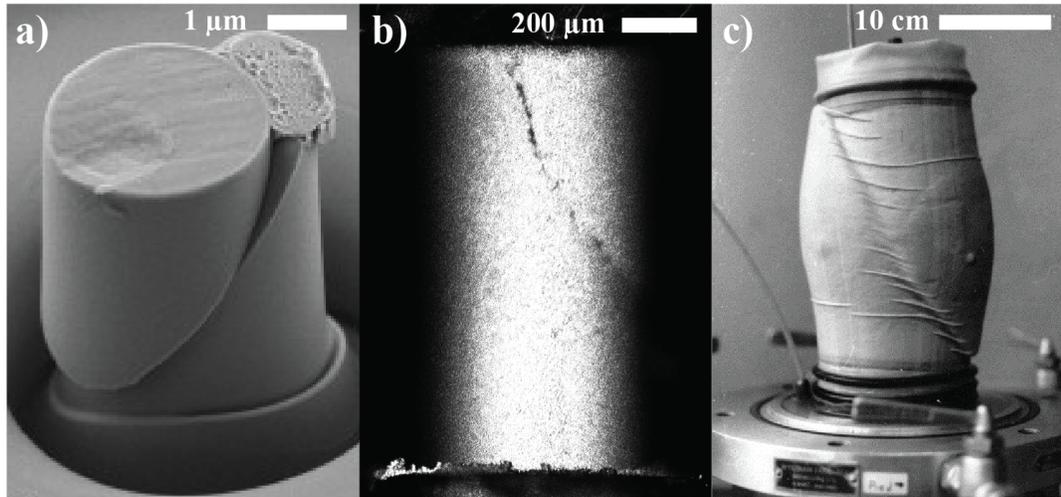
Figure 1.2: Shear bands developed in (a) a Zr-based metallic glass[11], (b) a colloidal micropillar[12], and (c) a sandstone pillar[13].

tions of universal behavior observed within this class of material, outline the current understanding of plasticity in amorphous solids with a focus on plasticity in MGs, and review the impact of model systems in advancing materials science. The findings and outstanding questions presented herein motivate the research that will be presented in this dissertation.

1.1. Amorphous Solids

Amorphous solids are solids in which the equilibrium positions of the constituent particles are disordered; that is, they do not lie on a translationally invariant lattice as they would in a crystalline solid[1, 14]. As mentioned previously, amorphous solids may

changeably. Technically, the term glass is reserved for an amorphous solid that has been formed by quenching the liquid melt[1].

be formed from many different types of constituent particles and prior research has shown that they share certain properties, irrespective of constituent particle type. We review several examples of commonality in behavior – often referred to as universality – below.

1.1.1. Glass Formation and Kinetics

When a liquid is cooled below the melting temperature, T_m, the liquid phase becomes thermodynamically unstable with respect to the crystal phase and the liquid is said to be supercooled[15]. Density fluctuations in a supercooled liquid are favorable nucleation sites for the lower-energy crystal phase and the system-spanning growth of these nuclei results in a first-order phase transformation from the liquid to a crystalline solid. Being first-order, this transformation is distinguished by a discontinuity in first derivatives of the free energy, such as the volume or entropy[16, 17].

However, if one cools the liquid quickly enough, crystal nucleation and growth can be suppressed and the supercooled liquid state can be maintained at temperatures well below T_m (see Figure 1.3). Further cooling results in a dramatic slowing of the particle dynamics, which manifests as an orders-of-magnitude increase in viscosity, and the material is said to undergo a glass transition[18–20]. Unlike crystallization, where there is a discontinuous jump in viscosity at T_m, viscosity changes continuously during the glass transition. Similarly, volume and entropy do not show a discontinuity as they do in crystallization, indicative that the glass transition is not a first-order

4

phase transition. Indeed, the glassy state may not be a thermodynamic transition at all but simply a kinetic constraint in which the dynamics of the particles are so slow that the material cannot equilibrate on laboratory timescales[21].
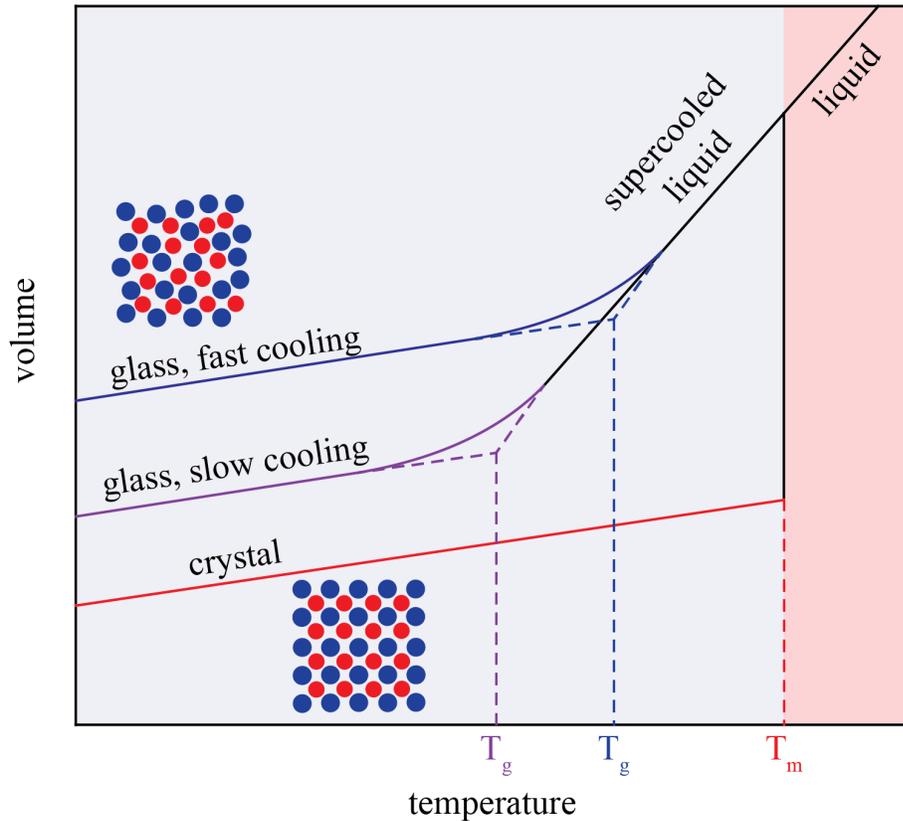
Figure 1.3: Routes to solidification from quenching the liquid melt. Crystallization is a first order transition marked by a discontinuity in the specific volume at the melting temperature T_m (red line). In glass formation, however, no such discontinuity is observed (blue and purple lines). As the cooling rate is reduced, the glass remains in equilibrium with the supercooled liquid to lower temperatures, resulting in a lower T_g.

Because glasses are out of thermodynamic equilibrium, their properties are history dependent[22]. This dependency can be readily seen by considering two glasses of identical composition cooled at different rates. The quickly cooled glass falls out

of equilibrium with the supercooled liquid at a higher temperature than the slowly cooled glass, resulting in a higher glass transition temperature, T_g [2]. In addition to the difference in T_g, the specific volume of the quickly cooled glass is larger than that of the slowly cooled glass at a given temperature. The discrepancies in T_g and specific volume highlight two points: T_g is not a thermodynamic quantity, as it may be varied by changing the formation protocol, and different processing techniques – the glass's history – result in different material properties. A fundamental understanding of the path dependence of glass properties is an ongoing effort [23–25], but we note that the increased "tunability" accessible via formation [26] and processing techniques [27, 28] opens exciting engineering opportunities for glass design and application.

The enormous slowing of dynamics that occurs during the glass transition in an atomic or molecular glass former has analogs in other types of thermal amorphous solids. In colloidal suspensions, a similar slowing of the particle dynamics is observed upon increasing the packing fraction from a dilute suspension [29, 30]. The sluggish dynamics are evident in both an increase in viscosity [29] and in direct measures of the particle mobilities [30]. Just like the glass transition, the increase in viscosity or decrease in mobility with increased packing fraction is continuous and there is no observable discontinuity in an order parameter. Foam is another example of an amorphous solid that exhibits glassy dynamics. Dense foams, which are mixtures of a gas phase in a fluid matrix [31], are known to behave as solids below a certain critical stress level.

---

[2]While there is no single convention to define T_g [19], a commonly used definition extrapolates the temperature-dependent specific volume in the supercooled liquid and glass phases and takes their intersection as T_g

Above this critical stress, they flow[32] and the relaxation time in the flowing regime has been shown to decrease continuously with increased stress[33] (the relaxation time is proportional to the inverse viscosity). In all of these cases – reducing the temperature of a glass-forming liquid, increasing the packing fraction of a colloidal suspension, and increasing the stress applied to a flowing foam – the relaxation time decreases continuously as the solid phase is approached. The continuity implies a critical point and has motivated attempts to unify the flowing-solid transition in what is known as the jamming transition[34, 35]. Jamming, the dramatic slowing in dynamics without an obvious structural transition, is an archetype of universality observed in many amorphous solids. Below, we review several other observations of universal behavior in amorphous solids.

1.1.2. Universal Behavior in Amorphous Solids

In addition to a continuous slowdown in dynamics, amorphous solids also exhibit an excess in the number of low-energy vibrational modes in comparison to the Debye model for crystals. Debye estimated the phononic contribution to a solid's heat capacity by considering the allowed vibrational modes for a periodic, repeating lattice of harmonic oscillators[36]. In Debye's model, the vibrational density of states (VDOS) for phonon frequency ω, $D(\omega)$, in three dimensions is given by:

$$D(\omega) = \frac{\omega^2}{2\pi^2 v_s^3}$$

7

where v_s is the velocity of the phonon. Experiments and simulations of various amorphous solids have found that the actual $D(\omega)$ is larger than what Debye's model would predict at low ω. In atomic glasses, these excess modes manifest as a plateau in the low temperature heat capacity[37] and can be observed in Raman scattering spectra[38]. In 2D packings of soft particles[39] and 3D colloidal glasses[40], $D(\omega)$ may be measured directly from real-space imaging of the particle positions. Again, both systems show an excess in the number of low-energy modes. Simulations of confined spherical particles that interact with a simple harmonic repulsive potential also exhibit this property[41]. The origin of the excess low-energy modes may be system-specific, but evidence suggests that density fluctuations intrinsic to the amorphous structure are responsible for this behavior. These density fluctuations lead to the localization of phonons, resulting in an excess number of low energy modes[42].

Another phenomenon observed in many glass-forming systems is so-called dynamical heterogeneity. Dynamical heterogeneity is the transient spatial variation in the local particle dynamics. For example, the displacement of a given particle may show sudden intermittent bursts in displacement followed by periods of little movement[43–45]. Another particle may move in a similar fashion, or move more frequently, or move not at all. One way to quantify the dynamics of a system is the self-intermediate scattering function, $F_s(k, t)$, given by[43, 46, 47]:

$$F_s(k,t) = \int G(r,t) \exp\left(-ikr\right) dr \tag{1.1}$$

8

with:

$$G(r,t) = \frac{1}{N} \sum_j \delta \left(r - [r_j(t) - r_j(t=0)]\right) \tag{1.2}$$

where k is the wavenumber and $r_j(t)$ is the position of particle j at time t. $G(r,t)$ may be interpreted as the probability that a particle has moved distance r in time t, and $F_s(k,t)$ is the Fourier transform of $G(r,t)$. $F_s(k,t)$ can be either directly measured using scattering experiments or calculated using real-space positions for individual particles. For a fluid, the form of $G(r,t)$ is well-approximated by a Gaussian:

$$G(r,t) = \frac{1}{(\pi^{3/2}W(t)^3)} \exp\left(-\frac{r^2}{W(t)^2}\right)$$

For times less than the timescale of collisions between particles, motion is expected to be ballistic and $W(t) = t\sqrt{2/\beta m}$. At long times, motion is expected to be diffusive, $W(t) = 2\sqrt{Dt}$, where D is the long time diffusion coefficient. Inserting this approximation into Equation 1.1 results in a scaling prediction for: $F_s(k,t) = \exp\left(-k^2 Dt\right)$. However, supercooled liquids and glasses show so-called "stretched exponential" behavior, where $F_s(k,t) = \exp\left(-t/\tau(k)\right)^{\beta(k)}$. Stretched exponential behavior is characteristic of glassy systems and a fingerprint of dynamical heterogeneity. For example, dynamical heterogeneity has been observed in an amorphous granular system upon the application of a shear stress. Similar to the aforementioned foam,

9

shearing the system induces flow and "unjams" the solid packing[48]. By tracking

particles directly, Dauchot et al. were able to determine $F_s(k,t)$. For length scales on

the order of the particle-particle distance ($k \sim 2\pi$), $F_s(k,t)$ indeed shows stretched-

exponential behavior at intermediate times. Because individual particle positions are

accessible in the experiment, Dauchot et al. were also able to calculate the four-point

correlation function – which measures correlation in motion over a set time window

between two points in the material – and find that the dynamics are quite heterogeneous

and spatially correlated[48]. Similar behavior has been found in a super-cooled colloidal

liquid where so-called "fast particles" – those with average displacements much larger

than the mean – are found to be spatially concentrated[30]. As the volume fraction is

increased towards the glass transition, the size of these concentrated regions decreases.

In sum, dynamical heterogeneity is observed in many glass-forming systems[43] and is

another example of a commonality observed in amorphous solids.

Furthermore, amorphous solids are known to exhibit stress fluctuations upon

yielding[49–51] and similar rheological behavior[52–55]. Taken as a whole, the many

manifestations of common behavior in amorphous solids suggest that at least some of

their properties emerge from the disordered structure itself and are relatively insensitive

to the details of the interactions between the constituent particles. Additionally,

universality propounds that the findings from studying one disordered solid may yield

insights that are applicable to other disordered solids. For instance, atomic solids,

which are challenging to study at the particle scale, may be modeled using systems of

larger, observable particles. With this in mind, we turn our attention to the manner in which amorphous solids permanently deform.

1.2. Plasticity in Amorphous Solids

In comparison to the aforementioned manifestations of universal behavior, commonalities in plasticity in amorphous solids of various length and energy scales remain relatively unexplored. First, however, it is informative to compare the deformation behavior of amorphous solids to the behavior of crystalline solids. The technological importance of crystalline metals made the study of crystalline plasticity an area of intense research in the early 20th century. Specifically, an understanding of the stress necessary to cause yield, or the onset of plastic deformation, was necessary to advance the design of alloys. Frenkel predicted the yield stress, $\tau_{y,ideal}$, of a perfect crystal by estimating the energy necessary to cooperatively shear crystallographic planes[56]. In Frenkel's model the shear stress, τ, to deform two crystallographic planes can be approximated as:

$$\tau = \tau_{max} \sin\left(\frac{2\pi}{a}x\right)$$

where τ_{max} is the peak shear stress, a is the lattice spacing of the crystal in the direction of shear, and x is the displacement of the sheared plane (see Figure 1.4). The displacement x can be rewritten in terms of the shear strain, $\gamma = \frac{x}{b}$, where b

is the lattice spacing perpendicular to the direction of shear. Assuming $a \approx b$ and $\gamma \ll 1$, τ can be rewritten as:

$$\tau = \tau_{max} \sin\left(\frac{2\pi}{a}x\right) \approx 2\pi\tau_{max}\gamma$$

Using elasticity, we can identify $2\pi\tau_{max}$ as the shear modulus, G, and arrive at an expression for the ideal shear strength as a function of G:

$$\tau_{max} = \tau_{y,ideal} \approx \frac{G}{2\pi}$$

Experimental strengths of crystalline metals, however, are found to fall orders-of-magnitude short of Frenkel's ideal strength, suggestive that plasticity results from mechanisms other than cooperative slip along crystallographic planes[57]. In real bulk crystals, microstructural defects, such as dislocations, grain boundaries, and surfaces, become active at stresses well below $\tau_{y,ideal}$, implying a transition to a far less cooperative plastic deformation mechanism. Controlling the character and number density of these defects mediates the strength of crystals; for instance, the Hall-Petch relationship for polycrystals[58][59] states that $\tau_y \sim d^{-1/2}$ where τ_y is the yield strength and d is the grain size (thus controlling the fraction of planar defects), and Taylor strengthening[60] predicts $\tau_y \sim \rho^{1/2}$ where ρ is the dislocation density. The ability to tailor material strength is a reflection of the large catalog of plastic events found

in crystals and the associated broad range of energies necessary for their operation. In such defected crystals, the highly cooperative shear mechanism that defines the intrinsic ideal strength is superseded by mechanisms that require the motion of only a few atoms (e.g., dislocation glide or climb), rather than the coordinated motion of many atoms.
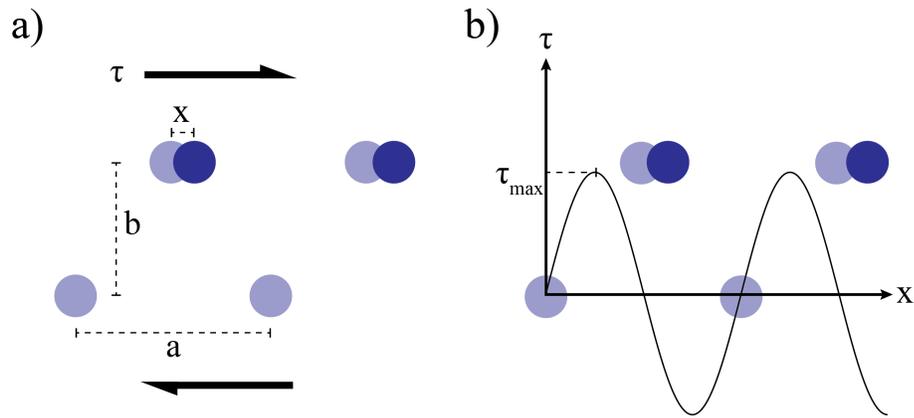
Figure 1.4: a) A shear stress applied to an ideal, defect free crystal with in-plane lattice spacing a and out-of-plane lattice spacing b results in a displacement x of the top plane. Displaced atoms are indicated by the dark blue circles. b) Frenkel's estimate of the shear stress required to generate a displacement x, which varies sinusoidally along the crystal lattice.

The situation is quite different in amorphous solids, where well-defined lattice defects like dislocations and grain boundaries cannot be identified[61]. Just as the increased industrial adoption of crystalline metals accelerated research on their mechanical properties, research on plasticity in amorphous solids has intensified with advancements in the formation of MGs. The first MG was created in 1960 by melt-spinning a Au-Si alloy[62]. In simple alloys like Au-Si, extremely high cooling rates are necessary to avoid crystallization. Melt-spinning, in which a stream of the liquid alloy

is dripped onto a cooled, rotating wheel, was one of the few techniques capable of generating the necessary cooling rates. However, the size and geometries of specimens that can be formed by melt-spinning are limited to extremely thin ribbons. A great advance came with the discovery of bulk glass formers, where the critical cooling rates needed to avoid crystallization are much smaller than those necessary in alloys like Au-Si[27, 63, 64]. These alloys, or BMGs, allowed for the formation of specimens millimeters or more in size, thereby opening new potential applications for MGs and invigorating research on their mechanical properties.

The unique properties of MGs make them attractive engineering materials. Like crystalline metallic alloys, MGs are stiff with typical values of the Young's modulus between 40-100 GPa[65]. However, the yield strengths of MGs approach Frenkel's theoretical limit ($\sim 0.025G$), which is an order-of-magnitude greater than the strength of most crystalline alloys[66, 67]. Some MGs also exhibit significant toughness, although this property is more sensitive to the MG alloy composition than yield strength is. For example, most iron-based MG alloys have a low toughness that is comparable to brittle ceramics, while zirconium-based MG alloys exhibit toughness values similar to tough crystalline alloys like steel[65]. MGs are also mechanically resilient; when loaded elastically, they dissipate very little energy[65]. This property makes MGs attractive materials for applications that require the storage of elastic strain energy, such as micro-scale resonators, springs, or actuators. Additionally, MGs have the capacity to be moulded using processes similar to those used to form oxide glasses[66, 68]. When

14

heated into the supercooled liquid regime, an MG behaves like a Newtonian fluid and can be formed into complex shapes using only small driving forces[69]. Upon cooling, the volume change in the MG is quite small, thereby allowing the solidified material to retain the shape of the mould[68]. Other desirable traits of MGs include corrosion resistance[65] and their magnetic properties[70]. However, because MGs often fail in a brittle, catastrophic manner at low temperatures, their adoption as structural materials has been limited[66]. Therefore, methods to design tougher glasses that can sustain significant plastic flow before fracture are needed to advance their practical usefulness. Rational design of toughness in an MG requires an understanding of its plastic behavior at the particle-scale, which we review in the subsequent sections.

1.2.1. Basic Phenomenology of Plasticity in Metallic Glasses

Partitioning a material's deformation behavior into flow regimes – elastic, plastic homogeneous, plastic heterogeneous, etc. – is useful for illuminating the plastic mechanisms that are dominant at different levels of applied stress, deformation rate, and temperature. For example, in crystalline metals, varying the temperature and strain rate induces transitions between dislocation glide, dislocation creep, and diffusional flow[71]. Deformation maps may be used to ascertain the activation energies of the underlying plastic mechanisms and guide rational material design principles. Like crystalline metals, the deformation behavior of MGs is also governed by the applied shear stress τ, the shear rate $\dot{\gamma}$, and the temperature T. The τ and T

dependence of the flow behavior is depicted in the deformation map in Figure 1.5. In the low temperature, low stress regime, where $T/T_g < 0.8$ and $\tau < 0.025G$, the behavior is elastic on laboratory timescales. For larger values of τ, yield occurs and strain localizes in shear bands. In this regime the yield strength decreases slightly with increased T and with increased $\dot{\gamma}$[9, 72, 73], although some alloys have been found to have a strain-rate independent strength[74]. At high temperature and low stress, plastic flow is homogeneous and may be either Newtonian ($\dot{\gamma} \propto \tau$) or non-Newtonian ($\dot{\gamma} \propto \tau^n$, where n is the stress sensitivity). The non-Newtonian regime is typically observed at $T < T_g$.
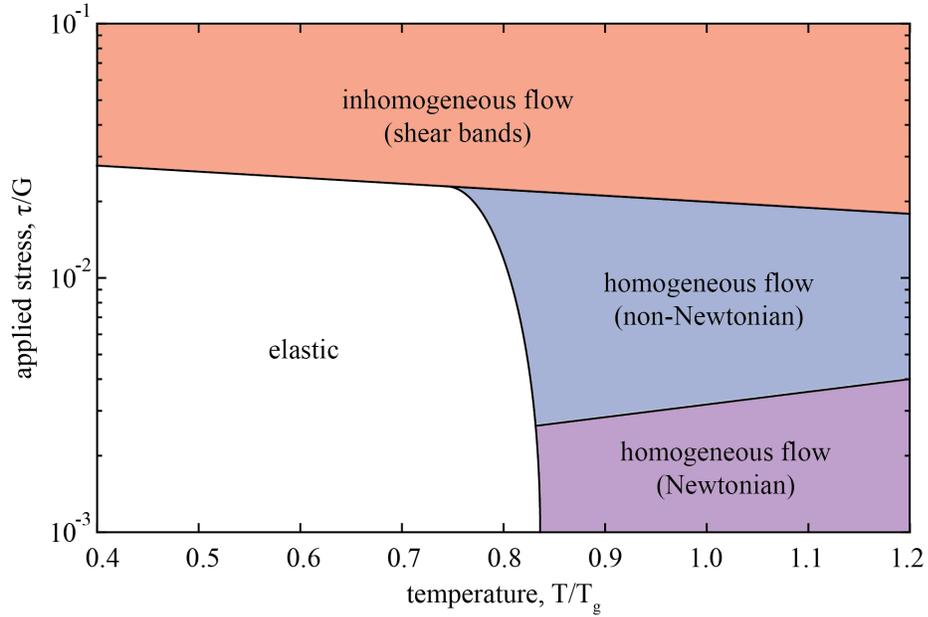
Figure 1.5: Following the review of Schuh, Hufnagel, and Ramamurty[66], the stress and temperature dependence of deformation in MGs. At low temperatures and low applied stress, the response is elastic (white region). At high levels of applied stress, deformation becomes inhomogeneous and manifests as shear bands (tan region). At high temperature and low levels of applied stress, the flow is homogeneous and the strain-rate dependence may be either Newtonian or non-Newtonian based upon the temperature and applied strain rate.

Two theoretical frameworks to explain the observed stress, temperature, and rate dependence of plastic behavior in MGs were put forth by Spaepen and Argon. In Spaepen's model, the underlying mechanism for plastic flow is envisaged as an individual atomic jump that is activated by an applied shear stress[75]. Following Polk and Turnbull[76], Spaepen assumed that these jumps create disorder at the atomic scale and generate an excess of local free volume. In Argon's model[77], the fundamental mechanism is the so-called shear transformation (ST), in which an applied shear stress activates the rearrangement of ∼100 particles. Like Spaepen's jumps, STs are dilatory – they result in increased local free volume – and generate a long-ranged elastic stress field in the surrounding glass. The enhanced local stress, which Argon modeled following Eshelby's solution for an inclusion in an elastic matrix, can trigger subsequent STs to operate.

Spaepen's and Argon's mechanisms share two common characteristics in that 1) they introduce excess free volume or disorder in the material and 2) they are thermally activated. The major difference between the frameworks is the nature of the fundamental plastic event, with Spaepen's atomic jump being discrete (involving only one atom) and Argon's STZ being the cooperative rearrangement of tens to hundreds of atoms. Computer simulations[78, 79] and model systems[80, 81] of amorphous solids that allow for direct observation of rearrangements support Argon's cooperative ST. In both models, a framework for thermally activated plasticity is used to connect the fundamental plastic event to macroscopic plastic flow. For a thermally activated

plastic process in which the activation energy is biased by an applied stress, the rate

of plastic events ω can be written as:

$$\omega = \nu \exp\left(-\frac{Q - \tau V}{k_B T}\right)$$

where ν is an attempt frequency on the order of the Debye frequency, Q is the energy

barrier of ST operation, τ is the applied stress, V is the activation volume of the ST,

k_B is Boltzmann's constant, and T is the temperature. Each plastic event results in a

characteristic strain, γ_o, so the strain rate, $\dot{\gamma} = \alpha \gamma_o \omega$, can be written as:

$$\dot{\gamma} = \alpha \gamma_o \nu \exp\left(-\frac{Q - \tau V}{k_B T}\right)$$

where the prefactor α is of order 1 and accounts for geometrical factors. Because STs

have a direction – they can operate both forwards and backwards – we can write the

net forward rate as:

$$\dot{\gamma} = \alpha \gamma_o \nu \left[\exp\left(-\frac{Q - \tau V}{k_B T}\right) - \exp\left(-\frac{Q + \tau V}{k_B T}\right)\right]$$
$$= \alpha \gamma_o \nu \exp\left(-\frac{Q}{k_B T}\right) \sinh\left(\frac{\tau V}{k_B T}\right) \quad (1.3)$$

The flow rate given by Equation 1.3 can be be used to separate the deformation map

into the homogeneous and inhomogeneous flow regimes whose boundaries are set by the competition between the free volume created by an atomic jump and the free volume annihilated by diffusion. In the homogeneous regime, the rate of free volume annihilation is equal to the rate of free volume production, and localized, runaway softening does not occur.

The Newtonian and non-Newtonian behavior is evident upon consideration of the small and large-stress limits of Equation 1.6. When $\tau \ll k_B T/V$, $\sinh(\tau V/k_B T) \approx \tau$), so:

$$\dot{\gamma} = \alpha \gamma_o \nu \exp\left(-\frac{Q}{k_B T}\right) \tau \qquad (1.4)$$

and $\dot{\gamma} \propto \tau$, which is Newtonian behavior. When $\tau \gg k_B T/V$, $\sinh(\tau V/k_B T) \approx \exp(\tau V/k_B T)$, and:

$$\dot{\gamma} = \alpha \gamma_o \nu \exp\left(-\frac{Q - \tau V}{k_B T}\right) \qquad (1.5)$$

which essentially eliminates the "backwards" operation of STs. Here, the flow is non-Newtonian as $\dot{\gamma} \propto \exp\left(-\frac{Q-\tau V}{k_B T}\right)$.

The boundary between homogeneous and inhomogeneous flow may also be constructed by setting an equivalency between the strain rate due to the nucleation of a critical shear event and the steady state strain rate given by Equation 1.3. Argon

estimated the strain rate of the nucleation event as:

$$\dot{\gamma} = \dot{\gamma}_s \exp\left(-\frac{C_s \tau_s \Omega_s \left(1 - \frac{\tau}{\tau_s}\right)^2}{k_B T}\right) \tag{1.6}$$

The expression in the numerator of the exponent in Equation 1.6 is determined from the maximum in the enthalpy for nucleating a loop in an elastic solid of radius R, where $\Omega_s = a\pi R^2$ is the volume of the loop and a is the loop thickness.

While these phenomenological expressions are useful in broadly delineating flow regimes, they often break down when applied to real specimens. For example, specimen size, internal structural variations, and stress gradients are all known to significantly alter the morphology of plastic deformation within the inhomogeneous flow regime[28, 66]. To make further progress, one must understand the nascent stages of shear banding – nucleation – and the growth of a shear band nucleus into a macroscopic shear band.

1.2.2. Nucleation of Shear Bands

After identifying the building blocks of plasticity in MGs, one must connect the operation of individual STs to macroscopic plastic flow. It is widely believed that shear band formation is a nucleation event. This assertion rests on the strain rate and temperature dependence of the shear band generation rate, which is found to increase with increased strain rate and increased temperature[82] as would be expected

in transition-state theory (see Equation 1.6). If shear banding is a nucleation process, two related questions arise: from where do shear bands nucleate and, after nucleating, how does the nucleus grow into a macroscopic shear band?

We turn first to the question of where nucleation originates in MGs. In crystalline metals, it is known that vacancies[83], grain boundaries[84], surfaces[85], and other defects are favorable nucleation sites for dislocation loops. Their favorability is a result of the lower energy barrier that must be overcome to form a dislocation loop at a defect, which is termed heterogeneous nucleation, in comparison to the energy barrier for homogeneously nucleating a loop in the bulk crystal[83, 86]. Modification of the population of nucleation sites in crystalline metals can be used to alter their strength and ductility. For example, the reduction in heterogeneous nucleation sites that accompanies a reduction in sample size is responsible for the extremely high strengths observed in nano-scale crystals[85, 87–89].

In a disordered material, where defects are not well defined, the categorization of nucleation sites is not straightforward. Zhao et al. introduced a framework to classify nucleation sites in disordered materials based on the concept of "connected atomistic free volume" (CAFV)[90]. CAFV quantifies the extent and connectivity of atomic coordination with respect to the perfect crystal. For example, the CAFV spectrum in a crystal, which is illustrated in Figure 1.6, consists of delta functions at 0 for perfectly coordinated particles, $-12\mathring{A}^3$ for interstitial defects, and $12\mathring{A}^3$ for vacancies. Extended defects like dislocation loops and grain boundaries have smooth distributions at larger

values of CAFV. In a disordered structure, the delta functions at small CAFV are replaced by a continuous distribution. Below a cutoff volume on the order of the vacancy CAFV, the CAFV spectrum is referred to as "intrinsic heterogeneity" and is a direct result of the disordered structure. CAFV larger than a vacancy is termed "extended heterogeneity". Just as in crystalline materials, modification of an MG's CAFV distribution can be used to tune its mechanical response; these techniques will be explored further in Section 1.2.4.
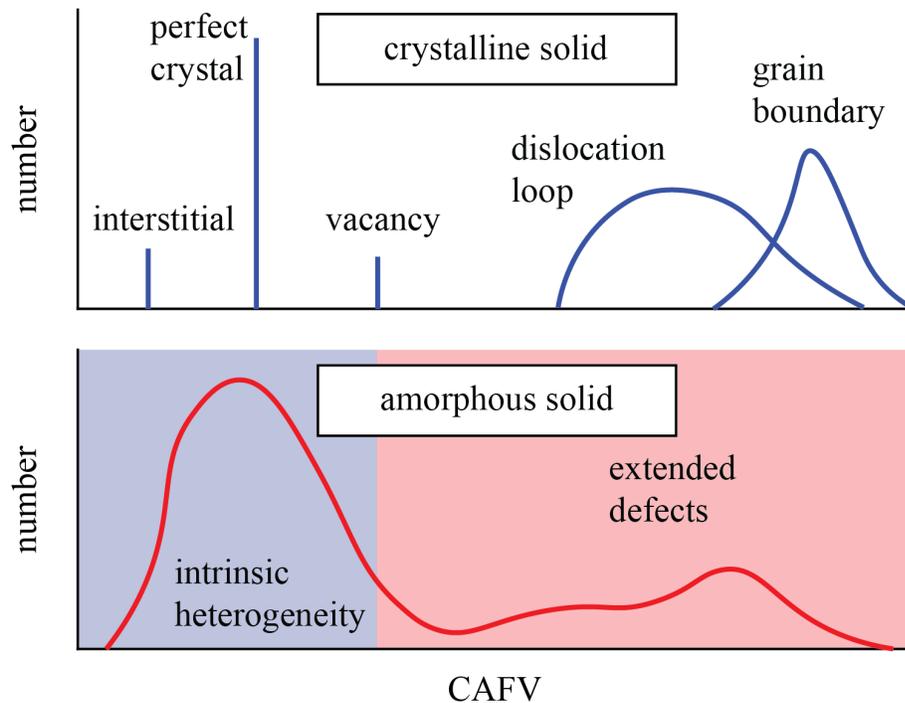
Figure 1.6: Following Zhao et al.[90], classification of defects in crystal and glasses according to their connected atomistic free volume (CAFV). In crystals, the defect spectrum consists of delta functions with well-defined characteristic CAFV. In glasses, the spectrum is smooth, reflecting the wide-range of local atomic structures in the amorphous state. The CAFV spectrum below the size of a crystal vacancy arises from intrinsic heterogeneity in the glass structure. Larger defects are associated with flaws such as voids, shear bands, and surfaces.

Within the intrinsic heterogeneity spectrum of a glass, the identification of flow defects – structural motifs that are most likely to rearrange under an applied stress – *a priori* has been an intense area of research[91–95]. The free volume approach to flow defect identification, in which local volume is compared to a reference structure such as the crystal or the density of the ideal hard-sphere glass[96], has proven to be a poor predictor of rearrangements[95, 97]. An alternative approach uses a Voronoi-index as a measure of the local structure[92–94]. In simulations of MG alloys, the packing's structure is tesselated using Voronoi's method[98, 99] and the resulting polyhedra are classified by counting the number of faces with a certain number of edges; i.e. for the Voronoi-index convention $< n_3, n_4, n_5, n_6 >$, the vector $< 0, 0, 12, 0 >$ indicates a polyhedron with 12 pentagonal faces[100]. Sheng et al. and Cheng et al. find a strong correlation between local atomic mobility and structure: particles with a local structure of $< 0, 0, 12, 0 >$ are found to compose a majority of the "slow" particles in the system while "geometrically unfavored motifs", or GUMs, like $< 0, 3, 6, 1 >$ and $< 0, 2, 8, 0 >$ polyhedra, are more mobile than the average. Other approaches that have been used to identify flow defects include local measures of the equilibrium stress[101, 102], elastic modulus[103], or yield stress[104]. As a whole, these structural approaches to defect identification have shown varied levels of success in their predictive capabilities[95] and appear to be strongly system-specific.

Alternative frameworks to the exclusively structural methods of flow defect identification incorporate knowledge of the particle dynamics along with structural

information. One approach links flow defects to the particles that participate most in low-energy vibrational modes[105–107], where a strong correlation is found between a particle's participation ratio in these modes and its likelihood to rearrange under shear. However, because determination of the particle-particle interactions in experimental systems is often challenging, the vibrational analysis is difficult to apply in laboratory settings. A second approach incorporates the particle dynamics, as quantified by the mean squared displacement, $\langle r^2 \rangle$, along with structure[97] in the so-called flexibility volume. The flexibility volume is defined as $v_f = \langle r^2 \rangle a$, where a is the average atomic spacing. The quantity v_f proves to be a robust predictive metric for the shear modulus G in many different MG alloys and also correlates strongly with rearrangements, whereas free volume alone does not. An added benefit of this approach is that v_f can be accessed experimentally at the macroscopic scale[97] through scattering measurements.

Recently, a new exclusively-structural predictive framework that leverages advances in machine learning has proven to be very effective at identifying flow defects[108–110]. Here, a particle is first characterized by M measures of its local environment at a time t. These M measures, which encode radial density and bond-angle information, constitute a vector in an M-dimensional space. Next, a measure of local plasticity is chosen to identify particles that rearrange in a time window between t and $t + \Delta t$. Finally, the particles are segregated into two groups: particles that exceed a threshold in the plasticity measure are labeled "soft" and particles with

plasticity below this threshold are labeled "hard". Using a support vector machine, the hyperplane that best separates the two classes of particles is found. The distance of a particle from the plane in this hyperspace is defined as its "softness", with positive softness reserved for the soft side of the hyperplane. Once the hyperplane is found, softness can be applied to particles whose future plastic activity is unknown. Softness proves to be a powerful predictive metric as soft particles are found to have a 90% probability of rearranging[109]. Additionally, softness has proven an excellent predictor of system dynamics in both the super-cooled liquid[109] and glass[110] regimes. The correlation between softness and dynamics has proven robust, and the application of softness to studying plasticity is a promising avenue for future study.

Flow defects are the most favorable sites for ST operation, and therefore the most likely site for shear band nucleation. However, not all STs result in a shear band; indeed, it is well known that STs are active well below the macroscopic elastic limit[111–113]. The progression from an individual ST to a critical shear band nucleus remains poorly understood, but the current understanding is that the initial ST triggers other STs in its vicinity through elastic interactions[82]. This clustering of STs proceeds until the nucleus reaches a critical size and then transitions to directed growth along directions of high shear stress. The size and shape of the critical nucleus are not firmly established. Experimental evidence suggests that the critical nucleus size in an MG is 10^7 times larger than the size of an ST[82]. Moreover, modeling of shear band nucleus growth highlights the role of applied stress: at a critical level of stress,

runaway nucleus growth, which is modeled as an oblate spheroidal inclusion in an elastic matrix, becomes thermodynamically favorable[114]. This transition is extremely sharp with respect to the applied stress. Propagation continues until the shear band is arrested by an obstacle or there is a sufficient reduction in the driving stress. The length and time scales associated with this propagation in MGs are extremely small, thereby making experimental studies quite challenging. Therefore, the structural changes, operating temperatures, and interactions of these propagating bands – all properties that are critical for devising methods to arrest this runaway process – have been a recent experimental and theoretical focus.

1.2.3. Propagation of Shear Bands

Once a shear band has nucleated, be it homogeneously or heterogeneously, continued applied stress causes the nucleus to grow into a macroscopic shear band. While this growth process remains poorly understood, several models of shear band operation have been proposed. In Shimizu et al.'s ARGL model, an operating shear band has four distinct regions: a liquid region at the rear of the band, a glue region, a rejuvenated region, and an aged region in front of the band[115, 116]. In the liquid region, the friction generated by shear results in temperatures above T_m and negligible resistance to flow. In the glue region, shear has also increased the temperature but it remains below T_g. Therefore, the glue region is more viscous that the liquid region and provides significant resistance to flow. The rejuvenated region remains at ambient

temperature but shear has generated structural disordering. The aged region in front of the band is undeformed and behaves elastically. An alternative model proposed by Cao et al.[117] envisages the shear band growth process in only two stages: 1) the operation of STZs along a system-spanning band of material which induces structural rejuvenation followed by 2) sliding along this rejuvenated path. In the two-stage model, the temperature in the rejuvenated path prior to sliding need not increase above T_m.

Experimental evidence has shown that the extreme temperatures associated with the ARGL are not necessary for shear band formation. While deformation experiments coupled with methods to measure temperature have confirmed heat generation during shear deformation[118, 119], this heating is often generated by sliding during fracture and not shear band formation itself. Indeed, compression experiments performed with an extremely stiff loading apparatus show that shear band formation need not generate a temperature rise at all[120], a finding in direct contradiction to the ARGL model. Additionally, compression experiments recorded with high speed video[121] reveal that a shear offset forms simultaneously across the entire sample, which is also in conflict with the ARGL model's propagating shear front. Indentation experiments on several MG alloys have also revealed that shear bands do not form at the point of maximum shear stress but instead develop along a path in which the stress exceeds a critical value[122], further supporting the propagating rejuvenation proposal of the "two stage" model.

During the propagation stage of shear banding, significant structural evolution occurs within the band. Simulations have shown that this evolution includes dilation[115, 117, 123], the preference for higher-energy atomic structures[124], and reduced atomic ordering[125]. Experimentally, electron and neutron diffraction[126, 127] have been used to probe structural change in shear bands in MGs. Here, a shift in the position of the first peak in the radial distribution function indicates volumetric dilation. Moreover, the evolution of radial distribution function at larger length scales actually indicates that certain atomic spacings are actually *over-coordinated* with respect to the undeformed glass, which is indicative of significant anisotropy in the structure induced by deformation. This finding is similar to the structural changes observed in sheared colloidal glasses[128, 129]. As discussed in Section 1.1.2, the jamming framework recognizes that both stress and temperature affect the rheology of an amorphous solid. Therefore, one may ask whether mechanically induced flow – shear banding – and thermally induced flow – the glass transition – share common structural and dynamical properties. In MGs, support for such a connection is founded in the fact that the energetics of the thermally activated β-relaxation and ST operation are almost identical[130, 131], although the length-scale and kinematics of the β-relaxation are not firmly established[132]. In an extension of this equivalency, Liu et al. predicted a scaling of the yield strength with temperature by equating the mechanical work done in the formation of a shear band and the heat necessary to induce a glass transition[133]. A derivation of this model accounts for the MG's structural state, as quantified by the

fictive temperature (see Section 1.2.4 for details), to describe the processing dependence of the yield strength[134]. Further support for a mechanical yield/glass transition connection is found in the self-similarity of iso-viscosity curves with proximity to the glass transition and magnitude of applied stress[52–55], which is suggestive of an equivalence between the glass transition and stress required for flow. However, the studies in Refs. 52–54 do not specify whether plasticity is spatially homogeneous or localized in shear bands, and other studies draw a distinction between shear banding and the glass transition. In experiments on a sheared colloidal glass, Chikkadi et al.[135] find a discontinuity in a dynamical order parameter that distinguishes shear banding from a glass transition, in which the dynamics of the latter vary continuously[18]. Similarly, a structural order parameter that segregates pre- and post-yield glasses classifies mechanical yield as a first-order transition[136]. Others have delineated between the glass transition and mechanical yield by contrasting the microstates induced by strain and increased temperature[137] and anisotropy of dynamical correlations[138], which are different for the thermal and mechanical transitions. While it appears that mechanical yielding in disordered solids shares at least some characteristics with the glass transition, the extent of the correlation is not yet agreed upon. Furthermore, the microscopic details of shear bands as they mature to macroscopic localization have yet to be elucidated.

One unambiguous attribute of shear bands is that they are responsible for catastrophic failure in MGs and, consequently, render MGs more brittle and less tough

than their crystalline counterparts. Accordingly, methods for controlling the density of nucleation sites and pre-existing shear band density underpin state-of-the-art methods for toughening MGs.

1.2.4. Strategies for Toughening Metallic Glasses

A material's toughness is defined as the amount of energy it can absorb before fracture[57]. While crystalline metals generally yield at lower levels of stress than MGs, their intrinsic hardening mechanisms allow for them to accumulate significant plastic strain before fracturing[139]. In MGs, STs cause local softening which results in unstable, catastrophic fracture soon after yield. Therefore, MGs are typically less tough than crystalline metals[66]. However, MGs do have the capacity for plastic flow, so routes to engineer toughness appear feasible[113]. Here, we review approaches to enhance the toughness of MGs. Broadly, we separate the toughening strategies according to the part of the CAFV spectrum – intrinsic or extended heterogeneity – that they modify.

First, we focus on toughening strategies that modify an MG's intrinsic structure without introducing extended defects. The toughness of MGs is alloy-specific; alloys with a small ratio of G/B, where B is the bulk modulus, are generally tougher[140]. This trend has been explained in the context of the material response around a crack tip: in MGs that are less resistant to shear (low G/B), shear band propagation is more favorable than crack tip opening. By suppressing crack opening, fracture can be avoided[141]. However, the G/B ratio alone cannot explain why thermal processing of an

MG alloy can significantly alter its toughness without affecting G/B[142]. Apparently, toughness is also sensitive to the details of the intrinsic structure. While the intrinsic structure of a glass is difficult to quantify in a single state variable, the "fictive temperature," T_f, has been widely used to quantify its thermomechanical history. Briefly, a higher T_f reflects a more "liquid-like" state. Bending experiments performed on multiple MG alloys with different T_f's reveal that the strain before failure increases for specimens with high T_f, although the extent of the increased ductility is alloy-specific. The underlying reason for the increase in ductility remains unclear – are STs in the high T_f state more diffuse spatially, thereby leading to more diffuse shear bands? Other strategies used to impart intrinsic toughness modify the triaxiality or heterogeneity of the stress state in the glass. Recent experiments have demonstrated that MGs actually have the capacity for strain hardening. In a notched MG pulled in tension, the deformed notched region actually shows an increase in hardness in comparison to the as-cast glass[143]. This hardening is attributed to diffusion-like structural relaxation, which is presumably promoted by the large component of hydrostatic stress in the notch. More evidence for hydrostatic stress-driven relaxation is found in indentation experiments. Here, an indenter imparts a static load on an MG in which the peak stress is below the yield stress. After unloading, the hardness of the glass is increased[111]. Increasing the stress heterogeneity has also been shown to impart ductility in MGs. MGs subjected to cryogenic temperature cycling, in which a specimen is repeatedly heated and cooled between room temperature and $77K$,

possess large spatial fluctuations in the residual stress concentrations[144]. The stress is caused by spatial heterogeneity in the thermal expansion coefficient, which results in significant non-affine strains during temperature cycling. The cryogenically-cycled specimen can withstand 5% plastic strain before fracture[28], which is a significant increase in comparison to the as-cast glass.

The population of extended defects may also be used to tune the toughness of MGs. Extended defects can both seed and arrest shear band operation. Some extended defects alter the stress state in the glass. For example, surface roughness can be envisaged as many particle-scale notches that, like macroscopic notches, increase the stress triaxiality. Computer simulations show that ductility is enhanced in nano-scale MGs where the surface roughness becomes a significant fraction of the specimen size[145]. While strain hardening is not observed in this work, the large hydrostatic tensile stress appears to make a larger fraction of the specimen available to plastic flow. Additionally, the large stress gradients near the surface arrest shear band propagation before the band becomes system-spanning. The population of extended defects can also be modified by processes such as high energy electromagnetic or ion irradiation and mechanical treatments like cold-rolling or shot-peening[28]. Ion irradiation of nano-scale MG wires has been shown to impart enhanced ductility[134, 146]. This effect was analyzed in the context of increased fictive temperature induced by the irradiation. Extended defects introduced by cold-rolling an MG have also been shown to increase ductility[147, 148]. Here, geometrical constraints during the cold-rolling process allow for

the generation of extreme amounts of plastic strain without fracture and the creation of a large number of shear bands. These pre-existing shear bands are reactivated under applied stress but their propagation is hindered by the hard, un-deformed matrix, thereby preventing them from becoming system spanning. Mechanical treatments like cold rolling introduce a directionality to the material because the shear bands they generate form along preferred directions[113]. When the processed material is subjected to load, the orientation of the load with respect to the pre-existing shear bands determines the mechanical response.

Processing methods that modify the intrinsic or extrinsic defect population in MGs have proven effective at enhancing toughness. However, in many cases – such as ion irradiation and cryogenic cycling – the structural modifications are subtle, difficult to measure, and the direct connection between structural alteration and shear band nucleation remains mysterious. To this end, model systems – where particle scale structure may be measured directly – may advance our understanding of the relationship between structural modification and incipient plasticity in glasses.

1.3. Model Systems

Great advances in imaging instrumentation have been made over the past century. The development of the transmission electron microscope[149, 150] and the atomic force microscope[151] have allowed researchers to visualize materials with atomic resolution. Powerful diffraction techniques are now capable of measuring spatially-varying strain

fields in nano-scale specimens[152, 153]. However, despite these and numerous other advances, the ultimate goal of resolving the position of every atom in a material and monitoring atomic displacements upon the application of some external field remains outside the capabilities of current technology. Therefore, model systems have been and remain a crucial tool in guiding and confirming our understanding of atomic solids.

Model systems have several beneficial properties. In many cases, the exact locations of particles in a model system may be determined directly. This capability is a huge advantage in comparison to atomic systems, where the techniques necessary for atomic-level imaging may be impossible or impractical and where diffraction or scattering techniques yield only ensemble-averaged quantities. In studying phenomena such as the nucleation of shear bands, the fluctuations in particle-scale quantities are imperative to understanding the incipient mechanisms and are not detectable in ensemble-averaged measures. In addition to particle-scale resolution, some model systems may also allow for the interactions between the particles to be tuned by varying both their range and magnitude. For example, salt may be added to colloidal suspensions to tune the range of interactions[154]. This "tunability" enables researchers to isolate the effect of particle-particle interactions from structure in a material's response.

The bubble raft of Bragg and Nye is an example of a well-known model system[155][156]. In their experiments, Bragg and Nye formed two-dimensional packings of air bubbles by bubbling air into a soap solution. The air bubbles crystallize into a

two-dimensional foam on the solution's surface and form with observable defects like dislocations, grain boundaries, and vacancies. By shearing or compressing the bubble raft, Bragg and Nye were able to study the way these defects behaved under an applied stress. Specifically, they studied the nucleation of dislocations, which they found preferentially occurred at the edges of the bubble raft. Because of the macroscopic scale of the system, the propagation of the nucleated dislocations across the raft and the resulting shear offsets were readily observable and provided confirmation of Taylor's theory of dislocation motion[60], which had been proposed more than a decade prior.

Model systems have played a particularly important role in the study of amorphous solids. Simpson and Hodkinson modified Bragg and Nye's crystalline bubble raft experiment by mixing bubbles of different sizes[157] to create an amorphous foam. They found that the Young's modulus of the amorphous raft showed a similar reduction in comparison to a crystalline raft as amorphous silica did in comparison to crystalline silica. Argon and Kuo[80] also used an amorphous bubble raft to study the mechanics of the amorphous structure[77], but instead of measuring the elastic response, they used their raft to observe the plastic events that occurred during shear and compression. By measuring the particle-scale displacement fields that they observed during deformation, they confirmed the cooperative nature of the rearrangements and strengthened Argon's proposed shear transformations[77].

Colloidal systems have been widely used as models for atomic glasses. The

reasons for their widespread use are manifold, but we highlight three benefits in particular: 1) colloidal particles are large enough to be imaged using optical or laser-scanning confocal microscopes, 2) the interactions between the particles can be tuned from repulsive to attractive to nearly hard-sphere, and 3) the volume fraction and polydispersity of the particles can be used to form different phases[154, 158]. Weeks et al. used a confocal microscope to measure the aging of a colloidal glass at packing fractions near the glass transition[30, 159]. These experiments were the first to directly measure individual particle dynamics at various proximities to the glass transition, making them instrumental in guiding theories of the glass transition. Schall et al. used a three-dimensional packing of silica particles to study thermal and shear-induced rearrangements[81]. Using confocal microscopy, they observed rearrangements in the quiescent and sheared glass. Under shear, they found the signature quadrupolar strain field predicted by Eshelby's solution for an ellipsoidal inclusion, which they interpreted as more evidence of Argon's ST. Additionally, they were able to observe the STs coalesce into a network under continued shear, which they suggested is the nascent stage of shear banding. Jensen et al. performed similar shear experiments but analyzed the resulting strain fields differently[160]. Instead of attempting to identify individual STs, Jensen et al. quantified the spatial correlations in strain. The correlations are found to be nearly identical to the correlations predicted by the analytical solution for Eshelby's inclusion, thereby providing further support for the cooperative nature and long range elastic field of shear transformation zones.

Granular systems have also been used extensively as model systems. Granular systems are distinguished from colloidal systems in that the larger granular particles do not perform Brownian motion, making granular systems athermal. In the granular pillar compression experiments of Rieser and Durian[161, 162], granular pillars composed of plastic rods oriented vertically on a substrate are compressed using a platten. During compression, images of the pillar are collected using a camera mounted above the apparatus. Because the individual rods can be tracked individually, the particle-scale deformation can be quantified precisely. Indeed, the chains of particles oriented along directions of high shear show intermittent burst in shear strain rate – a shear band. Rieser et al. find a spatial correlation between these bands and a novel measure of the local structure.

Most of the model system studies previously discussed seek to understand the bulk behavior of the material of interest; as such, efforts are taken to mitigate the effects of extrinsic features like boundaries. Additionally, because confining forces are often necessary to stabilize these model systems, the effects of free surfaces have received little attention. While specimen size and surfaces are known to influence the deformation behavior of MGs[145, 163], the underlying reasons for their effects remain open[89, 146, 164]. Therefore, should one be able to create a model glass with free surfaces and variable specimen size, an opportunity exists to connect macroscopic size effects with variations in the microscopic mechanisms thereby adding insight to the size-dependent behavior of atomic glasses.

1.4. Summary and Thesis Outline

This review of the current state-of-the-art demonstrates that glasses of different characteristic length scales possess certain shared properties, including a glass/jamming transition, an excess of low-energy vibrational modes, dynamical heterogeneity, and rheological behavior. Strain localization – the propensity for strain to accumulate in thin bands of a material – is a universal feature of amorphous solids that has been less well-explored. Moreover, because strain localization is often accompanied by runaway, catastrophic fracture, strategies to detect and mitigate its nascent stages are applicable in applications as diverse as soil handling and polymer design. Of particular interest is the mitigation of shear banding in MGs, a class of material that possesses many desirable properties but has seen limited industrial acceptance due in part to limited ductility.

Despite recent progress in the field, there are numerous unresolved questions pertaining to plasticity in amorphous solids. While the nature of the fundamental plastic event – the shear transformation – has been observed in many amorphous solids, a satisfactory description of the ST's structural fingerprint, dynamics, and interaction with other STs remains unsettled. The identification of STs *a priori* remains an outstanding challenge; consequently, the extent to which a universal description of flow defects may be established in all amorphous solids remains debatable.

Additionally, the progression from individual STs to a critical shear band nucleus

remains poorly understood. For instance, the challenge of defining a universal critical shear band nucleus in the context of ST density, a structural descriptor such as softness or flexibility volume or some other metric remains unsolved. In MGs, it has been established that altering the structure of the glass through thermal and mechanical treatments can significantly alter a glass's ductility. The root cause(s) for this enhancement remain unclear: are the spatial distributions of flow defects altered, is the shear band nucleation process somehow affected, or is there another basis for the increased ductility? Satisfactory resolution of this question is dependent on a more robust definition of the shear band nucleation process.

Finally, the defining structure and dynamics of a mature shear band remain debatable. Specifically, the equivalence between a mature shear band and the isotropic glass/jamming transition remains ambiguous. Can a shear band be identified simply as an anisotropic glass transition, or are the structure and dynamics within the shear band distinct from the isotropic case?

Methods to toughen glasses to overcome or mitigate their intrinsic strain-softening behavior are needed to accelerate their adoption in technical applications, and the aforementioned outstanding questions often preclude progress. Moreover, due to the extremely small time and length scales associated with shear banding in MGs, experimental characterization of their nucleation, operation, and interaction is challenging. Therefore, model systems which mimic the behavior of an MG at an observable length scale are desirable.

In this thesis, we present experiments on colloidal pillars, which prove to be an appropriate model system. In Chapter 2, we describe a method to form colloidal pillars and discuss the effects of particle size and material on the morphology of the pillars. In Chapter 3, we report results of instrumented compression tests on amorphous pillars. Here, we observe shear banding and mechanical response that is strikingly similar to the behavior of MGs. In Chapter 4, we describe 4D *in situ* compression experiments, which allow us to study deformation in a pillar at the particle scale as shear banding proceeds. Finally, in Chapter 5 we highlight possible future directions of study and potential applications of our findings.

Chapter 2
Synthesis of Colloidal Pillars

Soft matter is a class of material that is composed of mesoscopic particles dispersed in a solvent of much smaller particles[165]. Aerosols (solid or liquid particles dispersed in a gas), emulsions (liquid particles dispersed in a liquid), and foams (gas particles dispersed in a liquid or solid) are three examples of common soft materials. In a soft material, the energy of the inter-particle interactions normalized by the particle mass is small in comparison to the interactions between atoms[166]. Just as atomic matter can exist as a solid, a liquid, or a gas, soft matter can also take on different phases. Two types of soft solids are colloidal and granular packings that are distinguished by particle size and particle-scale thermalization. In common lexicon, "colloidal" refers to particles that have a size of less than $1\mu m$; conversely, "granular" particles are larger than $1\mu m$. In a colloidal packing, the small particle size and/or the presence of a viscous surrounding fluid results in non-negligible Brownian motion of the particles and a finite temperature; in a granular packing, the Brownian motion is unimportant and the system can be considered athermal[167].

In this chapter, we will present a method for the preparation of colloidal pillars. The particles used in these pillars range in size from 85 nm to 7 μm. This range spans the $1\mu m$ boundary commonly used to delineate colloidal from granular systems – to avoid confusion, we will refer to all of the pillars as "colloidal". These colloidal

pillars are unique in that they are free from confining boundaries. In addition, the small constituent particle size differentiates these pillars in comparison to other dry colloidal/granular systems reported in literature. We introduce a method to alter the pillar structure, which we will later show alters the mechanical response. The pillars are an excellent model system to investigate some of the outstanding questions regarding plasticity in amorphous solids.

2.1. Materials and Methods

2.1.1. Synthesis of Colloidal Pillars

Colloidal pillars are synthesized by filling glass capillaries with suspensions of colloidal particles (details on the suspensions are given in Sections 2.1.2 and 2.1.3). As-purchased glass capillaries are cut into shorter pieces with a length of ∼4 cm using a glass cutter. The two ends of each capillary are polished using a polishing wheel with a 6 μm diamond-impregnated polymer film to make the faces of the capillary flat and smooth. The polished capillaries are cleaned with isopropanol to remove any contamination introduced during the polishing process.

After cutting the capillaries to length, the empty capillaries are silanized with octadecyltrichlorosilane (OTS) in toluene to render the inner surface hydrophobic and to limit the adhesion of particles to the inner walls of the capillaries during the drying process (Figure 2.1a and b).

The colloidal particle suspension is subsequently injected into the capillaries using a disposable syringe. The open end of the syringe is fitted with a 304 stainless steel and polytetrafluoroethylene (PTFE) dispensing needle and plastic tubing to help direct the suspension flow into the capillaries (Figure 2.1c). The filled capillary is placed horizontally on a bench or on a rotating wheel at room temperature and allowed to dry. The rotating wheel is used to prevent separation of particles by size due to gravimetric sedimentation. The drying process typically takes 3 days. After the water in the capillary has completely evaporated, a dense pillar remains (Figure 2.1d).
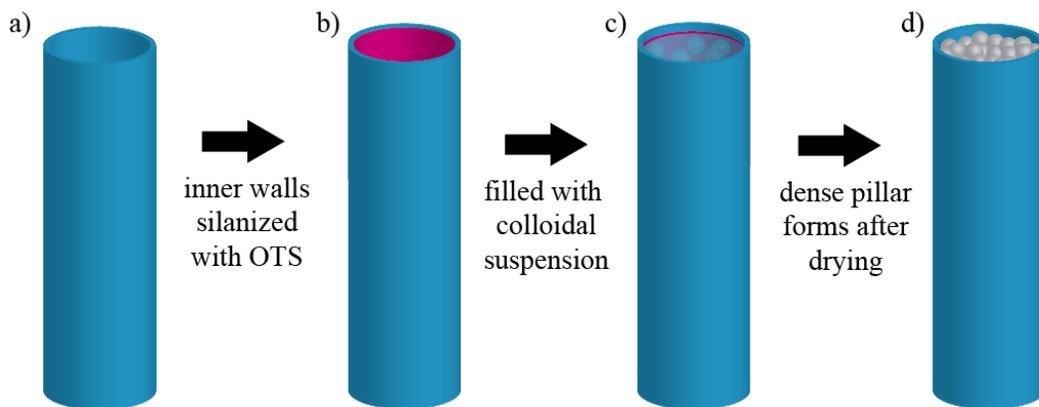
Figure 2.1: Procedure for forming colloidal pillars in capillary tube. a) An empty capillary tube is first b) silanized with OTS to make the inner surface hydrophobic. The capillary is c) filled with a suspension containing colloidal particles. After drying, a d) dense pillar remains.

2.1.2. Pillars for Instrumented Compression Experiments

Multiple combinations of colloidal particles and capillary diameters are used to form pillars for instrumented compression experiments. A summary of the particles and capillaries used is presented in Table 1.

colloid material	colloid size (nm)	capillary diameter (μm)	structure	cracked
SiO$_2$	85 $\pm$15	580	amorphous	yes
SiO$_2$	250	580	amorphous	yes
SiO$_2$	7000	580	amorphous	no
SiO$_2$	7000	900	amorphous	no
PS	500	580	amorphous	yes
PS	500	900	amorphous	yes
PS	6150	580	polycrystalline	no
PS	6150	900	polycrystalline	no
PS	3000/6150	580	amorphous	no
PS	3000/6150	900	amorphous	no

Table 1: Combinations of colloids and capillaries used in the synthesis of pillars for instrumented compression experiments.

Spherical SiO$_2$ particles with an average diameter of 85 nm (30-31 wt% suspension in isopropanol, particle sizes ranging between 70 nm and 100 nm) are obtained from Nissan Chemical America Corporation. 250 nm spherical SiO$_2$ nanoparticles with standard deviation <10% are purchased from Fiber Optic Center, Inc. 7 μm spherical SiO$_2$ particles are obtained. Polystyrene (PS) spheres with diameter 500 nm are obtained. PS spheres with diameters of 3.004 $\pm$ 0.065 μm (2.64% solid-latex) and 6.15 $\pm$ 0.188 μm (10% solids) are purchased from Polyscience, Inc. and Bangs Laboratories, Inc., respectively. Standard glass capillaries with inner diameter (ID) of 580 μm and outer diameter (OD) of 1,000 μm are purchased from World Precision Instruments, Inc. Borosilicate glass capillaries with ID 900 μm and OD 1,000 μm are purchased from Produstrial LLC.

A 25 wt% 250 nm SiO$_2$ aqueous suspension is prepared for the pillar fabrication. The as-received 85 nm SiO$_2$ and 6.15 μm PS suspensions are concentrated using a centrifuge at 1000 rpm for 10 min by removing a significant amount of the supernatant.

After drying, the pillars are extruded from the capillary tube and imaged using an optical or confocal microscope. We find that pillars composed of particles with diameter less than $\sim 1\mu$m develop cracks during drying (Figure 2.2a and b), while pillars composed of larger particles (Figure 2.2c) do not. While not exhaustively explored, the propensity of a pillar to form cracks appears to be influenced mainly by particle size and not pillar diameter or colloid material (Figure 2.2d). This result is consistent with previous observations on the effect of colloid size on crack formation
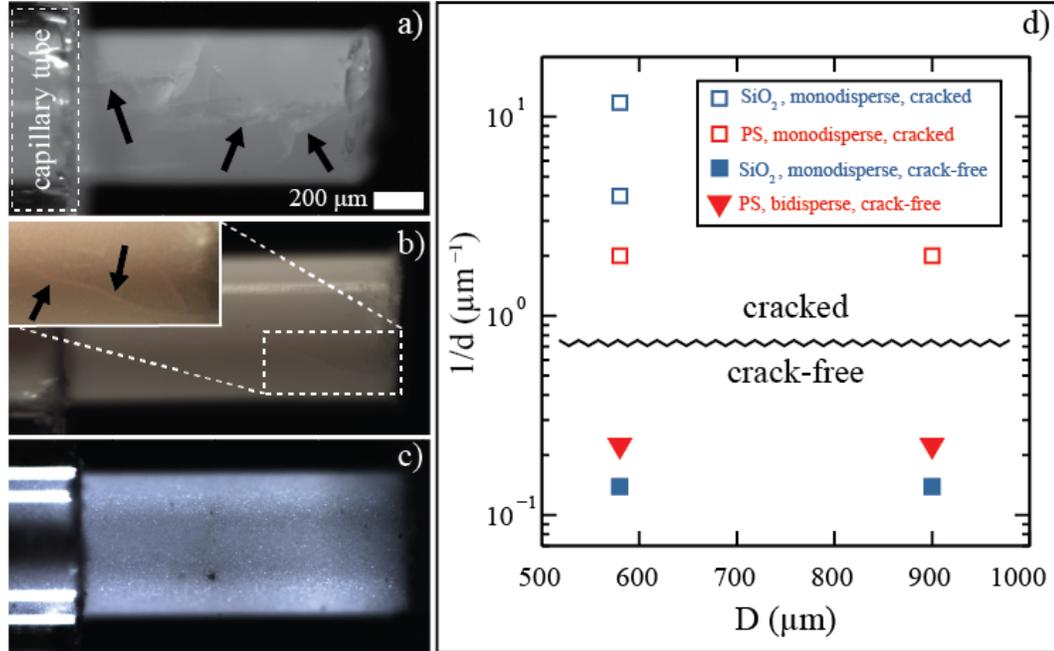
Figure 2.2: 580 μm diameter pillars composed of a) 85 nm SiO$_2$ spheres, b) 250 nm SiO$_2$ spheres, and c) a mixture of 3 and 6 μm PS spheres. Cracks are evident in the pillars composed of 85 nm and 250 nm SiO$_2$ particles. Scale bar is the same for each image. d) Pillars composed of larger particles show no evidence of the cracking observed in the pillars composed of smaller particles. Pillars composed of SiO2 particles are indicated by blue markers. Pillars composed of PS particles are indicated by red markers. Squares denote pillars composed of monodisperse particles and triangles denote pillars composed of bidisperse particles. Open symbols indicate pillars that form with cracks and filled symbols indicate pillars that form crack-free.

in drying colloidal thin-films[168]. Pillars composed of 6.15 μm PS show crystallization due to the small polydispersity. To avoid crystallization, we prepare a bidisperse suspension by mixing the 3 μm PS suspension and 6.15 μm PS suspension with a volume ratio of 3.78[169] (hereafter referred to as the 3/6 μm PS pillars).

Mechanical Annealing

In addition to the stochastic structural variation that results from the synthesis process, we developed a mechanical annealing procedure to reproducibly alter the packing fraction, ϕ, of the pillars. This procedure was applied only to the 3/6 μm PS pillars. After allowing the suspension of colloidal particles to dry within the capillary tube, two steel wires with diameters slightly smaller than the capillary diameter are inserted into both ends, rendering the packing fully confined (Figure 2.3). A piezoelectric actuator is brought into contact with one of the wires and the opposite wire is coupled to a force transducer, enabling measurement of the axial force. Sinusoidal displacements ($f = 0.5 - 5$ Hz, $A = 0.60 - 3.60$ μm) are produced by the actuator, which remains in contact with the wire. The piston periodically loads and unloads the pillar about the mean confining force ($F_{conf} \sim 0.1 - 10$ N), resulting in a gradual densification of the pillar and an increase in ϕ. After mechanically annealing the pillar from one side, the capillary tube orientation is reversed and the process is repeated from the other side to promote uniform compaction. Varying the confining force in addition to the amplitude, frequency, and number of displacement cycles allows for some control of compaction.

Following annealing, the average packing fraction of the confined pillar, $\langle\phi\rangle$, is determined by measuring the diameter, D, length, L, and mass, m_{filled}, using high-resolution optical microscopy and microbalance measurements, respectively. Upon
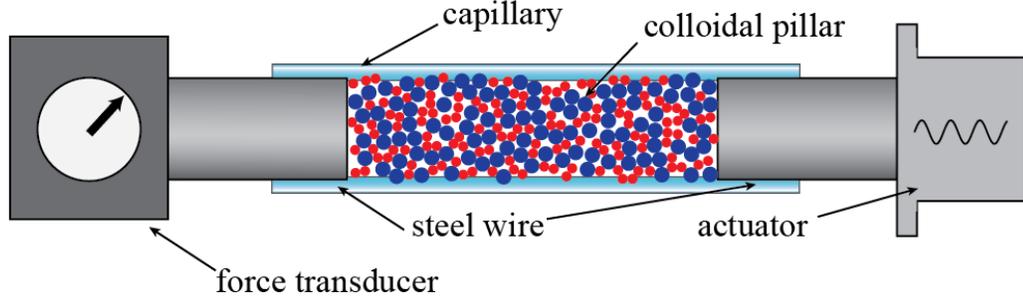
Figure 2.3: The mechanical annealing setup. The colloidal pillar is confined within a capillary by two steel wires between the actuator and the force transducer, and a sinusoidal displacement is generated by the actuator, leading to compaction of the pillar.

completion of mechanical testing, the mass of the empty capillary tube, m_{empty}, is measured. Using the density of PS, ρ_{PS}, the average packing fraction is determined as:

$$\langle \phi \rangle = V_{solid}/V_{bulk} = \frac{(m_{filled} - m_{empty})/\rho_{PS}}{\pi D^2 L/4}$$

Our mechanical annealing procedure produced pillars with $0.528 \leq \langle \phi \rangle \leq 0.684$. For our mixture of 3/6 μm PS particles, the random close packing limit (RCP) is predicted to be $\phi = 0.683$[170]. The lower bound, random loose packing (RLP), for a bidisperse mixture of frictional, cohesive particles is not known, but rheology measurements on a bidisperse mixture of hard-spheres with similar diameter ($\frac{D_L}{D_S}$) and total volume ($\frac{N_L V_L}{N_S V_S}$) ratios show a fluidity limit, marked by a large increase in viscosity, at $\phi = 0.550$[171]. Thus, our 3/6 μm PS pillars span the full spectrum of glass packing.

2.1.3. Pillars for 4D in-situ Compression Experiments

In addition to the pillars prepared for instrumented compression experiments, we also synthesized pillars specifically for 4D in-situ compression experiments. Thin-wall glass capillary tubes with an ID of 300 μm and an OD of 450 μm are obtained from Produstrial LLC. The capillary tubes are cut and polished following the same procedure described in Section 2.1.1. After polishing, an aqueous mixture of polyethylenimine (PEI) and silica particles is passed through the capillaries and allowed to dry. The capillaries are heated to fuse the silica particles to the inner walls of the capillary. This procedure adds roughness to the walls and suppresses crystallization of the colloidal particles near the walls.

After fusing the silica to the capillary walls, a suspension of 3.3 μm fluorescent poly(methyl methacrylate) (PMMA) (Andrew Schofield laboratory, University of Edinburgh) particles is injected into the capillary tube. Polydispersity of between 6% and 8% in the particle sizes suppresses crystallization, resulting in an amorphous packing. After the suspension has dried, the capillary tube is secured to a #0 glass cover slip (Goldseal) using UV-curable adhesive (Norland Optical Adhesive No. 61). Once secured, a length of the pillar is forced out of the capillary tube to form a free-standing compression specimen. Prior to extruding the specimen, the dried suspension is re-wetted using bromocyclohexane (CXB) to increase the cohesion between the particles and prevents the extruded specimen from crumbling.

2.2. Conclusions

We have presented a novel method for the preparation of free-standing pillars composed of various colloidal particles. Pillars composed of particles less than $\sim 1\mu m$ in size dry with a significant population of cracks due to the large capillary forces relative to the particle mass. Pillars composed of larger particles dry without visible cracks. An amorphous pillar structure can be attained by using a bidisperse mixture of particles. We also presented a method to alter the average packing fraction of the pillars, $\langle\phi\rangle$, using mechanical annealing. The annealed pillars appear to span the range of solid, amorphous densities for our particular mixture of particle sizes.

Chapter 3

Instrumented Compression Testing of Colloidal Pillars

Uniaxial compression is an effective method for evaluating the elastic and plastic response of a material. In a uniaxial compression test, a cylindrical or rod-shaped sample is subjected to a displacement or stress-controlled deformation along its major axis without confinement along the secondary axes. The material's response prior to yield can be used to determine its elastic constants. The material's compressive strength may be determined from the yield point. Finally, the post-yield morphology of plastic deformation can be used to infer the mechanisms underlying yield.

In this Chapter, we will present a method for the instrumented (the force imposed on the sample is measured) uniaxial compression of the colloidal pillars described in Section 2.1.2. Our results show that the pillars are an excellent model system to investigate some of the outstanding questions regarding plasticity in amorphous solids.

3.1. Compression Experiments

Following the synthesis procedure outlined in Section 2.1.2, a polished steel wire is inserted into the capillary and brought into contact with the confined pillar. The smooth wire face ensures uniform contact between the wire and pillar and aids in

preserving the initial pillar structure. The length of the wire is adjusted so that several centimeters remain exposed from the capillary after contact with the pillar is made. The capillary/wire assembly is secured to a custom grip using a clamp (see Figure 3.1a) and the exposed face of the wire is brought into contact with a finely-threaded drive screw. Turning the screw pushes the pillar through the capillary and allows for precise control of the length of the exposed pillar that emerges from the opposite end. In uniaxial compression, the sample geometry is known to affect the deformation mode observed[172]. To promote shearing, as opposed to buckling or barreling, the aspect ratios of the pillars (l_o/D, where l_o is the exposed pillar length and D is the pillar diameter) are maintained at values between $\sim$2.2 and $\sim$2.6. The wire also serves to backstop the pillar during the compression experiment.
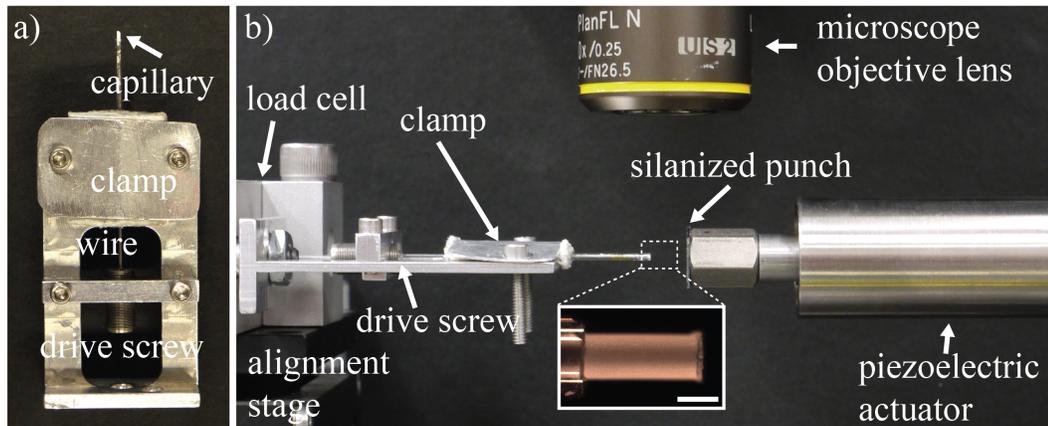
Figure 3.1: a) The custom grip. A wire is used to push the pillar out of the capillary. A finely-threaded drive screw allows for precise control of the exposed pillar length. b) Compression testing apparatus for colloidal pillars. The capillary is secured to a custom grip using a clamp and the grip is fixed to a load cell. A displacement is generated using a silanized silicon punch attached to a piezoelectric actuator. The setup may be operated in the field-of-view of both optical and laser confocal microscopes to observe the pillar deformation during compression. Inset: an exposed pillar, scale bar 500 μm.

Once the capillary is secured to the grip, the grip is attached to a load cell (GSO Series - Transducer Techniques, 0-100 mN, 0-1 N, and 0-10 N force ranges) so that the transmitted force may be recorded. A groove machined in the grip ensures axial alignment of the capillary and the load cell axis. The load cell is mounted to a combined translation/rotation stage (see Figure 3.1b). A piezoelectric actuator (P-212 Series, Physik Instrumente, 0-60 μm and 0-120 μm actuation ranges) is secured to a second translation/rotation stage opposite from the load cell. The stages allow for precise alignment of the actuator and load cell to ensure that the direction of compression is aligned with the pillar axis. A silicon wafer treated with OTS is fixed to the end of the actuator and is used as a punch. The OTS minimizes friction and adhesion with the pillar face, which have been shown to suppress shearing modes by confining the sample laterally[164, 172, 173]. Determination of the in-pillar displacement ($\Delta l = l_o - l$, where l_o is the initial pillar length and the sign convention is adopted to give positive values in compression) is made using the absolute displacement of the punch and the measured stiffness of each load cell.

The pillars do not dry with a flat surface and uneven contact between the punch and the pillar face results in large local stresses and crumbling at the pillar face. To minimize this effect, the pillar faces are formed prior to compression by extruding a small length of pillar ($\sim$20 μm for a 580 μm diameter pillar) and flattening the exposed pillar with the punch. Remnant particles are removed with compressed air and the pillar is then extruded to the desired length.

The compression testing apparatus is positioned in the focal plane of an optical or laser scanning confocal microscope (reflectance mode, $\lambda = 639$ nm). Digital images collected during compression allow for correlation of measurements of mechanical response with macroscopic events such as crack propagation or shear band propagation. Particles larger than ~5 μm are distinguishable at magnifications as low as 50x and provide substantial image contrast and digital image correlation is used to measure surface displacements from a series of images[174–176]. Full-field strain maps of the pillar surface are calculated from the spatial gradients of the displacement fields. The image sequences also allow for the correlation of any pillar slip within the capillary tube to recorded load drops.

3.2. Results and Discussion

3.2.1. Pre-Cracked Pillars

In situ micrographs and the mechanical response from a representative compression experiment of a 580 μm diameter pillar composed of 85 nm SiO$_2$ spheres are shown in Figure 3.2. As discussed in Section 2.1.2, these pillars dry with a significant population of macroscopic cracks. The distribution of these defects governs deformation behavior. The force-displacement response may be partitioned into initial stiffening from $\approx$0-0.005, linear response from $\approx$0.005-0.010, and a subsequent series of crack opening and propagation. Stiffening results from non-uniform contact

between the pillar face and punch, which is mitigated in subsequent experiments by conditioning the pillar face according to the procedure outlined in Section 3.1. Once the pillar-punch contact area becomes approximately constant, force increases linearly with $\Delta l/l_o$. No changes in the geometry of the cracks are observed during the stiffening and linear compression phases. The transition from linear to non-linear force response correlates with the opening of a crack near the punch face. During opening, the crack separates along the direction of maximum tensile stress (perpendicular to the direction of compression) while the crack tip remains fixed. The crack remains stable (no observable tip movement) up to point **b**, after which it propagates along a direction approximately parallel to the direction of compression. Crack propagation correlates with the first force drop at point **c**. The sequence of crack opening and propagation continues as $\Delta l/l_o$ is increased further (see Figure 3.2d and e).

The behavior of a 580 μm diameter pillar composed of larger 250 nm SiO_2 spheres, which also forms with pre-existing macroscopic cracks, shows similar crack evolution during loading. The face of the pillar was conditioned prior to compression and no initial stiffening is observed. Linear force response is observed up to ≈ 0.015 after which a crack propagates down the pillar axis, resulting in a relatively large load drop. In contrast to the 85 nm SiO_2 pillar, no crack opening is observed prior to crack propagation, which occurs initially at a load of $\sim$34 mN. The first active crack in the 250 nm SiO_2 pillar propagates the full length of the pillar axis. Therefore, the load-bearing ability of the pillar is greatly reduced, and subsequent displacement
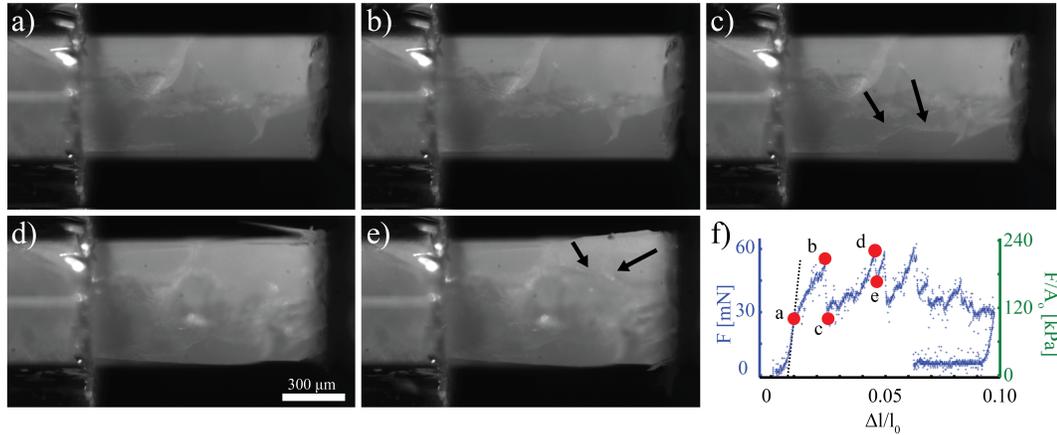
Figure 3.2: a) compression experiment on a 580 μm diameter pillar composed of 85 nm SiO$_2$ spheres. The red dots in frame f correspond to the micrographs. The pillar behaves quasielastically up to point a, after which one of the cracks slowly opens (frame b). The crack, highlighted by the black arrows in frame c, becomes unstable and propagates down the axis. This event corresponds to the first sudden load drop (frame f). Subsequent loading opens and activates other cracks (frames d and e). The arrows in frame e indicate the crack corresponding to the load drop between frames d and e.

fails to produce forces more than $\sim$1/2 of that required to activate the first crack. By comparison, the first active crack in the 85 nm SiO$_2$ pillar propagated $\sim$1/2 of the pillar length, and subsequent displacement generated forces larger than the force required to activate the first crack.

The compression experiments discussed are representative of the response observed in more than 5 85 nm pillars and more than 15 250 nm SiO$_2$ pillars. Collectively, we observe that the pillars composed of 85 nm and 250 nm SiO$_2$ dry with a large population of cracks, which ultimately dominate the mechanical response. Similar to fracture processes observed in brittle solids, the yield force and peak force of our pre-cracked pillars are governed by the initial flaw population and its evolution during

56

compression[177]. The force required for crack growth and propagation depends on the crack geometry (orientation and size) and particle-particle cohesion. While pillars with large populations of cracks are potentially interesting for fracture mechanics investigations, they are not suitable for probing shear banding behavior as the forces required to activate the cracks are less than the force required to nucleate shear bands. Thus, we next turn our attention to pillars synthesized with no visible pre-existing flaws.

3.2.2. Pristine Amorphous Pillars

Pillars composed of 3 and 6 μm polystyrene spheres dry without cracking, and the deformation mode observed in these pillars is different from the crack opening/propagation found in pillars composed of smaller particles. As mentioned in Section 2.1.1, a bidisperse colloid size mixture is used to suppress crystallization and the resulting amorphous structure is confirmed from micrographs of the surface. Micrographs and the mechanical response from a representative compression experiment of a 580 μm diameter pillar composed of 3 and 6 μm polystyrene spheres are shown in Figure 3.3.

Upon initial loading, force increases approximately linearly with $\Delta l/l_o$ strain and the strain throughout the pillar is relatively uniform with only a slight enhancement of compressive strain near the punch (see Figure 3.3a and b). As $\Delta l/l_o$ increases, the magnitude of strain near the punch increases relative to the strain in the rest of the
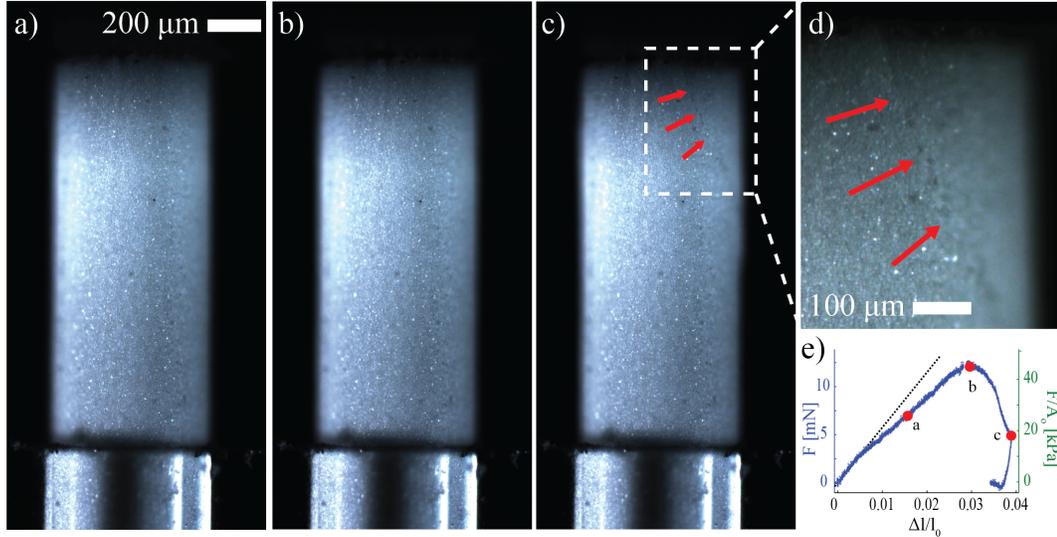
Figure 3.3: a) Optical micrographs acquired during compression of a 580 μm diameter pillar composed of 3 and 6 μm PS spheres. The punch is located at the top face of the pillar and actuates downward. The inset at the lower right shows the mechanical response (loading stiffness = 2.3 MPa, dashed line to denote linear response). At the point marked **b, a shear band begins to form. The mature shear band is indicated in frames c and d.**

pillar. At a critical force of $\sim$12.5 mN, the pillar begins to soften and each incremental displacement step results in a decrease in force. This softening corresponds to the nucleation of a shear band near the punch face, as seen in Figure 3.3c and d. During this nucleation stage, which persists from $\Delta l/l_o \approx 0.030 - 0.033$, structural evolution is observable along the shear band region despite the absence of a clear shear offset at the pillar surface. Further displacement induces shear band propagation during which slip is observable along the shear band and a detectable shear offset develops at the surface. While the full orientation of the shear band is not determinable from the micrographs, it appears that the band forms along a direction approximately 45° from the direction of compression, which is parallel to the direction of maximum shear

stress.

It is interesting to compare the deformation that we observe in the 3/6 μm pillars with the modes found in other amorphous systems. The shear bands that develop in the pillars have a finite thickness. From inspection of micrographs acquired during shear band propagation, we estimate the thickness to be ∼5 particle diameters. This thickness is consistent with the values reported in a sheared suspension of colloidal PMMA particles[178]. The shear band orientation of approximately 45° from the direction of compression is similar to the angle observed in experiments[179] and simulations[180] of compression of other granular solids. The examination of deviations from this angle has been suggested as a method to gain insight on the pressure dependence of yielding in disordered solids[66]. We consistently observe shear bands that originate at the pillar/punch interface and grow to intersect a free surface. Without the confining walls found in other granular compression experiments, there is no restoring force for radial displacements. Therefore, local softening due to dilatory structural evolution is concentrated near the punch and results in the preferential location for shear band formation. This behavior more closely resembles that found in compression experiments of micro-scale BMG pillars[11, 181, 182].

3.2.3. Effect of Ambient Humidity

Although the orientation and location of the shear bands are consistent from pillar to pillar, the normalized force at shear banding onset, F/A_o, is found to vary from

47 to 830 kPa. While structural variation from pillar to pillar surely affects the peak force value, we believe that fluctuating humidity may also account for the variability. All of the experiments reported to this point were performed in ambient conditions with no special provisions taken to control humidity levels. To explore the effect of humidity on pillar response, an environmental chamber capable of varying relative humidity (RH) from <2% RH to >98% RH was constructed for the compression testing apparatus.

Multiple compression cycles of a single pillar at various levels of RH illustrate the impact of environmental conditions on the mechanical response. A 900 μm diameter pillar composed of 3/6 μm PS spheres is compressed 25 times to displacements much less than the values necessary to cause shear banding ($\Delta l/l_o < 0.003$). Over the course of the compressions, RH is adjusted from near saturation (96% RH) to dry (<2% RH) and then back to near saturation. Eight of the response curves are plotted in Figure 3.4a. The plot ordering follows the sequence of testing, with the left-most plot corresponding to the first compression and the right-most plot corresponding to the last compression. Blue, red, green, and black plots correspond to 96% RH, 51% RH, 21% RH, and <2% RH environments, respectively. It is found that decreasing RH results in significant stiffening of the pillar, and the subsequent increase of RH restores the compliance of the pillar. To quantify the variation, polynomials are fit to the load and unload responses, expressed as F/A_o vs. $\Delta l/l_o$, for each of the 25 compression experiments. The maximum instantaneous stiffness, as determined from

the maximum value of $\frac{l_o}{A_o}\frac{dF}{d\Delta l}$ over the range of $\Delta l/l_o$, is extracted for each compression cycle. Figure 3.4b plots the maximum instantaneous load and unload stiffnesses for different values of RH. A low RH environment results in a pillar that is 10x stiffer than the same pillar compressed in a high RH environment. The decrease in unload stiffness with increasing RH is non-monotonic and reaches a maximum between 35-50% RH, where we observe a two-fold increase in the unload stiffness over the stiffness at <2% RH. The magnitude of the stiffness increase is similar to that observed in a colloidal crystal indented at various levels of RH[183]. The cross-over region between the extreme values of stiffness extends over a wide range of RH (30-70% RH) that overlaps with typical ambient RH variation.

Increasing environmental RH increases the moisture content in the pillar due to capillary condensation. In the limit of a completely dry pillar, a state not realizable in our system, particle-particle cohesion due to water-bridges vanishes. At low RH, water-bridges form at the contact points between particles and increase cohesion. When these water-bridges remain distinct, the pillar is said to be in the pendular state[184] defined for wet granular media. Increasing RH further results in some of the water-bridges merging and completely filling some of the voids in the pillar and the pillar is said to be in the funicular state. Higher RH may saturate the pillar, filling all of the voids, and the pillar is said to be in the capillary state.

Dynamic vapor sorption (DVS) is performed to quantify the water content in the pillar as a function of RH. DVS employs a precision microbalance to measure
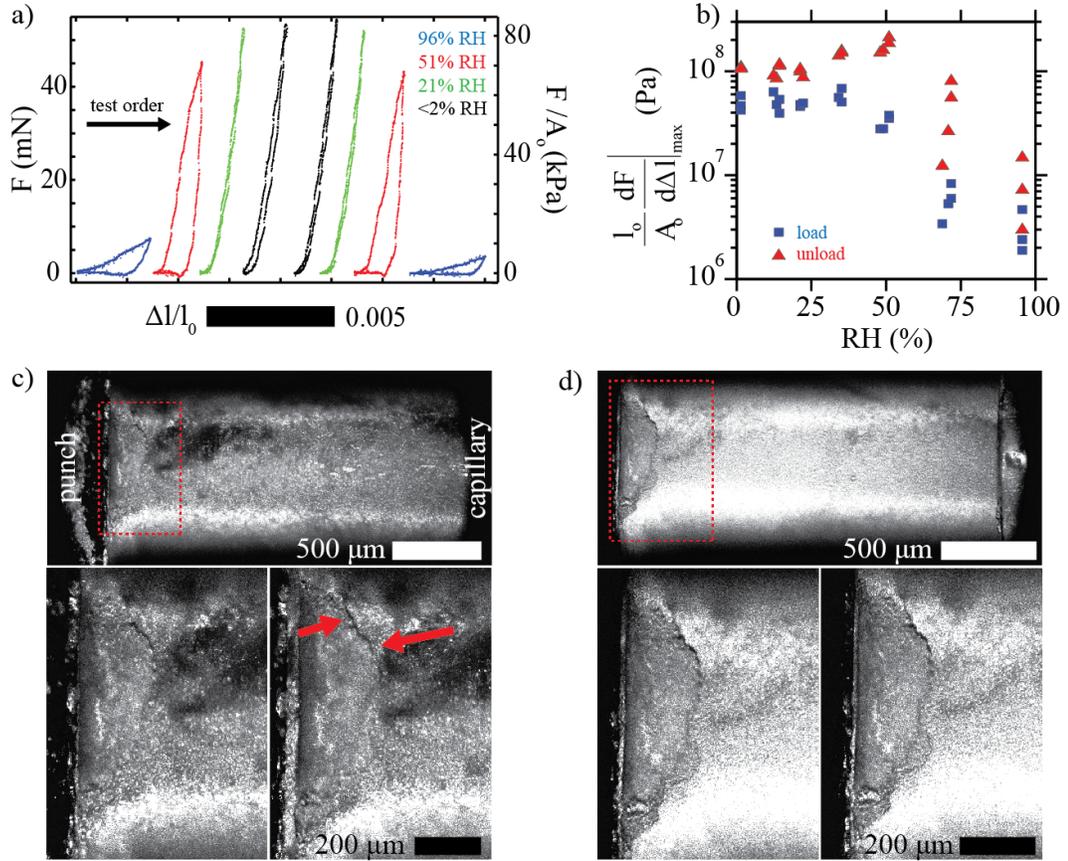
Figure 3.4: a) Eight sequential response curves for a pillar compressed at different RH. b) The variation of the maximum instantaneous stiffness on load and unload with changes in RH. c) Confocal micrographs from a pillar compressed at 96% RH. Top frame shows entire pillar, lower left frame shows region denoted by red box prior to compression, and the lower right frame shows the same region after compression. Significant structural evolution of a previously sheared region is observed. d) Confocal micrographs from a pillar compressed at <2% RH. Top frame shows entire pillar, lower left frame shows region denoted by red box prior to compression, and the lower right frame shows the same region after compression. Little structural evolution of a previously sheared region is observed.

the change in the mass of a sample with changes in RH. The relative change in mass of the pillar is given by $m(RH)/m_{dry}$ where m_{dry} is the mass of the dry pillar and $m(RH)$ is the mass of the pillar at a given RH. The bulk volume, V_{bulk}, of the pillar is determined by measuring the pillar dimensions using optical microscopy and the

void volume, V_{void}, is determined through the relation:

$$V_{void} = V_{bulk} - \frac{m_{dry}}{\rho_{PS}}$$

where ρ_{PS} is the density of PS (1.06 g/cc). For the 900 μm diameter pillar composed of 3/6 μm PS spheres, $V_{void}/V_{bulk} = 0.24$. The water content in the pillar is quantified by the dimensionless water content:

$$\frac{V_{water}}{V_{bulk}} = \frac{m(RH) - m_{dry}}{\rho_{H_2O} \times V_{void}}$$

where ρ_{H_2O} is the density of water (1.00 g/cc). The relative changes in mass and RH during a DVS experiment are plotted against time in Figure 3.5a, and the equilibrium relative change in mass and water content are plotted against RH in Figure 3.5b. It is found that the relationship between water content and RH is not linear, with a sharp increase in water content for RH values >80%.

Particle-particle cohesion and friction are markedly different in the pendular, funicular, and capillary states[184] and these variations are reflected in the distinct mechanical responses observed at different RH. In the pendular state, where $0 < V_{water}/V_{void} < 0.10$-$0.25$[179], cohesive forces are the result of water-bridges that form between particles. In the capillary state, where $V_{water}/V_{void} > 0.90$, cohesion is the result of suction generated in the fluid phase containing the particles. In the funicular
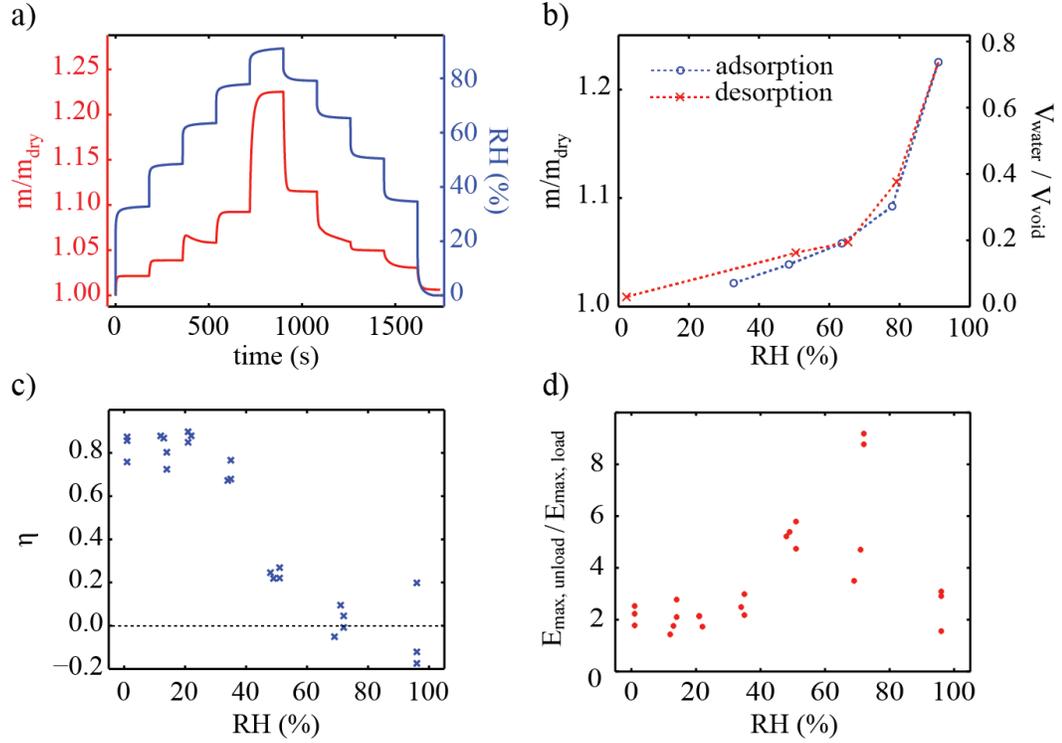
Figure 3.5: a) The relative change in mass and RH plotted against time for a 900 mm diameter pillar composed of 3/6 mm PS spheres. b) The equilibrium relative change in mass and water content as a function of RH on adsorption and desorption. c) The efficiency, a measure of the work recovered during a compression cycle, as a function of RH. d) The ratio of the maximum instantaneous stiffness on unload, $E_{max,unload}$, to the maximum instantaneous stiffness on loading, $E_{max,load}$.

state, cohesion is a combination of the cohesive interactions characteristic of the pendular and capillary states. Friction is greatly reduced in the capillary state, where the large water content serves as a lubricant between particles. In comparing the compression data with water content, we see that the maximum unloading stiffness achieved at 50% RH corresponds to a water content of ~0.12-0.15, a value associated with the pendular regime. Increasing RH beyond 50% results in a significant decrease in the loading and unloading stiffnesses which we attribute to increased plasticity.

We quantify the extent of plasticity at a given RH through two metrics: efficiency, η, and the ratio of the maximum instantaneous stiffness on unload to the maximum instantaneous stiffness on load. We define η as the ratio of the work done by the system on unloading to the work done on the system during loading:

$$\eta = \frac{\int_{x_{max}}^{0} F_{unload}(x)dx}{\int_{0}^{x_{max}} F_{load}(x)dx}$$

$\eta = 1$ would indicate a perfectly elastic process and $\eta = 0$ would indicate a perfectly plastic, or dissipative, process. The efficiency of the compression cycles as a function of RH is plotted in Figure 3.5c. At low RH, $\eta \approx 0.8$, which is the maximum value observed. At RH > 30%, η drops significantly and settles to values ~ 0 at 70% RH. Near saturation, several negative efficiency values are measured, indicating that the net work done on the pillar during unloading is positive (i.e., energy is put into the system on unloading). We attribute this effect to strong adhesion between the pillar face and the punch; pulling the pillar face off of the punch involves breaking many water-bridges that form between the surfaces during compression, which requires energy. The precipitous drop in η at RH values above 30% is indicative of significantly increased plasticity that occurs through dissipative mechanisms like particle-particle sliding and rolling. This assertion is reinforced by the drastic increase in the ratio of the maximum instantaneous stiffness on unload to the maximum instantaneous stiffness on load, $E_{max,unload}/E_{max,load}$, which increases from ~ 2 at RH < 40% to

values between 4 and 9 at $40\% < \text{RH} < 70\%$, corresponding to water content values $\sim$0.16-0.22. Taken as a whole, the water content and stiffness data indicate maximum cohesion at 50% RH and increased plasticity at >30% RH.

Confocal micrographs of a single pillar compressed to larger values of $\Delta l/l_o$ show a fundamental change in deformation in two extreme RH environments (see Figure 3.4c and d). In Figure 3.4c and d, the top image is the pillar prior to compression, the lower left image is the region outlined by the dashed red-box prior to compression, and the lower right image is the same region after compression. At 96% RH (Figure 3.4c), significant evolution of a previously sheared region (indicated by the red arrows) is observed during compression. Conversely, the sheared region in the very dry (<2% RH, Figure 3.5d) pillar shows little evolution.

The effect of varying levels of cohesion and friction on shear band nucleation and propagation is not clear. However, we have shown that the macroscopic quasi-elastic response of our pillars is a strong function of RH. The strong correlation between water content within the pillars and measurements of mechanical stiffness and efficiency suggest that RH strongly affects particle-particle cohesion and friction. In BMGs, a high ratio of the bulk modulus, B, to the shear modulus, G, has been associated with increased fracture toughness and plasticity[185]. This relationship has been rationalized by equating a high bulk modulus with the suppression of dilation and a low shear modulus with lower resistance to plastic flow. Therefore, large B/G promotes more shear band operation prior to final fracture. Exploring the effect of varying macroscopic

elastic properties in our model pillar packings, which can be controlled via tunable particle interactions, on the packings' plasticity and fracture may guide refinement of predictive models for design of tough atomic solids.

3.2.4. Scaling of Strength and Elastic Modulus

After the initial studies on the various pillars described to this point, a systematic study of the effect of structure on the mechanical response of the amorphous 3/6 μm PS pillars was conducted. These pillars were prepared using the mechanical annealing procedure described in Section 2.1.2 and the packing fraction, $\langle \phi \rangle$, of each pillar was measured prior to compression. Additionally, RH was held constant at 30%, 50%, or 60% RH over the duration of an experiment to ensure constant particle-particle interactions.

The measured ultimate strengths and effective elastic moduli for 27 3/6 μm PS pillar specimens are shown in Figure 3.6a and b. Both $\sigma_{max} = F_{max}/A_o$ and E_{load} are found to vary by more than 2.5 orders-of-magnitude over the range of $\langle \phi \rangle$ studied, corresponding to relatively loose and dense packings in the limit of low and high $\langle \phi \rangle$, respectively. We contend that σ_{max} is the best measure of the intrinsic strength of the pillar because plastic activity localized near the punch, which occurs at lower levels of applied stress, is likely a result of surface roughness and not representative of the bulk structure of the pillar. Surprisingly, σ_{max} and E_{load} appear to be relatively insensitive to RH in the range covered in these experiments.

Our measurements demonstrate a strong correlation between σ_{max} and E_{load} of individual disordered pillars (Figure 3.6c), with a slope of 0.009 ± 0.0009 that is invariant to $\langle \phi \rangle$ and RH (shown by coloring and shape of markers, respectively, in Figure 3.6c). The robust relationship between σ_{max} and E_{load} is suggestive of a unique and cooperative plastic event that establishes the maximum strain the pillars can withstand before macroscopically failing. The insensitivity of this universal scaling to RH also suggests that the details of inter-particle interactions do not influence the critical strain, which implies a plasticity mechanism that is universal to disordered solids with the capacity for finite plastic flow. This notion is further bolstered by the remarkable similarity of our measured scaling to that compiled from compressive behavior of MGs by Johnson and Samwer[67] and Qu et al.[186]. We further note that such scaling between strength and elastic constants has been reported in atomistic simulations of nanocrystalline alloys[187] which in the limit of diminishingly small grain sizes have been shown to exhibit cooperative mechanisms of plasticity reminiscent of metallic glasses (e.g. shear banding, pressure-sensitive yield criteria)[188].

To understand the scaling relationship in our relatively athermal colloidal pillars, we model the fundamental building block of cooperative plastic flow in the framework of Eshelby-like elasticity. Specifically, we consider the change in free energy associated with the introduction of an ellipsoidal inclusion – representing the cooperative shear transformation – in an elastic matrix subjected to an applied far-field stress. This approach is motivated by experiments[80, 81, 160, 190] and simulations[101, 191] on the de-
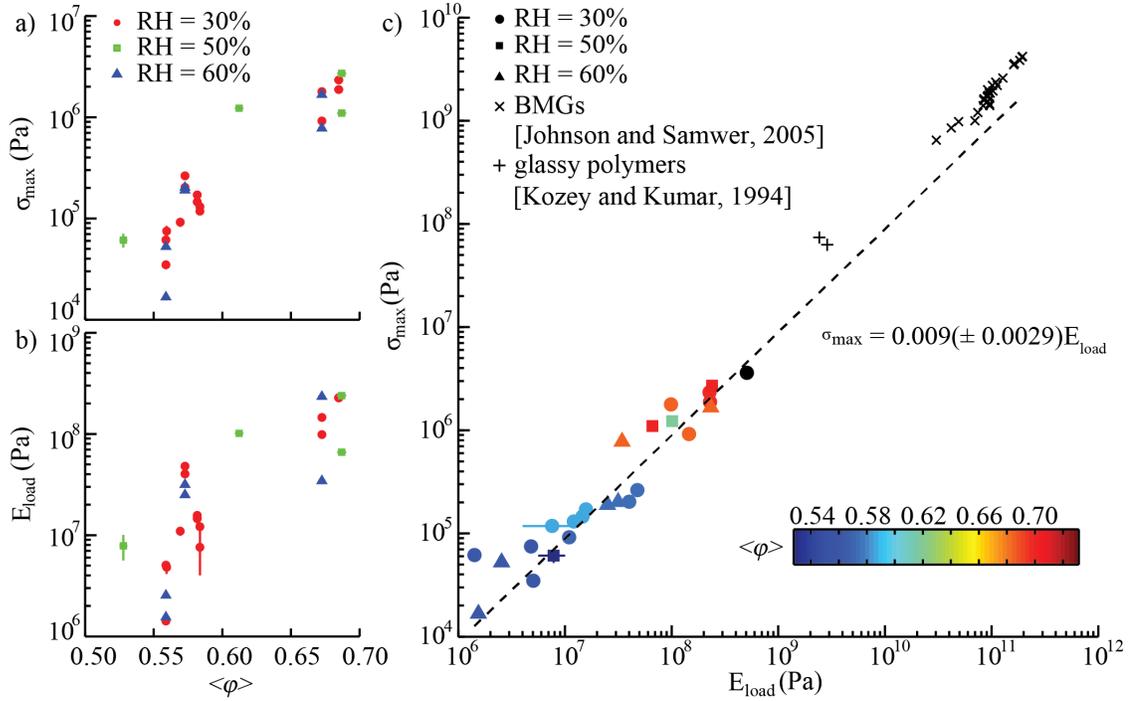
Figure 3.6: a) The normalized maximum transmitted force, σ_{max} vs. $\langle\phi\rangle$, and b) the normalized stiffness, E_{load}, vs. $\langle\phi\rangle$. c) The normalized maximum transmitted force, σ_{max}, vs. E_{load} showing a robust correlation that is relatively invariant with $\langle\phi\rangle$ (represented by data marker color; black represents pillars where $\langle\phi\rangle$ measurements were not available). Colloidal pillar measurements are compared with yield strength and Young's modulus values for metallic glasses[67] and glassy polymers[189]. The dashed line shows the best linear fit to the colloidal data with slope 0.009±0.0009, representing the critical strain for failure.

formation of amorphous solids that suggest that the fundamental plastic event is a cooperative, shear-induced rearrangement of $\sim$10-100 particles[77] referred to as a shear transformation (ST) (see Figure 3.7). After operation, in which the ST evolves from the initial to the deformed state, an elastic strain field is generated in the ST and the surrounding matrix owing to elastic compatibility. The corresponding change in the Gibbs free energy due to the introduction of an inclusion in a finite elastic matrix subjected to an applied stress has been analyzed using Eshelby's method, where the

confined transformation is modeled by allowing for a stress-free unconfined transformation followed by reinsertion into and elastic accommodation by the matrix[114, 192, 193].

In addition to the elastic energy of the confined shear transformation, the applied stress field interacts with the stress field generated by the inclusion, resulting in an extra part of the Gibbs free energy (see Appendix A). Taken together, the elastic energy and interaction terms yield a simple expression for the change in the Gibbs free energy associated with the introduction of the inclusion:

$$\Delta G = -\frac{1}{2} \int_\Omega \sigma_{ij}^I \epsilon_{ij}^T dV - \int_\Omega \sigma_{ij}^\infty \epsilon_{ij}^T dV \qquad (3.1)$$

$$\Delta G = -\frac{\Omega}{2} \sigma_{ij}^I \epsilon_{ij}^T - \Omega \sigma_{ij}^\infty \epsilon_{ij}^T \qquad (3.2)$$

Here, σ_{ij}^I is the stress field inside the confined inclusion, ϵ_{ij}^T is the unconfined transformation strain of the inclusion, σ_{ij}^∞ is the applied far-field stress, and Ω is the volume of the inclusion. The integrals are readily evaluated because the stress and strain fields inside of an ellipsoidal inclusion are spatially uniform. The stress field inside the inclusion can be written as:

$$\sigma_{ij}^I = C_{ijkl}(S_{klmn} - \delta_{km}\delta_{ln})\epsilon_{mn}^T \qquad (3.3)$$

70
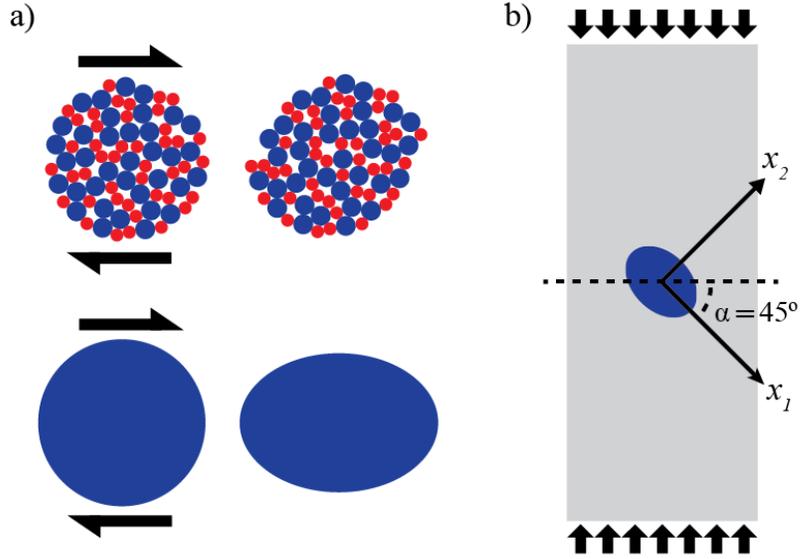
Figure 3.7: a) An idealized cooperative rearrangement induced by an applied shear stress (top row) and a continuum representation of the rearrangement (lower row). b) The reference axes defined for the energy analysis. The ellipsoids major axis, a, lies along x_1 and its minor axis, c, lies along x_2.

where C_{ijkl} is the stiffness tensor, S_{klmn} is Eshelby's tensor, and δ_{ij} is the Kronecker delta. Eshelby's tensor relates the unconfined transformation strain of the inclusion to the confined strain of the inclusion (i.e., the strain after being reinserted in the matrix)[192]. The shear bands that form in the pillars are oriented approximately 45° from the pillar axis, which is similar to the orientation of shear bands found in compressed BMGs[164] and soil pillars[194]. While it is believed that the nature of external loading may bias the orientation of shear bands (towards the pillar axis in compression[195]), we lack the ability to measure shear band orientation to such precision. Therefore, for the energy analysis we neglect any strong pressure-dependent yielding and assume a tri-axial (i.e., each axis is unique in its length, $a > b > c$) ellipsoidal inclusion with the major axis, a, lying along the direction of maximum

shear stress, $\alpha = 45°$ (see Figure 3.7). Following the work of Argon and Shi, we define the transformation strain of the unconfined inclusion as:

$$\epsilon_{ij}^T = \frac{\epsilon_o^T}{3} \begin{bmatrix} 1 & 0 & 0 \\ 0 & 1 & 0 \\ 0 & 0 & 1 \end{bmatrix} + \frac{\gamma_o^T}{2} \begin{bmatrix} 0 & 1 & 0 \\ 1 & 0 & 0 \\ 0 & 0 & 0 \end{bmatrix} \tag{3.4}$$

which can be described by the scalar dilatational strain magnitude ϵ_o^T and the scalar shear strain magnitude γ_o^T. Furthermore, we assume that the transformation dilatancy $\beta \equiv \epsilon_o^C / \gamma_o^C \approx 1$[196]. The superscript C denotes the confined transformation strain and may be related to the unconfined transformation strain with superscript T by Eshelby's tensor S_{ijkl}[196]. Assuming an isotropic elastic medium, Equation 2 reduces to:

$$\sigma_{ij}^I = \frac{2E\epsilon_o^T}{9(\nu - 1)} \begin{bmatrix} 1 & 0 & 0 \\ 0 & 1 & 0 \\ 0 & 0 & 1 \end{bmatrix} + \frac{E\gamma_o^T(7 - 5\nu)}{30(\nu^2 - 1)} \begin{bmatrix} 0 & 1 & 0 \\ 1 & 0 & 0 \\ 0 & 0 & 0 \end{bmatrix} \tag{3.5}$$

where E is Youngs modulus and ν is Poissons ratio[79]. This expression represents the self-stress of the inclusion, which is completely defined by the material's elastic constants, E and ν, and the transformation strain magnitudes ϵ_o^T and γ_o^T. For uniaxial compression and the reference basis defined in Figure 3.7, σ_{ij}^∞ can be written as:

$$\sigma_{ij}^{\infty} = \frac{\sigma}{2} \begin{bmatrix} e-1 & 1 & 0 \\ 1 & -1 & 0 \\ 0 & 0 & 0 \end{bmatrix} \tag{3.6}$$

where $\sigma = F/A_o$ is the applied stress, and compression is negative. Equation 3.1 then reduces to:

$$\Delta G = \frac{\Omega E}{\nu^2 - 1} \left[\frac{\nu+1}{9} \left(\frac{\epsilon_o^T}{\beta} \right)^2 + \frac{7-5\nu}{60} \left(\gamma_o^T \right)^2 \right] + \frac{\Omega\sigma\gamma_o^T}{2} - \frac{\Omega\sigma\epsilon_o^T}{3\beta} \tag{3.7}$$

With the assumption $\beta = 1$, ϵ_o^T can be related to γ_o^T (see Appendix A). We assume that at σ_{max}, $\Delta G = 0$, and upon a further increase in the applied stress, the introduction of an inclusion (i.e. operation of a shear transformation) becomes energetically favorable. The relationship between strength and stiffness thus becomes (see Appendix A for full expression for Θ):

$$\frac{\sigma_{max}}{E} = \gamma_o^T \Theta(\nu, \beta = 1) \tag{3.8}$$

We assume $E = E_{load}$ and values of ν between 0.15^3 and 0.45 and find a best fit for the data with γ_o^T as the free parameter. Over the range of ν considered, γ_o^T ranges from 0.026 for $\nu = 0.45$ to $\gamma_o^T = 0.033$ for $\nu = 0.15$; thus γ_o^T is largely insensitive to ν. Because our system is dissipative, the true elastic modulus is larger than the stiffness measured on loading. Assuming that 50% of the work done on the system during

loading is stored as elastic energy[12], the true elastic modulus is underestimated by a factor of 2 ($2E_{load} = E_{elastic}$, see Appendix A for load-unload measurements and evidence of quasi-linear loading). This error results in an overestimation of γ_o^T by a factor of 2. Therefore, we take $\gamma_o^T/2$ and γ_o^T as bounds on the magnitude of the characteristic transformation shear strain. Dissipation is likely a result of a combination of frictional sliding at particle contacts and ST activity. Recent experiments of sheared jammed particles at an interface [12] have shown that below a critical strain of 2%, ST activity, while present, is minimal. In this confined system, the dramatic increase in ST operation at the critical strain results in a rapid increase in the loss modulus. In our free-standing pillars, the instability manifests as macroscopic yield and the development of shear bands. Our motivation in setting $\Delta G = 0$ at σ_{max} is to extract a critical strain at which STs are sufficiently active so as to lead to shear banding.

The magnitude of γ_o^T found using this analysis of our pillar data is similar to the values found in simulations of Lennard-Jones particles[79] and experiments of sheared bubble rafts[80] in which displacement fields can be measured directly. Dasgupta et al. compared the non-affine displacement fields generated by an ST in a molecular dynamics simulation to the displacement field generated by a general Eshelby transformation strain[79]. These authors found good agreement between the fields when using a traceless Eshelby transformation strain with two non-zero eigenvalues and $\gamma_o^T = 0.08$, which agrees well with our value of ~ 0.03. Argon estimated a shear transformation strain value $\gamma_o^T = 0.125$ based on observations of bubble rafts[77] and

Argon and Shi later extracted a range of $\gamma_o^T \approx 0.10 \sim 0.14$ for MGs[196] using a viscoplasticity model. Particle-level measurements of the transformation strain around a rearrangement in a sheared colloidal glass find $\gamma_o^T \approx 0.08 \sim 0.26$[81]. Recent kinetic Monte Carlo (kMC) simulations of MGs that have been successful in capturing shear band formation employ a characteristic ST strain $\gamma_o^T = 0.10$ when determining the free-energy change associated with ST operation[114, 197, 198]. This similarity in shear transformation kinematics surprisingly extends to other classes of amorphous solids. Simulations of sheared amorphous silicon – a network glass with strongly directional bonding – show $\gamma_o^T \sim 0.015$[199]. The authors of this study note that while the characteristic size of shear transformations appears to be bonding dependent (~ 1 nm in metallic glasses, ~ 3 nm in amorphous silicon, and ~ 10 nm in glassy polymers[199]), γ_o^T remains similar across systems. Indeed, glassy polymers that are known to develop shear bands upon yielding, such as polymethyl methacrylate (PMMA)[200] and PS[201], show shear transformation strains similar to those of MGs ($\gamma_o^T \approx 0.11$ and $\gamma_o^T \approx 0.08$ for PMMA and PS, respectively[189]). See the Appendix A for a table of compiled experimental values of γ_o^T and γ_y for MGs, glassy polymers, and the colloidal pillars in this work. The robust critical strain appears to break down in glasses which show deformation morphology other than shear banding. For example, the macroscopic critical shear strain in amorphous silica nanowires that exhibit brittle behavior and cleavage fracture is $\gamma_y \approx 0.2$[202], much larger than the value found in MGs and glassy polymers. Thus, the cooperative shear mechanism discussed in this work hinges on

the intrinsic capacity for plastic flow that precedes final fracture.

3.2.5. Load-Drop Statistics

Many solids deform in discrete bursts. For example, nano-scale crystals exhibit sudden load drops or displacement bursts associated with dislocation slip when driven beyond yield[203–205]. The magnitudes of these bursts often reflect an internal length-scale, such as the spacing between dislocations[206], that is characteristic of the material's structure. In disordered solids like MGs[50] or sheared granular packings[51], these discrete events are associated with ST operation. Because an individual ST can trigger subsequent STs, the magnitudes of these events span a broad range and are emblematic of the way STs interact with one another.

A simple lattice model for plasticity makes predictions about the distribution of the magnitudes of these events[49, 207]. In the model, a solid is discretized in a lattice where each lattice site may be occupied by a particle. Lattice sites that are occupied couple to other occupied sites elastically. Each occupied site has a slip stress $\tau_{S,i}$. When the stress at site i exceeds $\tau_{S,i}$, the site slips and the stress at the site drops to an arrest threshold stress, $\tau_{S,a}$. The stress relieved from this site is then redistributed to neighboring sites; this relaxation and redistribution can then trigger more slip events. After slipping, the threshold stress is reduced by an amount ϵ, which captures the strain-softening behavior of amorphous materials.
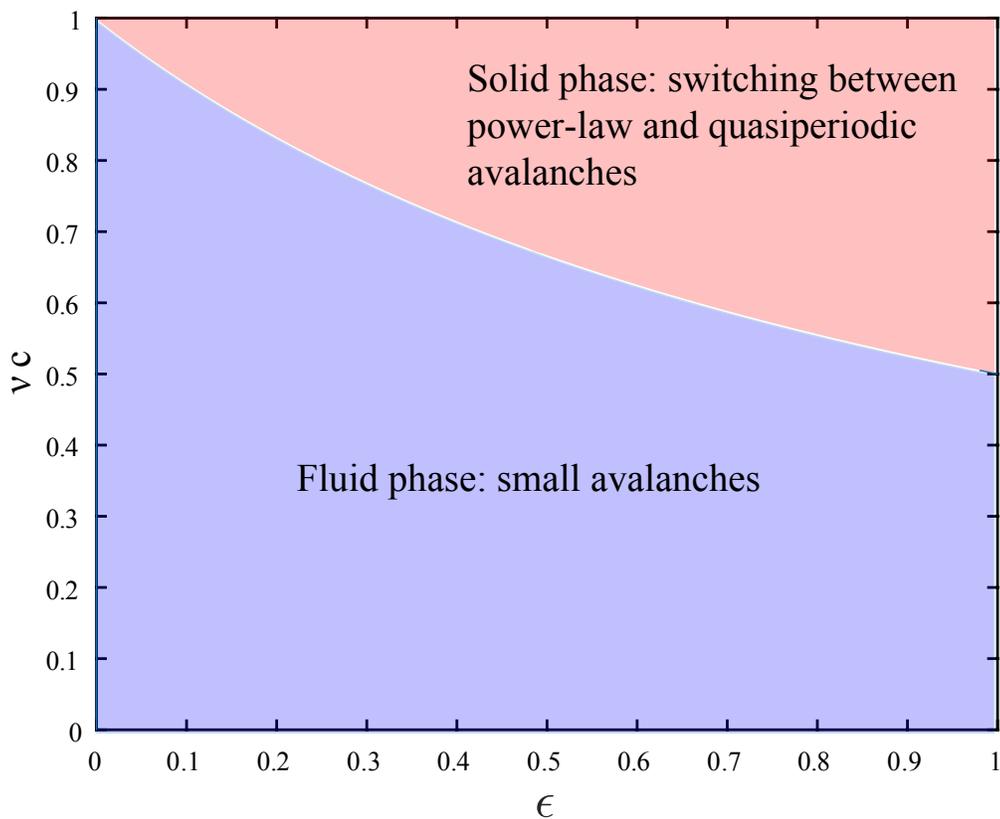
Figure 3.8: The dynamic phase behavior of the lattice model. By varying the amount of weakening (ϵ) and the packing fraction ($\phi \propto \nu c$), the material exhibits either fluid-like or solid-like behavior.

The model predicts two ϕ and ϵ-dependent dynamic phases: a fluid phase in which only small avalanches are observed and a solid phase in which both power-law and quasiperiodic avalanche statistics are found (see Figure 3.8). In the fluid phase, increased dissipation limits the elastic interaction between sites, which effectively truncates the interaction length and leads exclusively to small avalanches. In the solid phase, dissipation is less pronounced, resulting in larger, system-spanning avalanches in addition to small, localized events.

In a mean field theory solution of the lattice model, the complementary cumulative distribution, $C(\Delta S)$, of the load drops in the solid phase is given by:

$$C(\Delta S) = a \times \Delta S^{-\tau+1} exp \left[- \left(\frac{\Delta S}{\Delta S_{max}} \right)^2 \right] \qquad (3.9)$$

where a is a constant, ΔS is the magnitude of a stress drop, τ is a scaling exponent, and ΔS_{max} is a cutoff stress drop magnitude. The scaling exponent τ is predicted to be 1.5 and the cutoff stress drop magnitude should show a packing fraction-dependence where $\Delta S_{max} \sim (1 - \phi)^{-2}$.

We extract load drop statistics for the colloidal pillars at three packing fractions at 30% and 60% RH and compare the statistics to the model's prediction. For each compression cycle, a median filter with a window of 20 samples is applied to the force signal. Because the typical duration of an avalanche is several seconds for our quasi-static compression experiments and the force signal is acquired at 120 Hz, this procedure does not filter the events we are interested in. For each compression cycle, a linear fit is performed on the unloading portion of the compression cycle and the RMS error for the fit is taken as the experimental noise in the signal. We set a minimum threshold for a detectable stress-drop as 10x the RMS value of the linear fit. Because the range of the force transducer used for the ϕ=0.559 and ϕ=0.572 specimens is 0-100 mN and the transducer used for the ϕ=0.673 specimens is 0-1 N, the noise floor is not the same for each specimen. The complementary cumulative distribution function,

78
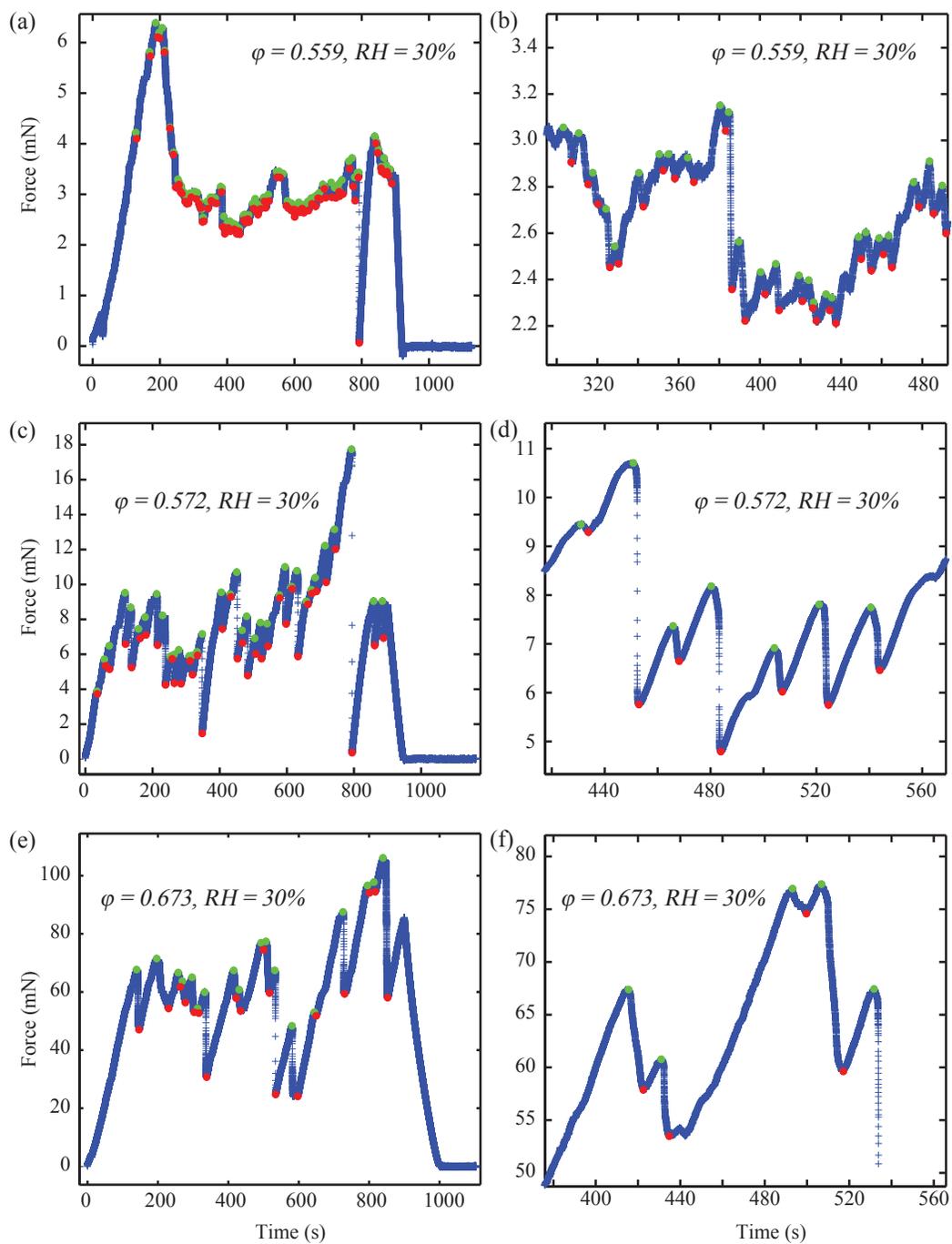
Figure 3.9: Representative compression cycles at $RH = 30\%$ for colloidal pillars with $\phi = 0.559$ (top row), $\phi = 0.572$ (middle row), and $\phi = 0.673$ (bottom row). The left column shows an entire compression cycle and the right column is a magnification that highlights the discrete force drops. Red and green circles indicate the start and end of a stress drop, respectively.

sample	τ	ΔS_{max} (Pa)	count (N)
$\phi = 0.559$, RH=30%	2.10	448000	211
$\phi = 0.559$, RH=60%	2.34	57700	285
$\phi = 0.572$, RH=30%	1.49	73600	327
$\phi = 0.572$, RH=60%	1.43	111000	223
$\phi = 0.673$, RH=30%	1.29	296000	189
$\phi = 0.673$, RH=30%	1.35	368000	205

Table 2: Colloidal pillar load drop statistics fitting parameters at various packing fractions and RHs.

$C(\Delta S)$, is then calculated for each value of ϕ and RH (see Figure 3.10).

The denser pillars ($\phi = 0.572$ and $\phi = 0.673$) generally follow the scaling prediction at both levels of RH, with $\tau \sim 1.5$ at $\phi = 0.572$ and $\tau \sim 1.3$ at $\phi = 0.673$ (see Table 2 and Figures 3.10 and 3.11). Both packing fractions show distributions with an exponential cutoff with the cutoff stress increasing for the higher packing fraction, as predicted. The number of small events is increased at 60% RH in comparison to 30% at all three packing fractions. However, the pillars with ϕ=0.559 show much different statistics than the denser pillars show: here, $\tau \sim 2.1 - 2.3$ and there is no exponential tail; these pillars exhibit the dynamic behavior predicted in the fluid regime. We cannot measure the weakening parameter ϵ directly, so it is difficult to estimate where our pillars fall on the dynamic phase diagram.

3.3. Conclusions

We have presented a method for instrumented uniaxial compression testing of colloidal pillars. The deformation behavior of pillars that form with pre-existing cracks is dominated by the propagation of these cracks. Amorphous, flaw-free pillars, on the other hand, exhibit shear banding upon yield. We also found that the water content in the pillars, which is set by RH, can dramatically alter the quasi-elastic response of the pillars. Dissipation in the pillars is lowest at $RH < 40\%$, where the capillary bridges that form between particles are distinct. Higher RH results in the coalescence of the bridges and a significant fraction of the pillars becomes saturated with water, resulting in increased dissipation.

We then performed a systematic study of the amorphous, flaw-free pillars at various packing fractions and controlled levels of RH. In these experiments, we found a strong relationship between the strength and stiffness of the pillars, independent of RH. This scaling of strength and stiffness is understood by considering the energetics of an ellipsoidal inclusion in an elastic solid; this model is founded in the kinematics of a shear transformation, which has been shown to be the fundamental plastic event in amorphous solids. At a critical value of applied stress, STs become energetically favorable and the similarity in their kinematics, which is reflected in the eigenstrain of the inclusion, makes the yield transition sharp. The robustness of the correlation between σ_{max} and E_{load} for a wide range of structural configurations brought about by mechanical annealing suggests that incipient operation of STs and macroscopic

plastic flow along shear planes occur nearly simultaneously. In other words, the transition from the quasi-elastic to plastic regimes is sharp with respect to stress. The sharpness of the transition can be inferred as a signature of a system driven in the athermal limit with a relatively narrow distribution of barrier energies defining the fundamental unit of plastic deformation. In contrast to thermal systems, such as metallic glasses, maneuvering within the complex potential energy landscape of our athermal colloidal systems is not aided by thermal activation. We assert that our system is athermal by considering the non-dimensional parameter $\frac{k_B T}{\epsilon}$, where k_B is Boltzmann's constant, T is the temperature, and ϵ is a measure of the interaction energy between particles assuming Hertzian contact. This parameter is a measure of the thermal energy relative to the elastic energy stored in the particles and vanishes in the athermal limit. For our system, $\frac{k_B T}{\epsilon} \sim 1 \times 10^{-14}$, much less than the value found in other systems treated as athermal[55]. The significance of rate effects that could arise from capillary bridge formation is quantified in the parameter $\dot{\gamma}\tau$, where $\dot{\gamma}$ is the strain rate and τ is the timescale associated with the nucleation of water capillaries. Assuming a capillary nucleation timescale similar to that measured on silicon surfaces[208], $\dot{\gamma}\tau \sim 1 \times 10^{-11}$, indicating that nucleation events occur at timescales much smaller than the timescale associated with the imposed strain. With thermal fluctuations absent, the applied stress alone surmounts the local energy maxima, ultimately driving the cooperative events. In turn, the compatibility constraint of the elastic matrix upon shear transformation (cooperative rearrangement of a collection

of particles with a characteristic shear strain γ_o^T) provides the long-range interaction to drive localized failure. Taken as a whole, the similarities in macroscopic yielding strain, characteristic ST strain, and shear band morphology between our colloidal packings and metallic glasses, despite the dissipative nature of our particle-particle interactions, lend support to the notion of a universal, cooperative plastic event unique to amorphous solids with the capacity for plastic flow.

Additionally, we collected avalanche statistics in the compressed pillars and compared our experimental data to the predictions of a discrete lattice model. For $\phi > 0.572$, we found that the stress drop statistics generally follow the prediction of the model and exhibit power-law scaling. However, at $\phi = 0.559$, the statistics are quite different – the avalanche size distribution falls off more quickly than the solid-phase exponent – and indicate a transition to fluid-like behavior.

The simple ST model for the yield strain presented here does not capture the complex dynamical interaction of activated and nucleating STs that determine the ultimate deformation morphology, which likely governs the extent of plastic deformation and the spatio-temporal evolution from individual ST operation to macroscopic shear localization. Indeed, the fluid-like stress drop statistics of the low ϕ pillars suggests that the spatial organization of the STs in this regime is distinct from the organization of STs in the higher ϕ pillars even though the yield strain in both regimes is constant. The change in flow behavior is reminiscent of the change observed in an MG's flow behavior upon cryogenic cycling[28], which appears to alter the nature of shear band

nucleation sites. As discussed in Section 1.2.4, controlling the spatial distribution of these nucleation sites is crucial when attempting to engineer toughness in MGs. An experimental technique capable of resolving the nucleation and evolution of shear bands at the particle scale is therefore necessary to attain this information. In Chapter 4, a method for *in situ* 4D compression experiments, where such data may be collected, is presented.
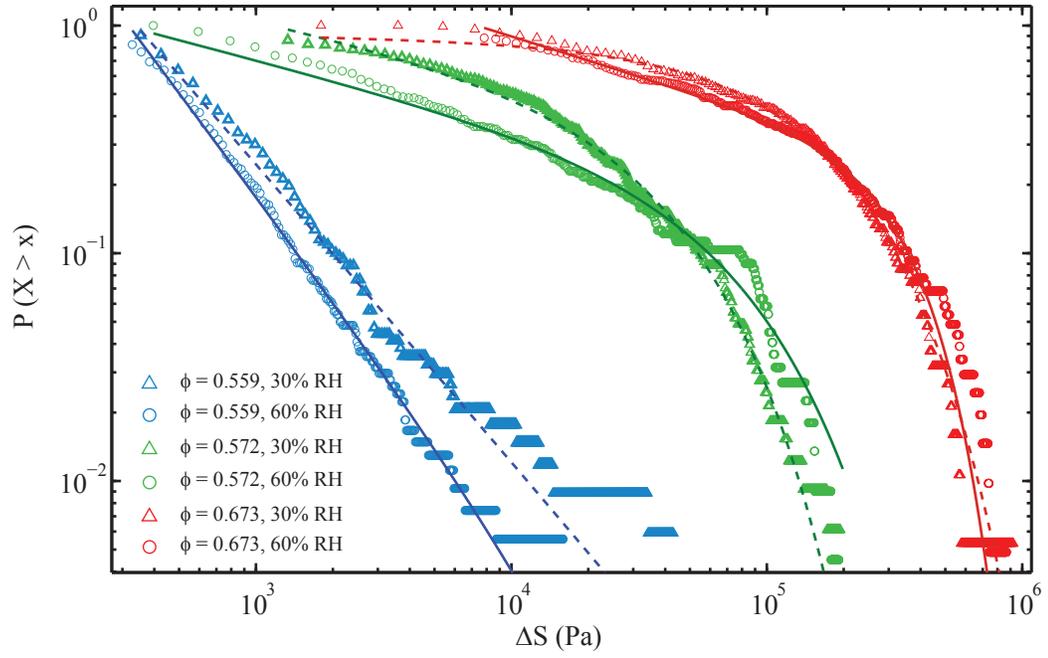
Figure 3.10: The complementary cumulative distribution functions, $C(\Delta S)$, for stress drops in the colloidal pillars.
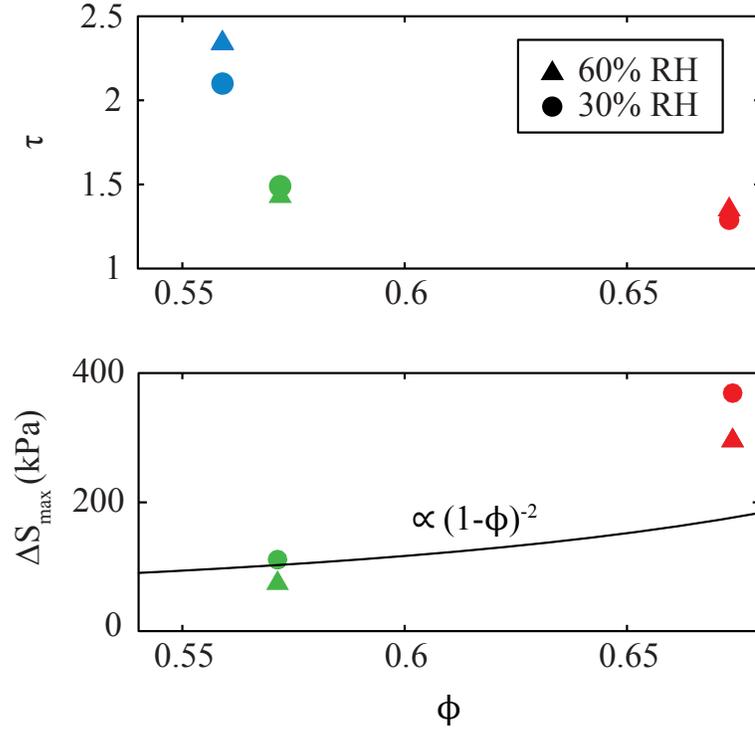
Figure 3.11: The scaling exponent τ (top panel) and cutoff avalanche size ΔS_{max} (bottom panel) as a function of the packing fraction ϕ. The denser pillars generally follow the scaling prediction at both levels of RH, with $\tau \sim 1.5$ at $\phi = 0.572$ and $\tau \sim 1.3$ at $\phi = 0.673$, while the ϕ=0.559 pillar shows much different statistics than do the denser pillars with $\tau \sim 2.1 - 2.3$. The exponential cutoff ΔS_{max} does increase with ϕ for the two densest pillars, although the increase deviates from the predicted scaling, while the ϕ=0.559 does not exhibit an exponential cutoff in $C(\Delta S)$.

Chapter 4

In-situ 4D Compression Experiments of Colloidal Pillars

The results presented in Chapter 3 establish that the plastic morphology and scaling of strength and stiffness in colloidal pillars strongly resemble the behavior observed in MGs. The experiments presented thus far are limited in that they measure only macroscopic properties of the pillars. In order to study the nascent stages of shear band nucleation and growth, particle-scale resolution is required. To achieve this, we combine a modified version of the pillar compression experiments with laser scanning confocal microscopy in *in-situ* 4D compression experiments.

4.1. Confocal Microscopy

As outlined in Section 1.3, one of the advantages of some model systems is the ability to locate individual particles in real-space. Laser scanning confocal microscopy (LSCM) is a widely used tool for imaging colloidal systems at the particle scale[154, 209]. Unlike a typical optical microscope, an LSCM uses a point-source – typically a laser – to illuminate the sample. Steerable mirrors in the microscope's optical path raster the point source across the sample. The light reflected or emitted by the sample must pass through a small pinhole located in the sample's conjugate focal plane. The pinhole

blocks out-of-focus signal and results in a small depth-of-field. After passing through the pinhole, the reflected light is collected by a photomultiplier tube or an avalanche photodiode detector and the measured signal is recorded as the pixel intensity. Each raster point results in a single pixel in the micrograph.

As mentioned previously, a major advantage of an LSCM is its very small depth-of-field in comparison to a standard optical microscope. This enhanced axial resolution makes an LSCM ideal for optical sectioning, in which a series of 2D micrographs at different focal planes are compiled into a single 3D volume. The focal plane is adjusted by precisely moving the objective lens along the optical axis. When optical sectioning is applied to fluorescent samples immersed in a medium with the same refractive index, the 3D structure of the fluorescent object can be reconstructed with high precision.

4.2. 4D in-situ Compression Experiments

The pillars used for 4D *in-situ* compression experiments are synthesized following the procedure outlined in Section 2.1.3. Briefly, these pillars are 300 μm in diameter and are composed of fluorescent 3.3 μm PMMA particles. After extruding a pillar from the capillary tube, the free-standing specimen is secured to a custom-built compression apparatus (see Figure 4.1a and b). The apparatus consists of a fluid reservoir and linkage that allow for the displacement of a piston that is sealed within the reservoir. The reservoir is filled with bromocyclohexane (CXB), which matches the refractive index of the PMMA particles. The top of the reservoir is sealed with a thin piece

of coverglass to allow for imaging using an LSCM operating in fluorescence mode with an excitation wavelength of 488 nm. During the compression experiment, high-magnification images are collected with an Olympus UPLFLN 100XO2 oil-immersion microscope. This objective was selected in part because its long working-distance of 200 μm allows for imaging deep into the pillar. A low-magnification micrograph of an extruded pillar and a high-magnification micrograph of the consituent particles are shown in Figure 4.1c and d, respectively.

The compression experiment proceeds by displacing the linkage with a piezoelectric actuator, which drives the piston and imposes a deformation on the pillar. A sequence of micrographs of the pillar is then collected. Typical displacement increments for the punch are $0.6\mu m$ ($\approx 0.2D_{part}$). A Labview (National Instruments) program is used to control the piezoelectric actuator, trigger the collection of micrographs, control the objective's piezoelectric actuator, and adjust the laser power. Each volume takes ~ 8 minutes to collect.

4.3. Particle Identification and Tracking

4.3.1. Finding and Tracking Algorithm

A 4D compression experiment results in a series of volumes – each volume being a stack of confocal micrographs – collected at each timestep in the experiment. In each volume, software is used to identify the positions of individual particles. The
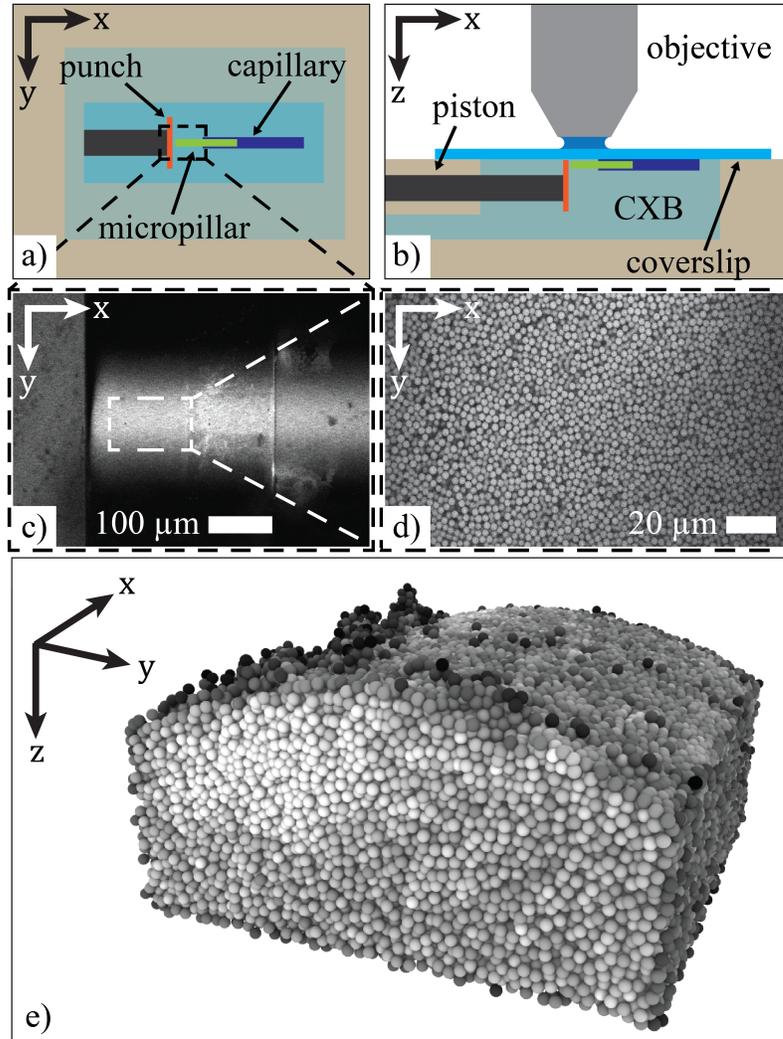
Figure 4.1: (a) A top-down and (b) side view of the experimental setup. The capillary tube containing the colloidal pillar is secured to a glass coverslip, which is fixed above a fluid reservoir. A piston with a flat punch is used to compress the exposed pillar. (c) A low-magnification image of an extruded pillar and the punch. (d) A high-magnification image of the colloidal particles that compose the pillar. (e) A 3D reconstruction of the pillar section imaged during the experiments using the identified particle positions (image generated with Ovito, see Ref 210). The particles are shaded by coordination number, highlighting the curved free surface.

positions are then linked into particle trajectories that span the entire compression experiment.

The particle identification algorithm proceeds as follows. The raw micrographs are corrected using an image flattening algorithm to eliminate optical distortion. The parameters for the flattening algorithm are selected by correcting micrographs of a target grid so that the rows are straight and undistorted in the entire field of view. After flattening, the 2D micrographs are compiled into 3D volumes. The volumes are filtered by convolution with a three-dimensional Laplacian of Gaussian (LoG) kernel, $L(x, y, z)$:

$$L(x, y, z) = \frac{1}{A} \left((x^2/\sigma_x^2 + y^2/\sigma_y^2 + z^2/\sigma_z^2 - 3) \exp \left(-(x^2/\sigma_x^2 + y^2/\sigma_y^2 + z^2/\sigma_z^2)/2 \right) \right)$$

(4.1)

where the normalization constant is $A = 2\sqrt{2}\pi^{3/2}\sigma_x\sigma_y\sigma_z$. The kernel width σ_i is chosen so that the full-width half-max of the kernel is the average particle size in pixels along each dimension, $\sigma_i = R_i/\sqrt{2\ln(2)}$. After the raw volume is filtered with the LoG kernel, local maxima in intensity are identified following the method outlined in Ref. 211 by comparing each voxel's intensity to the intensity of every neighbor in a $3 \times 3 \times 3$ pixel region. After local maxima are identified, a centroiding algorithm is used to identify particle centers with sub-voxel resolution. Prior to the centroiding, a low pass filter is applied to the raw volumes by convolution with a three-dimensional Gaussian kernel. The centroiding operation is then performed for each of the local maxima identified in the previous step. In dense samples, this operation can suffer

from systematic errors due to small particle-particle spacing and the properties of the imaging apparatus. To reduce the influence of neighboring particles, a spherical binary mask is applied around each intensity maximum, with the mask size given by the expected particle size. A recursive centroiding algorithm is then applied, referred to as "fracshift" in Ref. 212, that consists of repeating the centroiding operation until displacement between iterations is below a threshold. Gao et al.[212] showed that this recursive centroiding method is necessary to achieve subvoxel positions without bias. An example of a reconstructed pillar is shown in Figure 4.1e.

Once particles are identified in each volume, the positions are linked from volume to volume to create trajectories. Given a particle with position $\mathbf{r_i(t)}$ at time t, the tracking algorithm searches for positions at time $t+1$ within a spherical neighborhood of radius $0.5D_{part}$ of $\mathbf{r_i(t)}$. If a particle is found, position $\mathbf{r_i(t+1)}$ is added to the trajectory for particle i. The average displacement between the two timesteps is found: $\bar{\delta}(t, t+1) = \sum_i \mathbf{r_i(t+1)} - \mathbf{r_i(t)}$. Next, the positions at time t that have not been associated with a position at time $t+1$ are shifted by $\bar{\delta}(t, t+1)$. Again, the search for neighbors is performed with search radius $0.5D_{part}$. This process is repeated iteratively until the search radius is D_{part}. This process ensures that particles whose displacements deviate from the average, which is common in regions of high plastic activity, are not "lost". Trajectories that deviate most from the mean displacement are inspected visually to check for mis-identification.

4.3.2. Position Accuracy

Because all of the particle-scale structure and strain measurements depend on the precision of the particle finding algorithm, it is important to quantify the accuracy with which particle centers are determined. We make two estimates of the experimental uncertainty in locating particle centers by 1) measuring the variance in the particle displacements of a dense, quiescent sample and 2) adding random noise to particle positions and measuring the resulting noise floor in D^2_{min}.

Using a dense, quiescent sample, the variance in displacement values between timesteps is determined as:

$$\sigma_{\Delta x} = \sqrt{\frac{1}{N} \sum_{i=1}^{N} (\Delta x_i - \langle \Delta x \rangle)^2} \tag{4.2}$$

where $\langle \Delta x \rangle$ is the mean displacement. The variances in each dimension between timesteps are shown in Figure 4.2a and the average variances for all timesteps are shown in Table 3. Because the pillar used for this measurement approaches the random close packing limit, the mobility of particles is extremely small and the displacements can be used as a noise floor for our particle finding accuracy. As expected, the uncertainties in the x and y dimensions are smaller than in the z dimension. This is a result of the larger voxel size in the z-dimension and the inherently lower resolution along the optical axis. Overall, the particle identification accuracy is quite good, with uncertainty in x and y of ~1.7% of the particle diameter and uncertainty in z of

~2.4% of the particle diameter.

dimension	$\sigma_{\Delta x}(\mu m)$	$\sigma_{\Delta x}/D_{part}$
x	0.0568	0.0172
y	0.0547	0.0166
z	0.0775	0.0235

Table 3: Particle position uncertainty in 4D *in-situ* compression experiments.

A second estimate of the uncertainty in particle positions is made by adding a displacement of fixed magnitude and random direction to the positions identified at $t = 0$. Using the displaced positions, we calculate D^2_{min} according to the procedure outlined in Section 4.4. The noise floors in D^2_{min} for displacement magnitudes of 20 nm, 50 nm, 100 nm, and 250 nm are shown in Figure 4.2. The experimental noise floor lies between 50 nm and 100 nm of random noise, which agrees well with the RMS displacement uncertainty estimate of $\sim 60 - 80 \ nm$.

4.4. Results and Discussion

The fraction of successful compression experiments is quite low and we were only able to capture the growth and operation of a shear band in a single experiment. Some of the issues contributing to the low experimental yield were the pillars' propensity to break apart upon filling the reservoir with CXB, a restricted field-of-view which
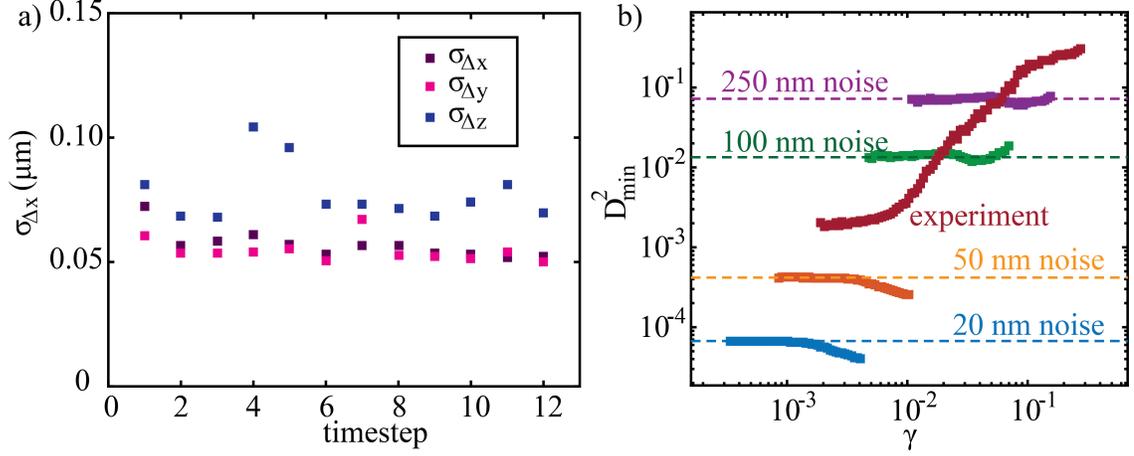
Figure 4.2: D_{min}^2 as a function of strain for four magnitudes of random particle displacements. The experimental noise floor in D_{min}^2 (red markers) lies between the 50 nm and 100 nm random displacements, which agrees with the position uncertainty estimate of $\sim 60 - 80 nm$ from the RMS displacement values.

resulted in shear bands that formed outside the imaging region being lost, and shear banding that occurred with such large displacements between timesteps that particle tracking was made impossible. The results discussed in the following Section focus on the details of the experiment in which we were able to capture the growth of a single shear band. In this experiment, we focus on the interplay of structure and response in an operating shear band.

4.4.1. Measures of Strain and Structure

We quantify strain in the pillar at the particle scale. First, we find the best affine deformation tensor J_k for particle k. J_k maps particle k's neighbors at time t to their positions at time $t + \Delta t$ by minimizing the total non-affine displacement[78]:

$$D^2_{min,k} = \frac{1}{N} \sum_{i=1}^{N} [\, r_i(t + \Delta t) - J_k r_i(t) \,]^2$$

A particle's neighbors are identified using a cut-off distance of $2D_{part}$. $D^2_{min,k}$ can be interpreted as diffusive-like deformation that cannot be accounted for with a combination of rotation and strain operations. The strain tensor ϵ_k is found by extracting the symmetric part of J_k:

$$\epsilon_k = \frac{1}{2}[J_k + J_k^T]$$

which allows for the calculation of the shear strain $\gamma_k = \sqrt{\frac{1}{2}Tr(\epsilon_k - \Delta_k I)}$ where $\Delta_k = \frac{1}{3}Tr(\epsilon_k)$ is the hydrostatic strain invariant. Once strain is calculated, we determine the spatial autocorrelation of $\gamma(r)$ at each timestep as:

$$\chi_\gamma(\mathbf{dr}) = \frac{\langle \gamma(\mathbf{r})\gamma(\mathbf{r} + \mathbf{dr})\rangle - \langle\gamma(\mathbf{r})\rangle^2}{\langle\gamma(\mathbf{r})^2\rangle - \langle\gamma(\mathbf{r})\rangle^2} \tag{4.3}$$

We calculate several measures of the macroscopic and particle-scale structure. The packing fraction, ϕ, in a volume V is calculated as:

$$\phi = \frac{N}{V}\frac{\pi D^3_{part}}{6} \tag{4.4}$$

96

We also perform a Voronoi tesselation and extract the volumes, $V_{Voronoi}$, of the resulting polyhedra. The three-dimensional radial distribution function, $g(\mathbf{r})$, is calculated following the procedure in Appendix B. From $g(\mathbf{r})$, the isotropic pair correlation function $g(r)$ is calculated by integrating $g(\mathbf{r})$ in a spherical shell of radius r. Local structural anisotropy is not captured in ϕ, the $V_{Voronoi}$ statistics, or $g(r)$. It has been shown that the structural distortion that occurs during shear deformation of glasses is quite anisotropic[128, 129, 213], and a more detailed measure of the local structure is necessary to resolve this anisotropy. We measure a directional coordination, $Z(\theta, \omega)$, which can be extracted from the pair correlation function, $g(\mathbf{r})$, as follows. After calculating $g(\mathbf{r})$, a direction vector is chosen at an orientation parameterized by azimuthal angle ω and elevation angle θ (see Figure 4.5). A cone with its axis along the direction vector is defined so that the solid angle of the cone is given by Ω. All points within the cone are selected, and then the directionally dependent coordination $Z(\theta, \omega) = \int_0^{r_{min}} \eta g(\mathbf{r}) \, d\mathbf{r}$ is calculated where r_{min} is the value of r at the first minimum in $g(r)$ and η is the particle number density N/V.

4.4.2. Discussion

We observe strain concentrated in a region near the interface with the punch, which is hereafter referred to as "the shear band" (see Figure 4.3). Further from the punch, the pillar remains relatively undeformed and this region will be referred to as "the matrix". A timestep t refers to a specific volume with $t = 0$ corresponding

to the first volume collected. The shear band was somewhat deformed before the first timestep, so the nascent nucleation of the shear band is not captured in this experiment (see Figure 4.3b, c, and d).

However, we are able to observe the evolution of this already-nucleated shear band as deformation proceeds and find that its maturation shows a striking resemblance to a localized, shear-driven colloidal glass transition. The shear band region dilates such that ϕ decreases to approximately the colloidal glass transition value $\phi_g \approx 0.58$. We note that the exact value of ϕ_g for hard-sphere colloids remains uncertain and may have some dependence on the polydispersity of the system[214–216]; this is reflected in the shading of Figure 4.3b. Further compression does not decrease ϕ further. Dilation is also visible in the evolution of the distribution of Voronoi volumes $P\left(V_{Voronoi}\right)$ (Figure 4.3c and d), which shifts to a higher mean value and broadens, reflected particularly in the large volume tail. The matrix, on the other hand, shows little dilation and a nearly static $P\left(V_{Voronoi}\right)$. $g\left(r\right)$ in the shear band and in the matrix shows broadening of the nearest neighbor peak (Figure 4.3a and b). Density beyond the first neighbor shows significantly more evolution in the shear band than in the matrix.

Figures 4.5b and c show the directional coordination, $Z(\theta, \omega)$, in the matrix and shear band, respectively, at three timesteps. It is apparent that the shear
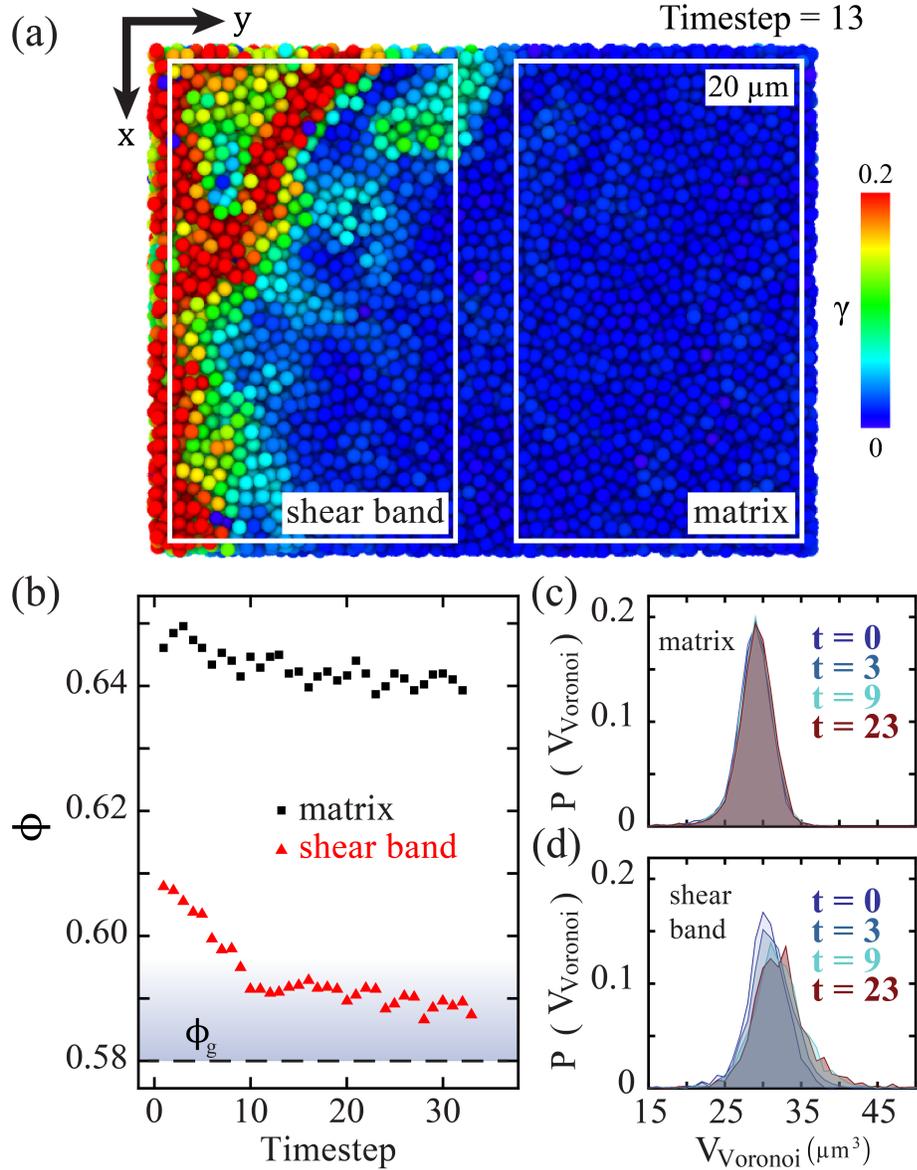
Figure 4.3: (a) Shear strain in a slice of the pillar at $t = 13$. Strain is localized in bands near the punch. The white rectangles indicate the delineation of the "shear band" and "matrix" regions. (b) The evolution of the packing fraction, ϕ, in the shear band and matrix. Significant dilation is measured in the shear band from $t = 0$ to $t = 10$, after which point ϕ remains approximately constant. The matrix shows little dilation. The shaded region highlights the range of ϕ_g reported in polydisperse colloidal systems[214]. The distribution of Voronoi volumes in the matrix (c) and shear band (d). The distribution in the matrix is static, while the distribution in the shear band evolves to a larger mean volume as deformation proceeds.
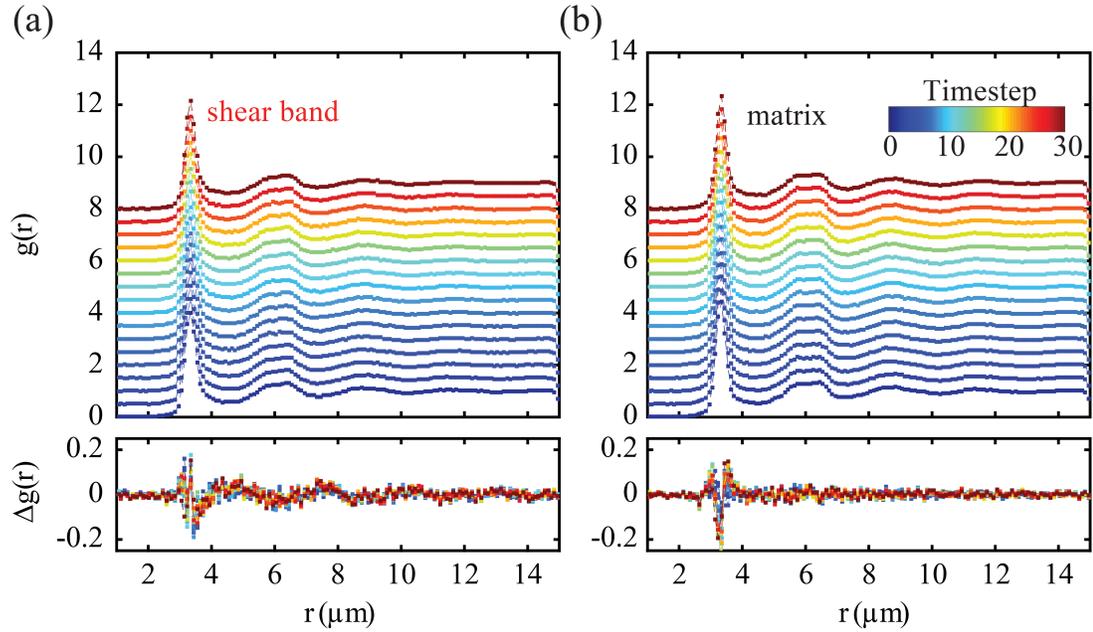
Figure 4.4: The radial distribution function $g(r)$ (top row) and change in $g(r)$ (bottom row) at different timesteps for a) the shear band and b) the matrix. The $g(r)$ plots are offset for clarity. Both the shear band and matrix show subtle changes in nearest neighbor peak height and location during deformation. The shear band shows extended fluctuations for $r \sim 4 - 8 \mu m$ while $g(r)$ in the matrix is unchanged at these distances.

band, which was pre-deformed at $t = 0$, is, on average, under-coordinated with respect to the matrix, with particular under-coordination along $\{\theta \approx \pi/2, \omega \approx \pi\}$ (see Figures 4.5d and e for the mean, minimum and standard deviation in Z for the matrix and shear band). As deformation proceeds, Z in the shear band continues to decrease and becomes more anisotropic, which is reflected in the increasing standard deviation in Z (Figure 4.5e), with the most under-coordinated directions finally lying along $\{\theta \approx \pi, \omega \approx \pi\}$ and $\{\theta \approx 0, \omega \approx 0\}$. The closest-packed directions are along $\{\theta \approx \pi/4, \omega \approx \pi/2\}$ and $\{\theta \approx 3\pi/4, \omega \approx 3\pi/2\}$, which correspond to directions of minimum (deviatoric) shear for the uniaxial compression geometry. This result is

in contrast to previous studies, which find more coordination along directions of high shear[129].

It has long been recognized that shear transformations in amorphous solids result in an increase in the free volume in the region around the shear transformation[75, 77, 217, 218]. In thermal systems, the competition between shear-induced generation of free volume and diffusion-driven annihilation of free volume results in temperature and strain rate dependent flow behavior. At high temperatures and low strain rates, free volume diffusion and annihilation can suppress run-away free volume generation, resulting in homogeneous plastic flow. At lower temperatures and high strain rates, annihilation cannot keep up with free volume generation, and strain localization, or heterogeneous plastic flow, occurs. For our nearly athermal, hard-sphere system, we expect that the annihilation of any excess free volume is insignificant in comparison to the shear-driven generation, thereby resulting in overall dilation with increasing strain. What is striking, however, is how abruptly the dilation process in our experiments terminates at the transition ϕ.

It is apparent that the shear band, which was pre-deformed at $t = 0$, is, on average, under-coordinated with respect to the matrix, with particular under-coordination along $\{\theta \approx \pi/2, \omega \approx \pi\}$ (see Figures 4.5d and e for the mean, minimum and standard deviation in Z for the matrix and shear band). As deformation proceeds, Z in the shear band continues to decrease and becomes more anisotropic, which is reflected in the increasing standard deviation in Z (Figure 4.5e), with the most under-coordinated

101

directions finally lying along $\{\theta \approx \pi, \omega \approx \pi\}$ and $\{\theta \approx 0, \omega \approx 0\}$. The closest-packed

directions are along $\{\theta \approx \pi/4, \omega \approx \pi/2\}$ and $\{\theta \approx 3\pi/4, \omega \approx 3\pi/2\}$, which correspond

to directions of minimum (deviatoric) shear for the uniaxial compression geometry.

This result is in contrast to previous studies, which find more coordination along

directions of high shear[129].

Figure 4.5: (a) The spherical coordinate conventions used to determine the average coordination along a given direction. A cone with solid angle Ω and its axis along a vector with azimuthal angle ω and elevation angle θ is defined. All points in $g(\mathbf{r})$ within the cone are selected, and vector with azimuthal angle ω and elevation angle θ is defined. Integration along the direction vector yields $g(r)$, which is then used to determine the coordination. The angular coordination in the matrix (row (b)) and the shear band (row (c)) at three timesteps. Little change in the coordination is observed in the matrix. The shear band, however, shows a decrease in the mean coordination and a decrease in the anisotropy of the coordination. These changes in Z in the matrix and shear band are quantified in (d) and (e), respectively, which show the evolution of the mean and minimum of Z with timestep. The error bars represent the standard deviation in Z, which is clearly enhanced in the shear band.

In stark contrast, Z in the matrix shows little change in both the mean and

minimum coordination (see Figure 4.5d). On average, the shear band lacks one

neighbor in comparison to the matrix, with the most under-coordinated directions

having only ~ 10 neighbors in comparison to the matrix's mean value of 12. The evolution of Z in the shear band shows the same behavior as ϕ in that it remains static after $t = 10$.
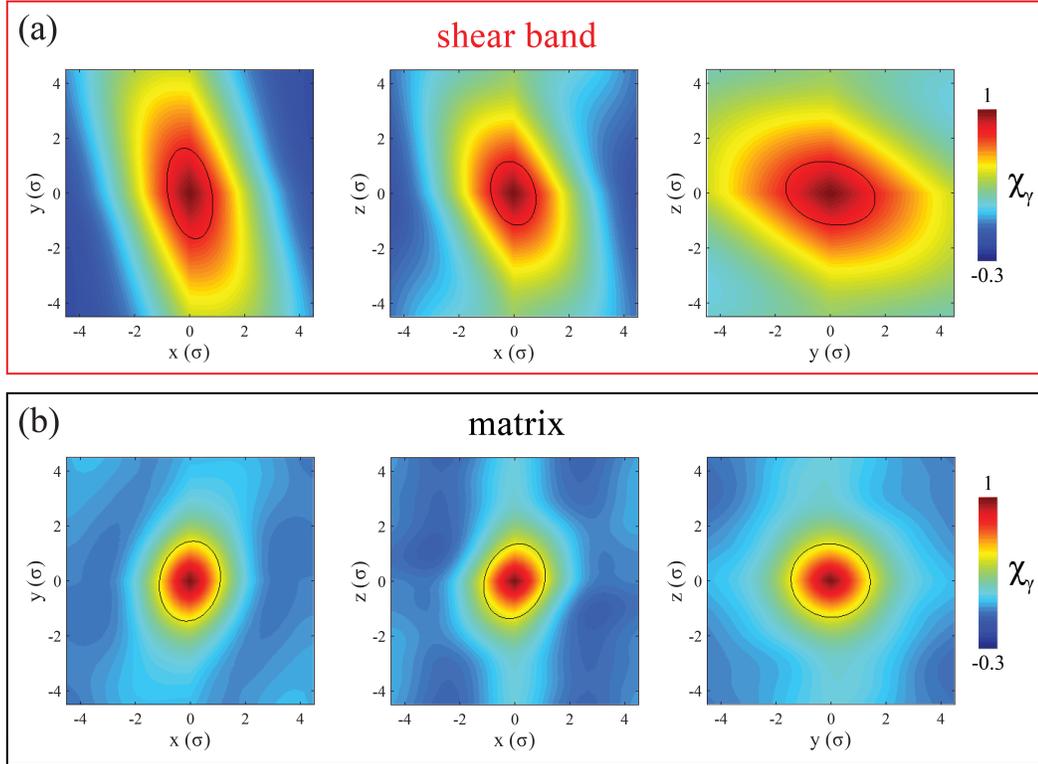
Figure 4.6: Slices along the x-y, x-z, and y-z planes of the strain correlation functions in both the a) shear band and b) the matrix. An ellipsoid is fit to an iso-intensity surface of the 3-D correlation. The decay along the ellipsoid's major axis is used to quantify the maximal extent of the correlation, as shown in Figure 4.7. The anisotropy of the ellipsoid is quantified by the ratio of the major axis length to the minor axis length.

Evidently, compression drives significant changes in the structure within the shear band. To quantify how this structural change affects mechanical response, we analyze spatial correlations in shear strain. χ_γ is found to be quite anisotropic, but generally ellipsoidal, with particular directions exhibiting strong correlation at large

distances. The correlation is shown at three timesteps in both the shear band and the matrix in Figure 4.6. To quantify changes in the correlations as deformation proceeds, an ellipsoid is fit to an iso-intensity surface for each $\chi_\gamma(dr)$. The value of χ_γ along the ellipsoid's major axis (see Figure 4.7a and b) is a measure of the maximum extent of the correlation in strain. At each timestep, we find the value of $\chi_\gamma(\sigma = 10)$ where $\sigma = r/D_{part}$. These values are plotted against ϕ at the same timestep in Figure 4.7c. In the matrix, the correlations are relatively unchanged throughout the experiment, with zero correlation beyond $\sigma = 4$, suggestive of minimal plastic activity. Note that for our definition of the correlation, uniform strain, as would be expected in perfectly elastic response, results in $\chi_\gamma(\mathbf{dr}) = \mathbf{0}$ everywhere. In the shear band, the spatial extent of the correlations is much larger initially and decays as deformation proceeds. At $\phi > 0.60$, the correlation at $\sigma = 10$ is significant with $\chi_\gamma(\sigma = 10) \approx 0.2 - 0.4$. Further dilation, however, reduces $\chi_\gamma(\sigma = 10)$. Notably, the timestep where $\chi_\gamma(\sigma = 10) \to 0$ corresponds to the same timestep where both ϕ and Z sharply saturate. This decay in the extent of correlations in shear strain signifies a transition from a solid-like to liquid-like response, which accompanies the changing structure within the shear band. We also find that the anisotropy of the correlation, quantified by the ratio of the ellipsoid's major to minor axis, decays with dilation in the shear band from $\simeq 3$ to $\simeq 1.5$. The correlation in the matrix is isotropic, with anisotropy values $\simeq 1.1$ that persist throughout the experiment.
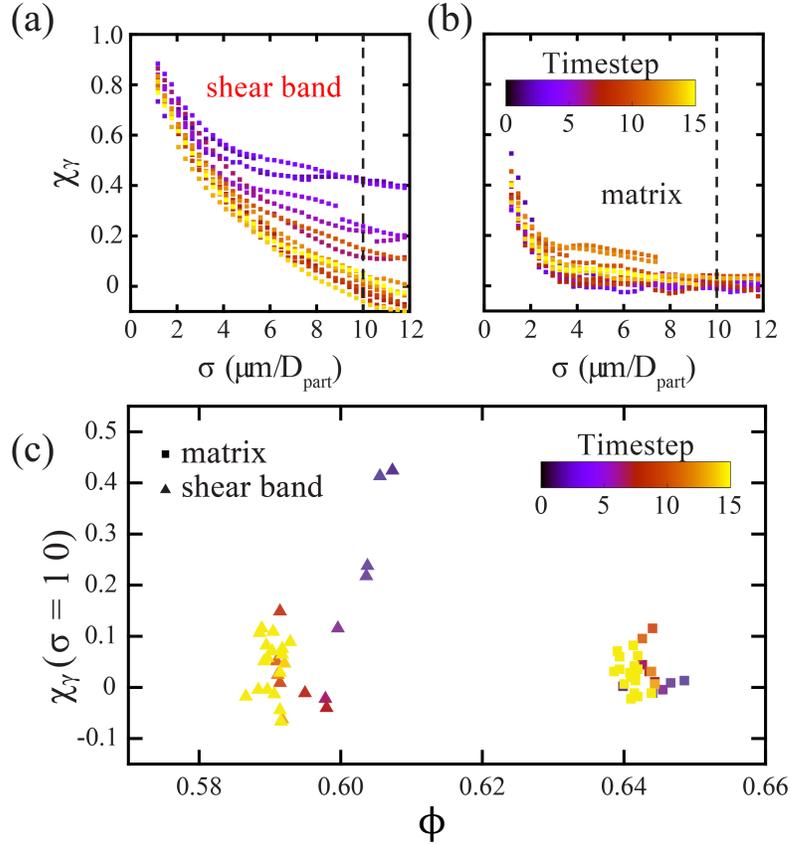
Figure 4.7: Decay of the strain autocorrelation χ_γ along the major ellipsoidal axis in both the a) shear band and b) matrix at different timesteps. c) The strain correlation at 10 particle diameters $\chi_\gamma (\sigma = 10)$ at various packing fractions. Data points for $t \geq 15$ have the same coloring.

4.5. Confined Compression Experiments

As discussed in Section 1.2.2, a new machine learning based approach has proven to be effective in predicting rearrangements in amorphous solids. The technique is dependent upon many structural descriptors of a particle's neighborhood; therefore, real space structural data is required to apply the method. Additionally, the accuracy of the method is improved by including many rearrangement events when determining the hyperplane that separates "hard" and "soft" particles[219]. The application of the

softness method to shear banding has the potential to engender robust definitions of a critical shear band nucleus and a mature shear band, both of which would mark significant advancements in our understanding of plasticity in glasses. However, the pillar geometry discussed thus far is not conducive to collecting the volume of data necessary for applying the softness method; capturing the shear band in the microscope's field of view is challenging, resulting in many experiments with minimal amounts of plastic activity that are not useful for hyperplane determination.

A more apt geometry for collecting large amounts of data is a confined compression cell. Here, a small reservoir is filled with a dense suspension of the fluorescent $d = 3.3~\mu m$ PMMA particles. The reservoir is constructed such that one wall is movable, which allows for the packing to be deformed (see Figure 4.8a and b). The top of the reservoir is sealed using a thin piece of coverglass to allow for imaging using the confocal microscope.

The deformation experiment proceeds by displacing the movable wall via a piezo-electric actuator and then collecting a sequence of micrographs of the packing that are assembled into a volume. The volumes collected are always tens of particle diameters away from any walls to minimize the effects of boundaries. Typical displacement increments were $0.6\mu m$ ($\approx 0.2d$). The displacement profile imposed is a sine wave with increasing amplitude from one cycle to the next. The same algorithm outlined in Section 4.3 is used to identify particles and determine trajectories.
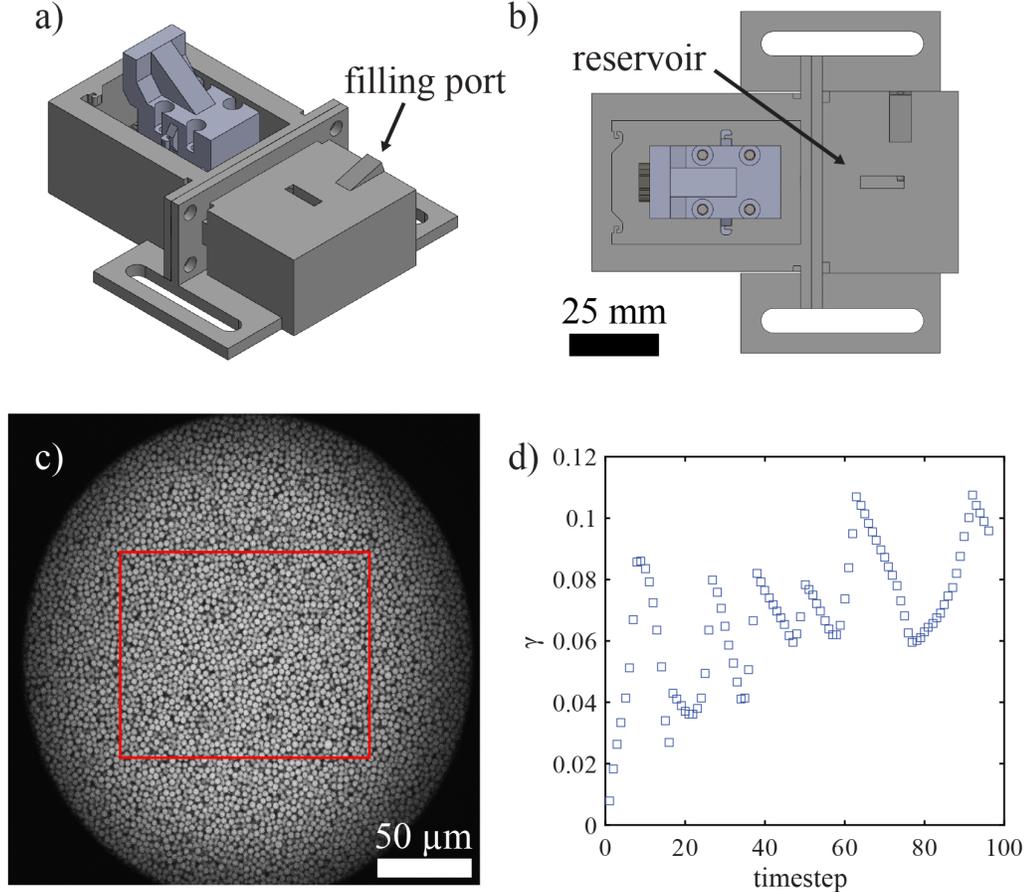
Figure 4.8: (a) Isometric and (b) top-down views of the compression cell for the confined compression experiments. The reservoir is filled by injecting a syringe containing a concentrated suspension of colloidal particles. A piezoelectric actuator is used to displace one of the walls of the reservoir. (c) A confocal micrograph of the dense suspension in the reservoir. The red box denotes the box that is used to define macroscopic deformation. (d) The macroscopic shear invariant generated during a cyclic displacement experiment. While the displacement applied by the piezoelectric actuator is sinusoidal, the displacement transmitted to the piston deviates from applied displacement due to hysteresis and slip in the linkage. Moreover, dissipation within the colloidal packing itself results in complicated displacement profiles.

To quantify the rearrangement of particle i between times t and $t + \Delta t$, we calculated $D^2_{\min}(i; t)$ following Equation 4.2. A particle i at time t is said to be rearranging if $D^2_{\min}(i, t) > D^2_{\min,0}$. Here, we chose $D^2_{\min,0} = 0.075 d^2$.

Because the imposed deformation was not uniform between timesteps, the incremental strain also varied non-uniformly between timesteps. To place the times t and $t + \Delta t$ on equal footing, we constructed an artificial box near the boundaries of the imaging volume. From one timestep to the next, we map the deformation of the box using the displacements of particles within a small distance of the planes that define the box's faces. We then use the displacements of the box's corners to find the displacement gradient tensor, $\mathbf{J}$, and the macroscopic strain tensor $\boldsymbol{\epsilon} = \frac{1}{2}\left(\mathbf{J}^{\mathbf{T}}\mathbf{J} - \mathbf{I}\right)$. We calculate the shear (deviatoric) invariant:

$$\gamma = \sqrt{\frac{1}{2}Tr\left(\boldsymbol{\epsilon} - \epsilon^{m}\mathbf{I}\right)^{2}}, \tag{4.5}$$

of the system between timestep t and each subsequent timestep t'. Here, $\epsilon^{m} = \frac{1}{3}Tr\boldsymbol{\epsilon}$ is the hydrostatic strain invariant. Then, for each timestep t, we chose Δt so that the shear invariant of the system was greater than a threshold, $\gamma > \gamma_0$. In this case, we chose our threshold to be $\gamma_0 = 0.04$.

We characterized the local structure around particle i with a set of $M = 157$ structure functions, defined as:

$$G(k; \mu) = \sum_i \mathrm{e}^{(r_{ik} - \mu)^2 / L^2} \tag{4.6}$$

$$\Psi(k; \xi, \lambda, \zeta) = \sum_{i,j} \mathrm{e}^{\left(r_{ik}^2 + r_{jk}^2 + r_{ij}^2\right)/\xi^2} \left(1 + \lambda \cos \theta_{kij}\right)^\zeta \tag{4.7}$$

The summations are performed for all particles within a radius R_c^{S}[108]. Our results are insensitive to changes in R_c^{S} so long as we include the first few neighboring shells[108]. In this work, we set $R_c^{S} = 2.5d$ and fixed $L = 0.05d$.

It was found that particles with diameters less than $0.95d$ (as estimated by the method described in Ref. 220) were significantly more mobile than larger particles. To ensure that our SVM really classified rearrangements and not simply large and small particles, we excluded these particles from our training set. Because particles near the boundary of the imaged volume have fewer neighbors than particles in the interior, the structure functions in these two regions differ. This difference could throw off our training. Thus, we also excluded particles less than $2.5d$ from the boundary from our training set. To construct our training set, we then chose all $N_r = 739$ rearranging particles in our system, and $N_n = 739$ particles from $t = 20$ with the lowest cumulative D_{min}^2 over $\tau = 76$ timesteps, 78% of the length of the experiment, as non-rearranging particles[221]. Typically, τ is chosen to be on the order of the relaxation time of the system, but because so few particles rearranged in this experiment, τ was chosen to be large with respect to the length of the experiment but also to avoid the

aging regime near the beginning of the experiment. This value of τ is more than 10 times the average lag time, Δt, chosen for the instantaneous D^2_{min} calculations used to determine rearrangements.

It is not possible to specify a hyperplane that completely separates rearranging particles from non-rearranging ones. Thus, the SVM is designed to penalize particles whose classification is incorrect. This misclassification penalty is controlled by the parameter C where larger C values correspond to fewer incorrect classifications. This parameter was chosen to be $C = 1.0$ by nested cross validation[222]. For this value of C, we find that 77% of rearrangements occur at particles with softness $S > 0$.

After determining the best hyperplane, the softness of particles in the shear banding pillar is calculated (see Figure 4.9a). Not surprisingly, soft particles (softness > 0) are concentrated in the shear band and the population of soft particles increases up until $t = 10$, generally following the behavior of ϕ. Again, because the incipient nucleation of the shear band is not captured in the experiment, we are not able to observe the initial evolution of softness near the punch-pillar interface.

Figure 4.9b shows only the soft particles in the pillar at $t = 25$ (the particle shading is by z position to enhance perspective). Clearly, the soft particles are concentrated in the shear band. We investigated whether a change in the density of soft particles or their connectivity showed an abrupt change at $t = 10$. While the density of soft particles does stop evolving after this point, defining a critical density
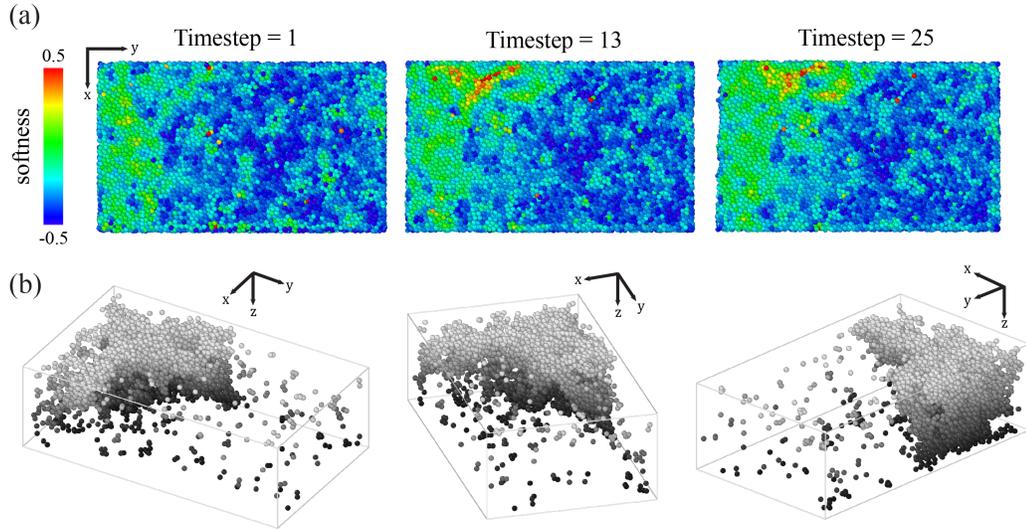
Figure 4.9: (a) An operating shear band in a colloidal pillar colored by softness. The plane shown is the same as the plane shown in Figure 4.3. Soft particles are concentrated in the shear banding region. This concentration is evident in panel (b), which shows only the soft particles in the pillar at $t = 25$. The particles are shaded by their z position to enhance visibility.

is challenging because of the complex geometry of the shear band. No obvious change in the connectivity of the particles was found at this timestep.

4.6. Conclusions

We have presented a method to perform 4D *in-situ* compression experiments on colloidal pillars that allow for the acquisition of individual particles trajectories. While we were unable to capture the nucleation of a shear band during one of these experiments, we were able to observe the maturation of an already-nucleated shear band. The results show that continued deformation induces a transition, as measured by ϕ, Z, and χ_γ, that is found to be quite abrupt despite our crude partitioning of

shear band and matrix regions. Indeed, a significant fraction of the shear band region remains rather undeformed (see Figure 4.3). We adjusted the size of the shear band region to test whether the observed trends in ϕ, $P(V_{Voronoi})$, and $\chi_\gamma(\sigma = 10)$ are sensitive to the size of the region considered. This exercise demonstrates that the exact values are sensitive to the size of the region considered, but the general trends are independent of the exact dimensions.

Overall, our results quantitatively support the interpretation of shear banding as a driven, localized glass transition and therefore supports the equivalency proposed in Section 1.2.2. Quasi-static deformation drives a reduction in ϕ in a thin band of the solid until ϕ approaches ϕ_g, at which point there is a sharp transition and dilation ceases. Dilation is accompanied by a decay in the extent and anisotropy of spatial correlations in strain, signifying a transition from solid-like to liquid-like response. While we cannot rule out a first-order transition in the particle dynamics, the observed continuous changes in structure and mechanical response are consistent with the behavior of a glass as it approaches the glass transition from the solid phase. By definition, the spatial extent of the changes in structure and response is heterogeneous, and the resulting microstructure is clearly distinct from a microstructure that may be obtained from isotropic dilation, which is consistent with the conclusions drawn in [137, 138]. Our results, providing the microscopic origins of such driven transitions, lend credence to an equivalency between mechanical shear banding and the glass transition provided that careful consideration of the spatial extent of the system is

given.

Additionally, we applied the recently introduced "softness" approach to identifying particles that are particularly susceptible to rearranging using a confined compression cell. Here, a dense colloidal glass is deformed under cyclic, confined compression and individual particle trajectories are determined. These trajectories are used in the determination of the "softness" hyperplane, which is then applied to the particles in the shear banding pillar. As expected, the shear band is found to have an excess of soft particles in comparison to the matrix region, although no abrupt change in their density or connectivity is found at the transition from solid-like to liquid-like behavior.

Chapter 5

Conclusions and Prospectives

In this dissertation, we have described the mechanical properties of colloidal assemblies. First, we discussed instrumented uniaxial compression tests in which the macroscopic response of the pillars is measured. In amorphous, flaw-free pillars that exhibit shear banding, a scaling of strength and stiffness similar to that observed in MGs is found. To understand this relationship, we considered the energetics of the critical events underlying shear banding. The universal kinematics of the events result in a characteristic yield strain, which is reflected in the scaling relationship between strength and stiffness. Building on these experiments, we developed an apparatus to perform *in situ* 4D compression experiments on the colloidal pillars. In these experiments, the positions of individual particles are determined in real space, thereby allowing for the quantification of particle-scale structure and deformation. In one of these experiments, we were able to observe the maturation of a shear band at the particle-scale. We found a transition from solid-like to liquid-like mechanical response and structure that accompanied deformation in the shear band. Finally, we performed preliminary confined, *in situ* 4D compression experiments on a colloidal glass.

Our experiments are by no means exhaustive of the colloidal pillar modality's potential. There remain promising avenues for further experimentation with the colloidal pillars, several of which we discuss below. In addition, we consider alternative

loading geometries that may be more amenable to addressing certain outstanding questions and more forgiving experimentally. Finally, we highlight the application of confocal microscopy to study of a practical fabrication method.

5.1. Key Findings

- We demonstrated the synthesis of novel, free-standing pillars composed of colloidal particles by using capillary tubes as templates. Pillars composed of particles less than $\sim 1\mu$m in size were found to dry with a significant population of cracks. Pillars composed of larger particles dry without visible cracks. An amorphous pillar structure can be attained by using a bidisperse mixture of particles.

- We developed an apparatus to perform instrumented uniaxial compression on the free standing colloidal pillars. A piezoelectric actuator is used to impose deformation on the pillar and the transmitted force is measured using a load cell. The pillar is positioned in the field of view of a white-light optical or laser scanning confocal microscope to allow for micrographs to be collected during compression.

- The deformation behavior of pillars that form with pre-existing cracks is dominated by the propagation of these cracks.

- Amorphous, flaw-free pillars exhibit shear banding when deformed in uniaxial

compression. The plastic morphology of these pillars is strikingly similar to the morphology observed in metallic glass micropillars.

- The ambient relative humidity, which controls the water content in the colloidal pillars, alters the quasi-elastic response of the pillars. Plastic dissipation in the pillars is lowest at humidity levels less than 40%, where the capillary bridges that form between particles are distinct. Higher humidity levels result in the coalescence of the bridges and a significant fraction of the pillars becomes saturated with water, resulting in increased dissipation.

- In a systematic study of the strengths of the amorphous, flaw-free pillars at various packing fractions and controlled levels of RH, we found a strong relationship between the strength and stiffness of the pillars, independent of RH. This scaling of strength and stiffness is understood by considering the energetics of an ellipsoidal inclusion in an elastic solid, which models a shear transformation. The robustness of the correlation between σ_{max} and E_{load} for a wide range of structural configurations brought about by mechanical annealing suggests that incipient operation of STs and macroscopic plastic flow along shear planes occur nearly simultaneously. The sharpness of the transition can be inferred as a signature of a system driven in the athermal limit with a relatively narrow distribution of barrier energies defining the fundamental unit of plastic deformation.

- Load drop statistics collected for the compressed pillars are compared to the mean field predictions of a discrete lattice model for plasticity. For $\phi > 0.572$,

we found that the stress drop statistics generally follow the predicted power-law scaling of the model. However, at the lowest packing fraction of $\phi = 0.559$, the statistics deviate from those observed in the denser pillars, indicative of a transition to fluid-like behavior.

- In an attempt to understand the particle-scale dynamics accompanying the sharp yielding and subsequent shear banding in our pillars, we performed *in situ* 4D compression experiments. While we were unable to capture shear band nucleation in an experiment, we were able to observe the maturation of an already nucleated shear band. We found that the developing shear band is accompanied by structural evolution, including dilation and a reduction in particle coordination. Moreover, the extent of the spatial correlations in strain gradually decays as the shear band matures, indicative of a transition from solid-like to liquid-like response. These results quantitatively support the interpretation of shear banding as a driven, localized glass transition.

- We constructed a confined, triaxial compression apparatus suitable for acquiring large amounts of deformation data with significant plasticity. The trajectories from these experiments were used to apply a new structural predictor of plasticity termed "softness" to our colloidal system. The "softness" metric was then applied to the pillar where shear band maturation was observed. We examined whether the transition in behavior found in the maturing shear band was accompanied by a change in the density or connectivity of soft particles, but were unable to

find a significant change in either measure.

5.2. Shear Banding in the Context of Softness

In Sections 1.2.2 and 4.5, we discussed the application of machine learning methods in elucidating structure-property relationships of rearrangements in amorphous solids. We described confined compression experiments on a colloidal glass which are amenable to the collection of a large number of rearrangements, which can be used to construct the hyperplane that defines "softness".

Preliminary efforts to analyze the shear band in the context of softness – specifically, by attempting to identify a percolation threshold or change in the density of soft particles at the solid-like to liquid-like transition – were not successful. To successfully perform these proposed experiments, one must overcome the challenges associated with observing a shear band in the pillars; specifically, one must capture the incipient nucleation in the LSCM field-of-view and stabilizing operation so that untrackable large displacements are avoided. Moreover, the packing fraction of the colloidal glass is more easily altered in the confined setup than in the pillar geometry, which opens the possibility of studying a possible connection between softness and the colloidal glass transition.

5.3. Stress Heterogeneity

As discussed in Section 1.2.4, multiple processing methods can be used to tune the heterogeneity in atomic stresses in an MG, thereby altering its toughness and ductility. However, the underlying mechanism responsible for enhanced ductility remains unclear and axiomatic design principles remain elusive. In some cases, it appears stress heterogeneity actually induces hardening. Hardening is believed to be the result of the high-temperature relaxation mechanisms in MGs, which are apparently enhanced by increased triaxiality in the stress. In other cases, the stress heterogeneity may delay the coalescence of STs into a shear band. Because of the large gradients, the continuous driving stress necessary for avalanche behavior is suppressed and strain localization is delayed.

Colloidal systems have the potential to elucidate the coupling between stress heterogeneity and ductility. Recently, Lin et al. introduced a method for calculating the particle-scale stress in colloidal systems[223, 224]. The so-called SALSA method ("stress analysis from local structural anisotropy") uses the time-averaged radial distribution function and thermodynamic considerations to calculate the stress tensor at the particle-scale. Using the SALSA method, Lin et al. studied the stress fields generated by dislocations, grain boundaries, and vacancies in a colloidal crystal. Interestingly, their experimental findings show that linear elasticity alone is often not sufficient to predict the stress fields generated by these defects.

It would be interesting to apply the SALSA method to the colloidal pillars, where free surfaces are present. Several modifications to the experimental procedures outlined in this dissertation would need to be made to use SALSA. Because thermal fluctuations underpin the SALSA method, it would be beneficial to increase thermal effects in our system. The simplest way to achieve this increase would be to use smaller particles. The dynamic timescale of a colloidal particle is the time τ_r it takes for the particle to diffuse a distance equal to its radius r, which scales as $\tau_r \propto r^3$ [154]. Reducing the particle size from $3.3\mu m$ to $1\mu m$ would result in an order-of-magnitude reduction in timescale and the system will explore more states in the same amount of laboratory time.

Studying the influence of surface roughness on the stress state near the surface is one potential application of the SALSA technique. In a method similar to that outlined in Section 2.1.1, the roughness of the pillars can be altered by varying the size of the silica particles used to line the inner walls of the capillaries. The measurements collected in these experiments may be able to address questions such as the relationship between surface roughness and stress intensity and the scaling of the decay in stress from the surface notches. A major drawback to the compression experiments is the difficulty in capturing the shear banding event. In this sense, studying a static pillar is less challenging experimentally. In addition to surface roughness, it would also be interesting to consider the impact of packing fraction on the stress heterogeneity.

The confined, triaxial compression setup described previously is also amenable

to studying this problem, especially if force transducers are incorporated into the compression cell. In such a compression cell, there is the potential to change both the stress triaxiality and the timescale of the particles. The triaxiality could be adjusted by controlling the confining stress, and the timescale could be adjusted by either varying the applied strain rate or changing the size of the particles. The ability to adjust these parameters independently may yield interesting insight into the problem. For example, does the characteristic eigenstrain, in terms of the shear and dilatational component, differ as the triaxiality is adjusted? If this is the case, then the elastic response in the matrix would be affected, potentially altering strain localization. Recent indentation experiments on MGs found a bimodal distribution of the nucleation events leading to strain localization, which was attributed to two distinct types of events with one being more diffusive in nature.

5.4. Application to Printing

The colloidal pillars described in this dissertation have been presented as a model system for studying plasticity in atomic solids. Of course, colloids also have wide-ranging industrial and technological uses. In many of these applications, colloids are used as the building blocks for larger-scale assemblies[225, 226]. Some examples include micro-electromechanical machines[227, 228], structural composites[229], sensors[230, 231], and photonics[232]. Because the structure of the colloidal assembly often dictates its properties, and therefore device performance, precise control of the assembly process is

desirable.

In self-assembly, particles assemble into a thermodynamically-stable state[233–235]. The nature of the stable state can be modified by altering the range and directionality of inter-particle interactions, the shape of the colloids, etc. As the particles perform Brownian motion, the system explores the energy landscape, gradually moving to lower energy states and eventually reaching thermodynamic equilibrium. Because the timescale for self-assembly is set by diffusion, the process can be quite slow.

Directed assembly is a potentially higher-throughput and more precise method of forming colloidal materials. Here, an external driving force is used to guide particles into the desired geometry and the resulting structures can have high-aspect ratios and sharp features not attainable with self-assembly. Direct write printing is a versatile directed assembly technique in which a colloidal ink is extruded from a robotically controlled nozzle[236, 237]. The extruded suspension can be solidified either by evaporation of the solvent or by a temperature-induced phase change, leaving a solid packing of colloidal material.

Recently, acoustic focusing has been coupled with standard direct write printing techniques in an effort to achieve even greater control over the printing process[238, 239]. In this method, piezoelectric actuators are used to generate a standing pressure wave in the microfluidic channel used in the printing process. These standing waves can be used to both align and trap colloidal particles. A precise understanding of the trapping

parameters and surface functionalization on the resulting agglomerate structure has yet to be developed.

Confocal microscopy has the potential to add insight to several steps in this printing process (see Figure 5.1 for an example). If the trapping process itself can be imaged in real time, for example, the impact of trapping parameters – particle size, shape, surface chemistry, etc – on the agglomerate structure can be explored. One outstanding question concerns the condition at which agglomerates break free of the trapping forces. What is there about the geometry of the structure, the resulting hydrodynamics forces, etc., that causes the particle to exit the trapping zone?

Confocal microscopy also has the potential to be applied to the printed structure. During the drying process, the hydrodynamic forces induced by the receding liquid meniscus may impart significant forces. How much do these forces alter the structure from its state in the trapping zone? How does the structure evolve with the drying front? Understanding how all of these parameters impact the printed structure will allow for the optimization of the printed structure so that it is as tough and robust as possible.
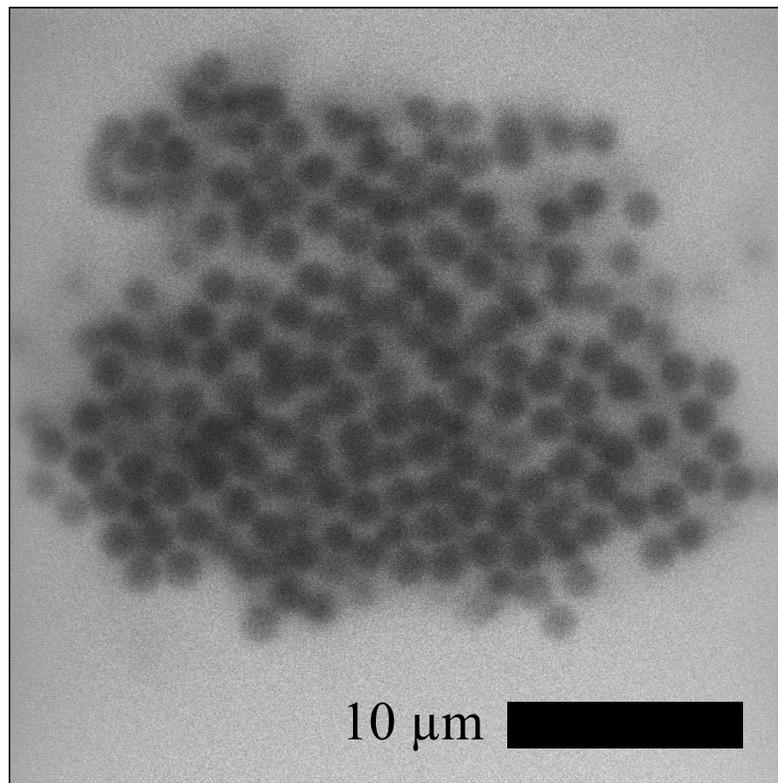
Figure 5.1: An assembly of 1.56 μm silica particles (Spherotech, functionalized with streptavidin) generated via acoustic focusing. The assembly is suspended in a mixture of 75% glycerol and 25% water with fluorescence, which results in dark particles on a bright background when illuminated with the confocal microscope's 488 nm laser. Image courtesy of Drew Melchert, UCSB.

Appendix A

Gibbs Free Energy of an Inclusion

in an Elastic Matrix

A.1. Gibbs Free Energy of an Inclusion in an Elastic Matrix

For completeness, we reproduce the derivation by T. Mura[193] of the change in the Gibbs Free Energy, G, of an inclusion in an elastic matrix with an applied traction. Define:

$$\epsilon_{ij} = \frac{1}{2}\left(\frac{\partial u_i}{\partial x_j} + \frac{\partial u_j}{\partial x_i}\right) \equiv \text{total strain}$$

$$\epsilon_{ij}^* \equiv \text{eigenstrain or transformation strain}$$

$$e_{ij} \equiv \text{elastic strain}$$

$$\sigma_{ij} = C_{ijkl}e_{kl} \equiv \text{stress}$$

The elastic strain energy of a body subjected to an applied traction σ_{ij}^∞ and an internal stress due to inclusion σ_{ij} is given by:

$$W^* = \frac{1}{2}\int_V \left(\sigma_{ij}^\infty + \sigma_{ij}\right)\left(\epsilon_{ij}^\infty + \epsilon_{ij} - \epsilon_{ij}^*\right) dV \text{ with } \sigma_{ij}^\infty = C_{ijkl}e_{kl}^\infty \qquad (A.1)$$

Equilibrium ensures that $\sigma_{ij,j} = 0$ and $\sigma_{ij}n_j = 0$ at the surface. Integration by parts gives:

$$\int_V \sigma_{ij}^\infty\left(\epsilon_{ij}^\infty + \epsilon_{ij}\right) dV = \int_V \sigma_{ij}^\infty\left(u_{i,j}^\infty + u_{i,j}\right) dV$$

$$= \sigma_{ij}\left(u_{i,j}^\infty + u_{i,j}\right)\big|_{V=S} - \int_V \sigma_{ij,j}\left(u_{i,j}^\infty + u_{i,j}\right) dV = 0 \quad (A.2)$$

Similarly $\sigma_{ij}^\infty = 0$. Since $\epsilon_{ij}^\infty = e_{ij}^\infty$ and $e_{ij} = \epsilon_{ij} - \epsilon_{ij}^*$ and using the symmetry

$C_{ijkl} = C_{klij}$:

$$\int_V \sigma_{ij}^\infty \left(\epsilon_{ij} - \epsilon_{ij}^*\right) dV = \int_V C_{ijkl} u_{k,l}^\infty \left(u_{i,j} - \epsilon_{ij}^*\right) dV = \int_V u_{k,l}^\infty C_{klij} e_{ij} dV =$$

$$\int_V u_{k,l}^\infty \sigma_{kl} dV = u_{kl}^\infty \sigma_{kl}|_{V=S} - \int_V u_{k,l}^\infty \sigma_{kl,l} dV = 0 \quad (A.3)$$

So:

$$W^* = -\frac{1}{2} \int_V \sigma_{ij} \epsilon_{ij}^* dV + \frac{1}{2} \int_V \sigma_{ij}^\infty \epsilon_{ij}^\infty dV \quad (A.4)$$

The total potential energy is given by:

$$G = W^* - \int_S F_i^\infty \left(u_i + u_i^\infty\right) dS \quad (A.5)$$

Where the second term is the work done at the boundary by the applied traction and $F_i^\infty = \sigma_{ij}^\infty nj$. Without any inclusions ($\epsilon_{ij}^* = 0$), $G = G_o$:

$$G_o = \frac{1}{2} \int_V \sigma_{ij}^\infty \epsilon_{ij}^\infty dV - \int_S F_i^\infty u_{ij} dS \quad (A.6)$$

Without any applied tractions ($\sigma_{ij} = 0$), $G = G_1$:

$$G_1 = -\frac{1}{2} \int_V \sigma_{ij}^\infty \epsilon_{ij}^* dV \quad (A.7)$$

The interaction between the strain field generated by the inclusions and the applied traction is:

$$\Delta G = G - G_o - G_1 = -\int_S \sigma_{ij}^\infty u_i n_j dS = -\int_V \sigma_{ij}^\infty u_{i,j} dV$$

$$= -\int_V \sigma_{ij}^\infty (u_{i,j} - \epsilon_{ij}^*) dV - \int_V \sigma_{ij}^\infty \epsilon_{ij}^* = -\int_V \sigma_{ij}^\infty \epsilon_{ij}^* \quad (A.8)$$

by Gausss theorem and the fact that $\int_V \sigma_{ij}^\infty (u_{i,j} - \epsilon_{ij}^*) dV = 0$ (see above). Therefore, with spatially homogeneous stress and strain fields:

$$\Delta G = -\int_V \sigma_{ij}^\infty \epsilon_{ij}^* dV = -\sigma_{ij}^\infty \epsilon_{ij}^* \quad (A.9)$$

For the case where the body is under an applied traction and inclusions are introduced, the change in free energy is given by:

$$\Delta \overline{G} = G - G_o = \Delta G + G_1 = -\frac{1}{2}\sigma_{ij} \epsilon_{ij}^* - \sigma_{ij}^\infty \epsilon_{ij}^* \quad (A.10)$$

Which is Equation 1 in the manuscript.

A.2. Derivation of the Stress Field for a Prescribed Transformation Strain

The tensorial infinitesimal strain, ϵ_{ij}, is given by:

$$\epsilon_{ij} = \frac{1}{2}\left(\frac{\partial u_i}{\partial x_j} + \frac{\partial u_j}{\partial x_i}\right) = \begin{bmatrix} \epsilon_{11} & \epsilon_{12} & \epsilon_{13} \\ \epsilon_{12} & \epsilon_{22} & \epsilon_{23} \\ \epsilon_{13} & \epsilon_{23} & \epsilon_{33} \end{bmatrix} = \begin{bmatrix} \epsilon_{11} & \frac{\gamma_{12}}{2} & \frac{\gamma_{13}}{2} \\ \frac{\gamma_{12}}{2} & \epsilon_{22} & \frac{\gamma_{23}}{2} \\ \frac{\gamma_{13}}{2} & \frac{\gamma_{23}}{2} & \epsilon_{33} \end{bmatrix} \tag{A.11}$$

Define the stiffness tensor, C_{ijkl}, for an isotropic homogeneous solid as:

$$C_{ijkl} = \frac{E\nu}{(1+\nu)(1-2\nu)}\delta_{ij}\delta_{kl} + \frac{E}{2(1+\nu)}(\delta_{ik}\delta_{jl} + \delta_{il}\delta_{jk}) \tag{A.12}$$

and the constitutive relation:

$$\sigma_{ij} = C_{ijkl}\epsilon_{kl} \tag{A.13}$$

where ϵ_{kl} is now the elastic component of the strain. Argon and Shi[196] use Eshelby's tensor for a spherical inclusion, given by:

$$S_{ijkl} = \frac{5\nu - 1}{15(1-\nu)}\delta_{ij}\delta_{kl} + \frac{4-5\nu}{15(1-\nu)}(\delta_{ik}\delta_{jl} + \delta_{il}\delta_{jk}) \tag{A.14}$$

To relate the confined strain, ϵ_{ij}^C, to the transformation strain, ϵ_{ij}^T, of the inclusion:

$$\epsilon_{ij}^C = S_{ijkl}\epsilon_{kl}^T \tag{A.15}$$

The authors assume two components of ϵ_{ij}^T:

$$\epsilon_{ij}^T = \frac{\epsilon_0^T}{3}\begin{bmatrix} 1 & 0 & 0 \\ 0 & 1 & 0 \\ 0 & 0 & 1 \end{bmatrix} + \frac{\gamma_0^T}{2}\begin{bmatrix} 0 & 1 & 0 \\ 1 & 0 & 0 \\ 0 & 0 & 0 \end{bmatrix} \tag{A.16}$$

Where the first term accounts for dilatation and the second a pure shear. The stress inside the inclusion, σ_{ij}^I, is given by:

$$\sigma_{ij}^I = C_{ijkl}\left(S_{klmn}\epsilon_{mn}^T - \epsilon_{kl}^T\right) \tag{A.17}$$

The elastic energy in both the inclusion and matrix is given:

$$E_{elastic} = -\frac{1}{2}\int_{\Omega_f} \sigma_{ij}^I \epsilon_{ij}^T dV \tag{A.18}$$

For the case of a spherical inclusion, in which σ_{ij}^I and ϵ_{ij}^T are constants, this expression becomes:

$$E_{elastic} = -\frac{1}{2}\sigma_{ij}^I \epsilon_{ij}^T \Omega_f \tag{A.19}$$

Considering only the dilatational component of ϵ_{kl}^T and using the relationship $E = 2\mu(1 + \nu)$:

$$\sigma_{ij}^I = \frac{2E\epsilon_0^T}{9(\nu - 1)}\begin{bmatrix} 1 & 0 & 0 \\ 0 & 1 & 0 \\ 0 & 0 & 1 \end{bmatrix} \text{ and } E_{elastic} = \frac{E}{9(\nu - 1)}(\epsilon_0^T)^2$$

$$= \frac{2\mu(1 + \nu)}{9(\nu - 1)}(\epsilon_0^T)^2 \tag{A.20}$$

Which is the same as the second term of Equation 7 in [196]. Now, considering only the shear component of ϵ_{kl}^T yields:

$$\sigma_{ij}^I = \frac{E\gamma_0^T(7 - 5\nu)}{30(\nu^2 - 1)}\begin{bmatrix} 0 & 1 & 0 \\ 1 & 0 & 0 \\ 0 & 0 & 0 \end{bmatrix} \tag{A.21}$$

and

$$E_{elastic} = \frac{E(7 - 5\nu)}{60(\nu^2 - 1)}(\gamma_0)^2 = \frac{\mu(7 - 5\nu)}{30(\nu^2 - 1)}(\epsilon_0)^2 \tag{A.22}$$

Which is the same as the first term of Equation 7 in [196]. In the presence of an applied far-field stress, the change in Gibbs free energy becomes (see previous section):

$$\Delta G = -\frac{1}{2}\sigma_{ij}^I \epsilon_{ij}^T \Omega_f - \sigma_{ij}^\infty \epsilon_{ij} \Omega_f \tag{A.23}$$

For uniaxial compression and our assumed orientation of the inclusion, the applied stress is:

$$\sigma_{ij} = \frac{\sigma}{2}\begin{bmatrix} -1 & 1 & 0 \\ 1 & -1 & 0 \\ 0 & 0 & 0 \end{bmatrix} \tag{A.24}$$

So the change in free energy is:

$$\Delta G = \frac{E}{\nu^2 - 1}\left[\frac{\nu + 1}{9}(\epsilon_o^T)^2 + \frac{7 - 5\nu}{60}(\gamma_o^T)^2\right] - \frac{\sigma(2\epsilon_o^T - 3\gamma_o^T)}{6} \tag{A.25}$$

Argon and Shi define the transformation dilatancy as:

$$\beta = \frac{\epsilon_o^c}{\gamma_o^c} = \frac{45(1-\nu)^2 \epsilon_o^T}{2(1+\nu)(4-5\nu)\gamma_o^T} \tag{A.26}$$

From measurements on an amorphous bubble raft, the authors estimate $\beta \approx 1$[196]. So:

$$\epsilon_o^T = \gamma_o^T \frac{2(1+\nu)(4-5\nu)}{45(1-\nu)^2} \tag{A.27}$$

With this relationship:

$$\Delta G = \frac{\Omega E}{\nu^2 - 1} \left[\frac{\nu+1}{9} \left(\frac{2(1+\nu)(4-5\nu)}{45(1-\nu)^2} \gamma_o^T \right)^2 + \frac{7-5\nu}{60} (\gamma_o^T)^2 \right]$$
$$+ \frac{\Omega\sigma\gamma_o^T}{2} - \frac{\Omega\sigma\gamma_o^T}{3} \frac{2(1+\nu)(4-5\nu)}{45(1-\nu)^2} \tag{A.28}$$

Setting $\Delta G = 0$ and rearranging yields:

$$\frac{\sigma}{E} = \gamma_o^T \frac{5,675\nu^5 - 33,365\nu^4 + 70,934\nu^3 - 74,578\nu^2 + 39,967\nu - 8,761}{270(\nu-1)^3(55\nu^3 - 111\nu^2 - 147\nu + 119)}$$
$$^T\Theta(/nu) \tag{A.29}$$

Appendix B

Determination of the 3D Radial Distribution Function with Imaging Boundaries

B.1. Determination of the 3D Radial Distribution Function with Imaging Boundaries

It is important to properly account for experimental boundaries when calculating $g\left(\mathbf{r}\right)$ using real-space positions of particles. The radial distribution function is defined as:

$$g\left(\mathbf{r}\right) = \frac{1}{\eta}\frac{dN\left(\mathbf{r}\right)}{d\mathbf{r}} \tag{B.1}$$

where $\eta = \frac{N}{V}$ is the particle number density and $\frac{dN(\mathbf{r})}{d\mathbf{r}}$ is the number of particles in the volume element at position $\mathbf{r}$. This function can be interpreted as the probability of finding a particle in the volume element $d\mathbf{r}$ at position $\mathbf{r}$, given that there is a particle at the origin, normalized by the probability of finding a particle in the volume, which is η.

Experimental boundaries can complicate determination of $g\left(\mathbf{r}\right)$ because certain vectors $\mathbf{r}$ are sampled more frequently than others. Consider a 3-dimensional rectangular box containing N particles with imaging bounds given by $l_{x,min}$, $l_{x,max}$, $l_{y,min}$, $l_{y,max}$, $l_{z,min}$, and $l_{z,max}$. For particles located near the boundaries of the box, only a fraction of their neighboring particles are located within the bounds of the imaging volume. Obviously, missing neighbors are a result of the boundaries and not a feature of the actual structure. Failure to properly account for the "missing volume" can lead to artificially low values of $g\left(\mathbf{r}\right)$ at values of $r = \|\mathbf{r}\|$ approaching half the box size and incorrect asymmetries for imaging boxes without equal edge lengths.

One computational algorithm that accounts for boundaries is described as follows:

1. Construct a 3-dimensional array $\mathbf{X} = \left[-x_l : dx : x_l; -y_l : dy : y_l; -z_l : dz : z_l\right]$ of distances $\mathbf{r}$ that sets the extent of $g\left(\mathbf{r}\right)$ to be calculated

2. Consider one particle i with position $[x_i, y_i, z_i]$ and determine the vectors $\mathbf{r}_{ij}$ from the particle to its neighbors within cutoff distance $r_{max} = \sqrt{x_l^2 + y_l^2 + z_l^2}$

3. Using $\mathbf{X}$, construct a 3-dimensional histogram of particle i's neighbor locations $\mathbf{N}_i$ by binning the x_{ij}, y_{ij}, and z_{ij} components of the $\mathbf{r}_{ij}$ vectors

4. Now consider the extent of:

$$X_i = [-x_l + x_i : dx : x_l + x_i; -y_l + y_i : dy : y_l + y_i; -z_l + z_i : dz : z_l + z_i]$$

contained within the imaging volume. Create a 3-dimensional array $\mathbf{T}_i$ of the same size as $\mathbf{X}_i$ with all entries set to 1. Now set all $\mathbf{T}_i(\mathbf{X}_i < l_{x,min}) = 0$, $\mathbf{N}_i(\mathbf{X}_i > l_{x,max}) = 0$, etc. $\mathbf{T}_i(\mathbf{X}_i)$ can be considered the number of attempts of finding a particle at $\mathbf{X}$ for particle i.

5. Repeat steps 2-4 for all N particles in the imaging volume and compute $\mathbf{N} = \sum_{i=1}^{N} \mathbf{N}_i$ and $\mathbf{T} = \sum_{i=1}^{T} \mathbf{T}_i$

6. Now the probability $\mathbf{P} = \mathbf{N} \oslash \mathbf{T}$ of finding a particle at position $\mathbf{X}$ may be computed, where $\oslash$ denotes the element-wise quotient.

7. $\mathbf{P}$ can now be normalized by η to give the pair-correlation function $g(\mathbf{r})$ discretized on the grid $\mathbf{X}$

Bibliography

[1] Richard Zallen. *The Physics of Amorphous Solids*. John Wiley & Sons, 2008.

[2] L-Q Xing, Y Li, KT Ramesh, J Li, and TC Hufnagel. Enhanced plastic strain in zr-based bulk amorphous alloys. *Physical Review B*, 64(18):180201, 2001.

[3] Lei Zhang, Gang Feng, Zorana Zeravcic, Teresa Brugarolas, Andrea J. Liu, and Daeyeon Lee. Using shape anisotropy to toughen disordered nanoparticle assemblies. *ACS Nano*, 7:8043–8050, 2013.

[4] Younjin Min, Mustafa Akbulut, Kai Kristiansen, Yuval Golan, and Jacob Israelachvili. The role of interparticle and external forces in nanoparticle assembly. *Nature Materials*, 7(7):527–538, 2008.

[5] Takayuki Narumi, Scott V Franklin, Kenneth W Desmond, Michio Tokuyama, and Eric R Weeks. Spatial and temporal dynamical heterogeneities approaching the binary colloidal glass transition. *Soft Matter*, 7(4):1472–1482, 2011.

[6] CA Schuh and TG Nieh. A nanoindentation study of serrated flow in bulk metallic glasses. *Acta Materialia*, 51(1):87–99, 2003.

[7] Ethan Pratt and Michael Dennin. Nonlinear stress and fluctuation dynamics of sheared disordered wet foam. *Physical Review E*, 67(5):051402, 2003.

[8] Brian Miller, Corey O'Hern, and RP Behringer. Stress fluctuations for continuously sheared granular materials. *Physical Review Letters*, 77(15):3110, 1996.

[9] Toshiji Mukai, TG Nieh, Yoshihito Kawamura, Akihisa Inoue, and Kenji Higashi. Effect of strain rate on compressive behavior of a pd 40 ni 40 p 20 bulk metallic glass. *Intermetallics*, 10(11):1071–1077, 2002.

[10] Vladimir Kobelev and Kenneth S Schweizer. Strain softening, yielding, and shear thinning in glassy colloidal suspensions. *Physical Review E*, 71(2):021401, 2005.

[11] A Dubach, R Raghavan, JF Löffler, J Michler, and U Ramamurty. Micropillar compression studies on a bulk metallic glass in different structural states. *Scripta Materialia*, 60(7):567–570, 2009.

[12] Daniel J Strickland, Lei Zhang, Yun-Ru Huang, Daniel J Magagnosc, Daeyeon Lee, and Daniel S Gianola. Synthesis and mechanical response of disordered colloidal micropillars. *Physical Chemistry Chemical Physics*, 16(22):10274–10285, 2014.

[13] P Bésuelle, J Desrues, and S Raynaud. Experimental characterisation of the localisation phenomenon inside a Vosges sandstone in a triaxial cell. *International Journal of Rock Mechanics and Mining Sciences*, 37(8):1223–1237, December 2000.

[14] Donald E Sands. *Introduction to crystallography.* Courier Corporation, 1969.

[15] KF Kelton. Crystal nucleation in liquids and glasses. *Solid State Physics*, 45.

[16] Robert W Balluffi, Sam Allen, and W Craig Carter. *Kinetics of Materials.* John Wiley & Sons, 2005.

[17] Kurt Binder. Theory of first-order phase transitions. *Reports on Progress in Physics*, 50(7):783, 1987.

[18] Ml D Ediger, CA Angell, and Sidney R Nagel. Supercooled liquids and glasses. *The Journal of Physical Chemistry*, 100(31):13200–13212, 1996.

[19] Pablo G Debenedetti and Frank H Stillinger. Supercooled liquids and the glass transition. *Nature*, 410(6825):259–267, 2001.

[20] R Busch, E Bakke, and WL Johnson. Viscosity of the supercooled liquid and relaxation at the glass transition of the zr46. 75ti8. 25cu7. 5ni10be27. 5 bulk metallic glass forming alloy. *Acta Materialia*, 46(13):4725–4732, 1998.

[21] Frank H Stillinger and Pablo G Debenedetti. Glass transition thermodynamics and kinetics. *Annual Reviews of Condensed Matter Physics*, 4(1):263–285, 2013.

[22] C Austin Angell, Kia L Ngai, Greg B McKenna, Paul F McMillan, and Steve W Martin. Relaxation in glassforming liquids and amorphous solids. *Journal of Applied Physics*, 88(6):3113–3157, 2000.

[23] Giulio Biroli and Juan P Garrahan. Perspective: The glass transition. *The Journal of Chemical Physics*, 138(12):12A301, 2013.

[24] Vassiliy Lubchenko and Peter G Wolynes. Theory of structural glasses and supercooled liquids. *Annual Review of Physical Chemistry*, 58:235–266, 2007.

[25] David Chandler and Juan P Garrahan. Dynamics on the way to forming glass: Bubbles in space-time. *Annual Review of Physical Chemistry*, 61:191–217, 2010.

[26] Sadanand Singh, MD Ediger, and Juan J De Pablo. Ultrastable glasses from in silico vapour deposition. *Nature Materials*, 12(2):139–144, 2013.

[27] Jan Schroers. Processing of bulk metallic glass. *Advanced Materials*, 22(14):1566–1597, 2010.

[28] Yonghao Sun, Amadeu Concustell, and A Lindsay Greer. Thermomechanical processing of metallic glasses: extending the range of the glassy state. *Nature Reviews Materials*, 1:16039, 2016.

[29] Y. Rahmani, K. van der Vaart, B. van Dam, Z. Hu, V. Chikkadi, and P. Schall. Dynamic heterogeneity in hard and soft sphere colloidal glasses. *Soft Matter*, 8:4264–4270, 2012.

[30] Eric R Weeks, John C Crocker, Andrew C Levitt, Andrew Schofield, and David A Weitz. Three-dimensional direct imaging of structural relaxation near the colloidal glass transition. *Science*, 287(5453):627–631, 2000.

[31] D Weaire and S Hutzler. *The Physics of Foams: Oxford University Press*. New York, 1999.

[32] DJ Durian. Foam mechanics at the bubble scale. *Physical Review Letters*, 75(26):4780, 1995.

[33] AD Gopal and DJ Durian. Shear-induced melting of an aqueous foam. *Journal of Colloid and Interface Science*, 213(1):169–178, 1999.

[34] Andrea J Liu and Sidney R Nagel. Nonlinear dynamics: Jamming is not just cool any more. *Nature*, 396(6706):21–22, 1998.

[35] Andrea J Liu, Sidney R Nagel, Wim Van Saarloos, and Matthieu Wyart. The jamming scenario-an introduction and outlook. *arXiv preprint arXiv:1006.2365*, 2010.

[36] R.K. Pathria and Paul D. Beale. *Statistical Mechanics (Third Edition)*. Academic Press, 2011.

[37] Anthony J Leggett. Amorphous materials at low temperatures: why are they so similar? *Physica B: Condensed Matter*, 169(1):322–327, 1991.

[38] VK Malinovsky and AP Sokolov. The nature of boson peak in raman scattering in glasses. *Solid State Communications*, 57(9):757–761, 1986.

[39] Ke Chen, Wouter Ellenbroek, Zexin Zhang, Daniel Chen, Peter Yunker, Silke Henkes, Carolina Brito, Olivier Dauchot, Wim van Saarloos, Andrea Liu, and A. Yodh. Low-frequency vibrations of soft colloidal glasses. *Physical Review Letters*, 105:025501, Jul 2010.

[40] Antina Ghosh, Romain Mari, Vijayakumar Chikkadi, Peter Schall, Jorge Kurchan, and Daniel Bonn. Density of states of colloidal glasses and supercooled liquids. *Soft Matter*, 6:3082–3090, 2010.

[41] Ning Xu, Matthieu Wyart, Andrea Liu, and Sidney Nagel. Excess vibrational modes and the boson peak in model glasses. *Physical Review Letters*, 98:175502, Apr 2007.

[42] SR Elliott. A unified model for the low-energy vibrational behaviour of amorphous solids. *EPL (Europhysics Letters)*, 19(3):201, 1992.

[43] Mi D Ediger. Spatially heterogeneous dynamics in supercooled liquids. *Annual Review of Physical Chemistry*, 51(1):99–128, 2000.

[44] Ludovic Berthier. Trend: Dynamic heterogeneity in amorphous materials. *Physics*, 4:42, 2011.

[45] Ludovic Berthier, Giulio Biroli, Jean-Philippe Bouchaud, Luca Cipelletti, and Wim van Saarloos. *Dynamical Heterogeneities in Glasses, Colloids, and Granular Media*. Oxford University Press, 2011.

[46] Jean-Pierre Hansen and IR McDonald. *Theory of Simple Liquids*. Academic Press, 2006.

[47] Paul Hopkins, Andrea Fortini, Andrew J Archer, and Matthias Schmidt. The van hove distribution function for brownian hard spheres: Dynamical test particle theory and computer simulations for bulk dynamics. *The Journal of Chemical Physics*, 133(22):224505, 2010.

[48] Olivier Dauchot, Guillaume Marty, and Giulio Biroli. Dynamical heterogeneity close to the jamming transition in a sheared granular material. *Physical Review Letters*, 95(26):265701, 2005.

[49] Karin A Dahmen, Yehuda Ben-Zion, and Jonathan T Uhl. A simple analytic theory for the statistics of avalanches in sheared granular materials. *Nature Physics*, 7(7):554–557, 2011.

[50] James Antonaglia, Wendelin J. Wright, Xiaojun Gu, Rachel R. Byer, Todd C. Hufnagel, Michael LeBlanc, Jonathan T. Uhl, and Karin A. Dahmen. Bulk metallic glasses deform via slip avalanches. *Physical Review Letters*, 112:155501, Apr 2014.

[51] Alberto Petri, Andrea Baldassarri, Fergal Dalton, Giorgio Pontuale, Luciano Pietronero, and Stefano Zapperi. Stochastic dynamics of a sheared granular medium. *The European Physical Journal B-Condensed Matter and Complex Systems*, 64(3):531–535, 2008.

[52] Pengfei Guan, Mingwei Chen, and Takeshi Egami. Stress-temperature scaling for steady-state flow in metallic glasses. *Physical Review Letters*, 104(20):205701, 2010.

[53] Takeshi Egami. Mechanical failure and glass transition in metallic glasses. *Journal of Alloys and Compounds*, 509:S82–S86, 2011.

[54] Peter Olsson and Stephen Teitel. Critical scaling of shear viscosity at the jamming transition. *Physical Review Letters*, 99(17):178001, 2007.

[55] Anindita Basu, Ye Xu, Tim Still, P. E. Arratia, Zexin Zhang, K. N. Nordstrom, Jennifer M. Rieser, J. P. Gollub, D. J. Durian, and A. G. Yodh. Rheology of soft colloids across the onset of rigidity: scaling behavior{,} thermal{,} and non-thermal responses. *Soft Matter*, 10(17):3027–3035, 2014.

[56] J. Frenkel. Zur Theorie der Elastizittsgrenze und der Festigkeit kristallinischer Krper. *Zeitschrift fur Physik*, 37(7-8):572–609, July 1926.

[57] George Ellwood Dieter and David J Bacon. *Mechanical Metallurgy*, volume 3. McGraw-Hill New York, 1986.

[58] E O Hall. The Deformation and Ageing of Mild Steel: III Discussion of Results. *Proceedings of the Physical Society. Section B*, 64(9):747, 1951.

[59] N.J. Petch. The cleavage strength of polycrystals. *Journal of the Iron and Steel Institute*, 174:1953, 1953.

[60] G. I. Taylor. The Mechanism of Plastic Deformation of Crystals. Part I. Theoretical. *Proceedings of the Royal Society of London. Series A*, 145(855):362–387, 1934.

[61] To Egami, K Maeda, and V Vitek. Structural defects in amorphous solids a computer simulation study. *Philosophical Magazine A*, 41(6):883–901, 1980.

[62] W Klement, RH Willens, and POL Duwez. Non-crystalline structure in solidified gold–silicon alloys. *Nature*, 187(4740):869–870, 1960.

[63] Akihisa Inoue, Katsumasa Ohtera, Kazuhiko Kita, and Tsuyoshi Masumoto. New amorphous mg-ce-ni alloys with high strength and good ductility. *Japanese Journal of Applied Physics*, 27(12A):L2248, 1988.

[64] Atakan Peker and William L Johnson. A highly processable metallic glass: Zr41. 2ti13. 8cu12. 5ni10. 0be22. 5. *Applied Physics Letters*, 63(17):2342–2344, 1993.

[65] MF Ashby and AL Greer. Metallic glasses as structural materials. *Scripta Materialia*, 54(3):321–326, 2006.

[66] C Schuh, T Hufnagel, and U Ramamurty. Mechanical behavior of amorphous alloys. *Acta Materialia*, 55:4067–4109, 2007.

[67] W. L. Johnson and K. Samwer. A universal criterion for plastic yielding of metallic glasses with a (T/Tg)2/3 temperature dependence. *Physical Review Letters*, 95, 2005.

[68] Mingwei Chen. A brief overview of bulk metallic glasses. *NPG Asia Materials*, 3(9):82–90, 2011.

[69] Golden Kumar, Hong X Tang, and Jan Schroers. Nanomoulding with amorphous metals. *Nature*, 457(7231):868–872, 2009.

[70] A Lindsay Greer. Metallic glasses. *Science*, 267(5206):1947, 1995.

[71] Me F Ashby. A first report on deformation-mechanism maps. *Acta Metallurgica*, 20(7):887–897, 1972.

[72] Florian H Dalla Torre, Alban Dubach, Marco E Siegrist, and Jörg F Löffler. Negative strain rate sensitivity in bulk metallic glass and its similarities with the dynamic strain aging effect during deformation. *Applied Physics Letters*, 89(9):091918, 2006.

[73] WH Jiang, FX Liu, F Jiang, KQ Qiu, H Choo, and PK Liaw. Strain-rate dependence of hardening and softening in compression of a bulk-metallic glass. *Journal of Materials Research*, 22(10):2655–2658, 2007.

[74] Hugh A Bruck, Ares J Rosakis, and William L Johnson. The dynamic compressive behavior of beryllium bearing bulk metallic glasses. *Journal of Materials Research*, 11(02):503–511, 1996.

[75] Frans Spaepen. A microscopic mechanism for steady state inhomogeneous flow in metallic glasses. *Acta Metallurgica*, 25(4):407–415, 1977.

[76] DE Polk and D Turnbull. Flow of melt and glass forms of metallic alloys. *Acta Metallurgica*, 20(4):493–498, 1972.

[77] A.S. Argon. Plastic deformation in metallic glasses. *Acta Metallurgica*, 27(1):47–58, January 1979.

[78] M L Falk and J S Langer. Dynamics of viscoplastic deformation in amorphous solids. *Physical Review E*, 57(6):7192–7205, June 1998.

[79] Ratul Dasgupta, Oleg Gendelman, Pankaj Mishra, Itamar Procaccia, and Carmel A B Z Shor. Shear localization in three-dimensional amorphous solids. *Physical Review E*, 88(3):32401, September 2013.

[80] A.S. Argon and H.Y. Kuo. Plastic flow in a disordered bubble raft (an analog of a metallic glass). *Materials Science and Engineering*, 39(1):101–109, July 1979.

[81] Peter Schall, David A Weitz, and Frans Spaepen. Structural Rearrangements That Govern Flow in Colloidal Glasses. *Science*, 318(5858):1895–1899, December 2007.

[82] Christopher A Schuh, Alan C Lund, and TG Nieh. New regime of homogeneous flow in the deformation map of metallic glasses: elevated temperature nanoindentation experiments and mechanistic modeling. *Acta Materialia*, 52(20):5879–5891, 2004.

[83] CA Schuh, JK Mason, and AC Lund. Quantitative insight into dislocation nucleation from high-temperature nanoindentation experiments. *Nature Materials*, 4(8):617–621, 2005.

[84] MA Tschopp and DL McDowell. Grain boundary dislocation sources in nanocrystalline copper. *Scripta Materialia*, 58(4):299–302, 2008.

[85] Lisa Y Chen, Mo-rigen He, Jungho Shin, Gunther Richter, and Daniel S Gianola. Measuring surface dislocation nucleation in defect-scarce nanostructures. *Nature Materials*, 14(7):707–713, 2015.

[86] Hongbin Bei, YF Gao, S Shim, Easo P George, and George Mathews Pharr. Strength differences arising from homogeneous versus heterogeneous dislocation nucleation. *Physical Review B*, 77(6):060103, 2008.

[87] Julia R Greer, Warren C Oliver, and William D Nix. Size dependence of mechanical properties of gold at the micron scale in the absence of strain gradients. *Acta Materialia*, 53(6):1821–1830, 2005.

[88] Michael D Uchic, Paul A Shade, and Dennis M Dimiduk. Plasticity of micrometer-scale single crystals in compression. *Annual Review of Materials Research*, 39:361–386, 2009.

[89] Julia R Greer and Jeff Th M De Hosson. Plasticity in small-sized metallic systems: Intrinsic versus extrinsic size effect. *Progress in Materials Science*, 56(6):654–724, 2011.

[90] Pengyang Zhao, Ju Li, and Yunzhi Wang. Extended defects, ideal strength and actual strengths of finite-sized metallic glasses. *Acta Materialia*, 73:149–166, 2014.

[91] Asaph Widmer-Cooper, Peter Harrowell, and H Fynewever. How reproducible are dynamic heterogeneities in a supercooled liquid? *Physical Review Letters*, 93(13):135701, 2004.

[92] HW Sheng, WK Luo, FM Alamgir, JM Bai, and E Ma. Atomic packing and short-to-medium-range order in metallic glasses. *Nature*, 439(7075):419–425, 2006.

[93] YQ Cheng, HW Sheng, and E Ma. Relationship between structure, dynamics, and mechanical properties in metallic glass-forming alloys. *Physical Review B*, 78(1):014207, 2008.

[94] YQ Cheng and E Ma. Atomic-level structure and structure–property relationship in metallic glasses. *Progress in Materials Science*, 56(4):379–473, 2011.

[95] David Rodney, Anne Tanguy, and Damien Vandembroucq. Modeling the mechanics of amorphous solids at different length scale and time scale. *Modelling and Simulation in Materials Science and Engineering*, 19(8):083001, 2011.

[96] TR Kirkpatrick, D Thirumalai, and Peter G Wolynes. Scaling concepts for the dynamics of viscous liquids near an ideal glassy state. *Physical Review A*, 40(2):1045, 1989.

[97] Jun Ding, Yong-Qiang Cheng, Howard Sheng, Mark Asta, Robert O Ritchie, and Evan Ma. Universal structural parameter to quantitatively predict metallic glass properties. *Nature Communications*, 7, 2016.

[98] Georges Voronoï. Nouvelles applications des paramètres continus à la théorie des formes quadratiques. deuxième mémoire. recherches sur les parallélloèdres primitifs. *Journal für die reine und angewandte Mathematik*, 134:198–287, 1908.

[99] Masaharu Tanemura, Tohru Ogawa, and Naofumi Ogita. A new algorithm for three-dimensional voronoi tessellation. *Journal of Computational Physics*, 51(2):191–207, 1983.

[100] John D Bernal. A geometrical approach to the structure of liquids. *Nature*, 183(4655):141–147, 1959.

[101] D Srolovitz, K Maeda, V Vitek, and T Egami. Structural defects in amorphous solids Statistical analysis of a computer model. *Philosophical Magazine A*, 44(4):847–866, 1981.

[102] D Srolovitz, V Vitek, and T Egami. An atomistic study of deformation of amorphous metals. *Acta Metallurgica*, 31(2):335–352, 1983.

[103] Michel Tsamados, Anne Tanguy, Chay Goldenberg, and Jean-Louis Barrat. Local elasticity map and plasticity in a model lennard-jones glass. *Physical Review E*, 80(2):026112, 2009.

[104] Sylvain Patinet, Damien Vandembroucq, and Michael L Falk. Connecting local yield stresses with plastic activity in amorphous solids. *Physical Review Letters*, 117(4):045501, 2016.

[105] M Lisa Manning and Andrea J Liu. Vibrational modes identify soft spots in a sheared disordered packing. *Physical Review Letters*, 107(10):108302, 2011.

[106] Jörg Rottler, Samuel S Schoenholz, and Andrea J Liu. Predicting plasticity with soft vibrational modes: From dislocations to glasses. *Physical Review E*, 89(4):042304, 2014.

[107] Jun Ding, Sylvain Patinet, Michael L Falk, Yongqiang Cheng, and Evan Ma. Soft spots and their structural signature in a metallic glass. *Proceedings of the National Academy of Sciences*, 111(39):14052–14056, 2014.

[108] Ekin D Cubuk, Samuel S Schoenholz, Jennifer M Rieser, Brad D Malone, Joerg Rottler, Douglas J Durian, Efthimios Kaxiras, and Andrea J Liu. Identifying structural flow defects in disordered solids using machine-learning methods. *Physical Review Letters*, 114(10):108001, 2015.

[109] Ekin D Cubuk, Samuel S Schoenholz, Efthimios Kaxiras, and Andrea J Liu. Structural properties of defects in glassy liquids. *The Journal of Physical Chemistry B*, 120(26):6139–6146, 2016.

[110] Samuel S Schoenholz, Ekin D Cubuk, Efthimios Kaxiras, and Andrea J Liu. Relationship between local structure and relaxation in out-of-equilibrium glassy systems. *Proceedings of the National Academy of Sciences*, 114(2):263–267, 2017.

[111] CE Packard, LM Witmer, and CA Schuh. Hardening of a metallic glass during cyclic loading in the elastic range. *Applied Physics Letters*, 92(17):171911, 2008.

[112] Z Wang, P Wen, LS Huo, HY Bai, and WH Wang. Signature of viscous flow units in apparent elastic regime of metallic glasses. *Applied Physics Letters*, 101(12):121906, 2012.

[113] Todd C Hufnagel, Christopher A Schuh, and Michael L Falk. Deformation of metallic glasses: Recent developments in theory, simulations, and experiments. *Acta Materialia*, 109:375–393, 2016.

[114] Eric R. Homer. Examining the initial stages of shear localization in amorphous metals. *Acta Materialia*, 63:44–53, January 2014.

[115] Futoshi Shimizu, Shigenobu Ogata, and Ju Li. Yield point of metallic glass. *Acta Materialia*, 54(16):4293–4298, 2006.

[116] Futoshi Shimizu, Shigenobu Ogata, and Ju Li. Theory of shear banding in metallic glasses and molecular dynamics calculations. *Materials Transactions*, 48(11):2923–2927, 2007.

[117] AJ Cao, YQ Cheng, and E Ma. Structural processes that initiate shear localization in metallic glass. *Acta Materialia*, 57(17):5146–5155, 2009.

[118] Bing Yang, Mark L Morrison, Peter K Liaw, Raymond A Buchanan, Gongyao Wang, Chain T Liu, and Mitsunori Denda. Dynamic evolution of nanoscale shear bands in a bulk-metallic glass. *Applied Physics Letters*, 86(14):141904, 2005.

[119] JJ Lewandowski and AL Greer. Temperature rise at shear bands in metallic glasses. *Nature Materials*, 5(1):15–18, 2006.

[120] Stephanie K Slaughter, Felicitee Kertis, Erin Deda, Xiaojun Gu, Wendelin J Wright, and Todd C Hufnagel. Shear bands in metallic glasses are not necessarily hot. *APL Materials*, 2(9):096110, 2014.

[121] SX Song, X-L Wang, and TG Nieh. Capturing shear band propagation in a zr-based metallic glass using a high-speed camera. *Scripta Materialia*, 62(11):847–850, 2010.

[122] CE Packard and CA Schuh. Initiation of shear bands near a stress concentration in metallic glass. *Acta Materialia*, 55(16):5348–5358, 2007.

[123] Yunfeng Shi and Michael L Falk. Strain localization and percolation of stable structure in amorphous solids. *Physical Review Letters*, 95(9):095502, 2005.

[124] Yunfeng Shi, Michael B Katz, Hui Li, and Michael L Falk. Evaluation of the disorder temperature and free-volume formalisms via simulations of shear banding in amorphous solids. *Physical Review Letters*, 98(18):185505, 2007.

[125] J Ding, YQ Cheng, and E Ma. Correlating local structure with inhomogeneous elastic deformation in a metallic glass. *Applied Physics Letters*, 101(12):121917, 2012.

[126] Alain Reza Yavari, Alain Le Moulec, Akihisa Inoue, Nobuyuki Nishiyama, Nicoleta Lupu, Eiichiro Matsubara, Walter José Botta, Gavin Vaughan, Marco Di Michiel, and Åke Kvick. Excess free volume in metallic glasses measured by x-ray diffraction. *Acta Materialia*, 53(6):1611–1619, 2005.

[127] Wojciech Dmowski, Y Yokoyama, A Chuang, Y Ren, M Umemoto, K Tsuchiya, A Inoue, and T Egami. Structural rejuvenation in a bulk metallic glass induced by severe plastic deformation. *Acta Materialia*, 58(2):429–438, 2010.

[128] V Chikkadi, S Mandal, B Nienhuis, D Raabe, F Varnik, and P Schall. Shear-induced anisotropic decay of correlations in hard-sphere colloidal glasses. *Europhysics Letters*, 100(5):56001, 2012.

[129] Dmitry Denisov, MT Dang, Bernd Struth, Gerard Wegdam, and Peter Schall. Resolving structural modifications of colloidal glasses by combining x-ray scattering and rheology. *Scientific Reports*, 3, 2013.

[130] HB Yu, WH Wang, HY Bai, Yue Wu, and MW Chen. Relating activation of shear transformation zones to β relaxations in metallic glasses. *Physical Review B*, 81(22):220201, 2010.

[131] Wei Hua Wang. Correlation between relaxations and plastic deformation, and elastic model of flow in metallic glasses and glass-forming liquids. *Journal of Applied Physics*, 110(5):053521, 2011.

[132] Hai Bin Yu, Wei Hua Wang, Hai Yang Bai, and Konrad Samwer. The β-relaxation in metallic glasses. *National Science Review*, 1(3):429–461, 2014.

[133] YH Liu, Chain T Liu, WH Wang, A Inoue, T Sakurai, and MW Chen. Thermodynamic origins of shear band formation and the universal scaling law of metallic glass strength. *Physical Review Letters*, 103(6):065504, 2009.

[134] DJ Magagnosc, G Kumar, J Schroers, P Felfer, JM Cairney, and DS Gianola. Effect of ion irradiation on tensile ductility, strength and fictive temperature in metallic glass nanowires. *Acta Materialia*, 74:165–182, 2014.

[135] V Chikkadi, DM Miedema, MT Dang, B Nienhuis, and P Schall. Shear banding of colloidal glasses: Observation of a dynamic first-order transition. *Physical Review Letters*, 113(20):208301, 2014.

[136] Prabhat K. Jaiswal, Itamar Procaccia, Corrado Rainone, and Murari Singh. Mechanical yield in amorphous solids: A first-order phase transition. *Physical Review Letters*, 116:085501, Feb 2016.

[137] Brittany A Isner and Daniel J Lacks. Generic rugged landscapes under strain and the possibility of rejuvenation in glasses. *Physical Review Letters*, 96(2):025506, 2006.

[138] Akira Furukawa, Kang Kim, Shinji Saito, and Hajime Tanaka. Anisotropic cooperative structural rearrangements in sheared supercooled liquids. *Physical Review Letters*, 102(1):016001, 2009.

[139] Ali Argon. *Strengthening mechanisms in crystal plasticity*. Number 4. Oxford University Press on Demand, 2008.

[140] JJ Lewandowski*, WH Wang, and AL Greer. Intrinsic plasticity or brittleness of metallic glasses. *Philosophical Magazine Letters*, 85(2):77–87, 2005.

[141] J.J. Lewandowski, M. Shazly, and A. Shamimi Nouri. Intrinsic and extrinsic toughening of metallic glasses. *Scripta Materialia*, 54(3):337 – 341, 2006. Viewpoint set no: 37. On mechanical behavior of metallic glasses Viewpoint set no: 37. On mechanical behavior of metallic glasses.

[142] Golden Kumar, Pascal Neibecker, Yan Hui Liu, and Jan Schroers. Critical fictive temperature for plasticity in metallic glasses. *Nature Communications*, 4:1536, 2013.

[143] ZT Wang, J Pan, Y Li, and CA Schuh. Densification and strain hardening of a metallic glass under tension at room temperature. *Physical Review Letters*, 111(13):135504, 2013.

[144] SV Ketov, YH Sun, S Nachum, Z Lu, A Checchi, AR Beraldin, HY Bai, WH Wang, DV Louzguine-Luzgin, MA Carpenter, et al. Rejuvenation of metallic glasses by non-affine thermal strain. *Nature*, 524(7564):200–203, 2015.

[145] Sara Adibi, Paulo S Branicio, Rachel Liontas, David Z Chen, Julia R Greer, David J Srolovitz, and Shailendra P Joshi. Surface roughness imparts tensile ductility to nanoscale metallic glasses. *Extreme Mechanics Letters*, 5:88–95, 2015.

[146] DJ Magagnosc, R Ehrbar, G Kumar, MR He, J eoers, and DS Gianola. Tunable tensile ductility in metallic glasses. *Scientific Reports*, 3, 2013.

[147] QP Cao, JW Liu, KJ Yang, F Xu, ZQ Yao, A Minkow, HJ Fecht, J Ivanisenko, LY Chen, XD Wang, et al. Effect of pre-existing shear bands on the tensile mechanical properties of a bulk metallic glass. *Acta Materialia*, 58(4):1276–1292, 2010.

[148] S. Scudino, B. Jerliu, K.B. Surreddi, U. Kühn, and J. Eckert. Effect of cold rolling on compressive and tensile mechanical properties of Zr52.5Ti5Cu18Ni14.5Al10 bulk metallic glass. *Journal of Alloys and Compounds*, 509:S128–S130, June 2011.

[149] David A Muller. Structure and bonding at the atomic scale by scanning transmission electron microscopy. *Nature Materials*, 8(4):263–270, 2009.

[150] Paul A Midgley and Rafal E Dunin-Borkowski. Electron tomography and holography in materials science. *Nature Materials*, 8(4):271, 2009.

[151] Franz J Giessibl. Advances in atomic force microscopy. *Reviews of Modern Physics*, 75(3):949, 2003.

[152] Ian Robinson and Ross Harder. Coherent x-ray diffraction imaging of strain at the nanoscale. *Nature Materials*, 8(4):291–298, 2009.

[153] Marcus C Newton, Steven J Leake, Ross Harder, and Ian K Robinson. Three-dimensional imaging of strain in a single zno nanorod. *Nature Materials*, 9(2):120–124, 2010.

[154] Vikram Prasad, Denis Semwogerere, and Eric R Weeks. Confocal microscopy of colloids. *Journal of Physics: Condensed Matter*, 19(11):113102, 2007.

[155] Lawrence Bragg and J. F. Nye. A dynamical model of a crystal structure. *Proceedings of the Royal Society of London. Series A, Mathematical and Physical Sciences*, 190(1023):pp. 474–481, 1947.

[156] Lawrence Bragg. A model illustrating intercrystalline boundaries and plastic flow in metals. *Journal of Scientific Instruments*, 19(10):148, 1942.

[157] AW Simpson and Pauline H Hodkinson. Bubble raft model for an amorphous alloy. *Nature*, 237:320–322, 1972.

[158] PN Pusey and W Van Megen. Phase behaviour of concentrated suspensions of nearly hard colloidal spheres. *Nature*, 320(6060):340–342, 1986.

[159] Eric R Weeks and DA Weitz. Properties of cage rearrangements observed near the colloidal glass transition. *Physical Review Letters*, 89(9):095704, 2002.

[160] KE Jensen, David A Weitz, and F Spaepen. Local shear transformations in deformed and quiescent hard-sphere colloidal glasses. *Physical Review E*, 90(4):042305, 2014.

[161] Jennifer M Rieser. *Deformation of two-dimensional amorphous granular packings.* University of Pennsylvania, 2015.

[162] Wenbin Li, Jennifer M Rieser, Andrea J Liu, Douglas J Durian, and Ju Li. Deformation-driven diffusion and plastic flow in amorphous granular pillars. *Physical Review E*, 91(6):062212, 2015.

[163] Dongchan Jang and Julia R Greer. Transition from a strong-yet-brittle to a stronger-and-ductile state by size reduction of metallic glasses. *Nature Materials*, 9(3):215–219, 2010.

[164] A.L. Greer, Y.Q. Cheng, and E. Ma. Shear bands in metallic glasses. *Materials Science and Engineering: R: Reports*, 74:71–132, 2013.

[165] Christos N Likos. Effective interactions in soft condensed matter physics. *Physics Reports*, 348(4):267–439, 2001.

[166] KM Salikhov. Kleman, m., lavrentovich, od: Soft matter physics. an introduction, 2004.

[167] Pierre-Gilles de Gennes. Granular matter: a tentative view. *Reviews of Modern Physics*, 71(2):S374, 1999.

[168] Karnail B Singh and Mahesh S Tirumkudulu. Cracking in drying colloidal films. *Physical Review Letters*, 98(21):218302, 2007.

[169] Anuraag R Kansal, Salvatore Torquato, and Frank H Stillinger. Computer generation of dense polydisperse sphere packings. *The Journal of Chemical Physics*, 117(18):8212–8218, 2002.

[170] Robert S Farr and Robert D Groot. Close packing density of polydisperse hard spheres. *The Journal of Chemical Physics*, 131(24):244104, December 2009.

[171] Andrew P. Shapiro and Ronald F. Probstein. Random packings of spheres and fluidity limits of monodisperse and bidisperse suspensions. *Physical Review Letters*, 68:1422–1425, 1992.

[172] H.A. Kuhn. *ASM Handbook, Materials Testing and Evaluation*, volume 8. ASM International, 2000.

[173] FF Wu, ZF Zhang, and SX Mao. Compressive properties of bulk metallic glass with small aspect ratio. *Journal of Materials Research*, 22(02):501–507, 2007.

[174] Michael A Sutton, Jean Jose Orteu, and Hubert Schreier. *Image correlation for shape, motion and deformation measurements: basic concepts, theory and applications.* Springer Science & Business Media, 2009.

[175] C Eberl, DS Gianola, and KJ Hemker. Mechanical characterization of coatings using microbeam bending and digital image correlation techniques. *Experimental Mechanics*, 50(1):85–97, 2010.

[176] Thompson-R. Gianola D.S. Sharpe Jr. W. Eberl, C. and K.J. Hemker. Digital image correlation and tracking. MATLAB File Exchange.

[177] M F&amp Ashby and SD Hallam. The failure of brittle solids containing small cracks under compressive stress states. *Acta Metallurgica*, 34(3):497–510, 1986.

[178] Lucio Isa, Rut Besseling, and Wilson CK Poon. Shear zones and wall slip in the capillary flow of concentrated colloidal suspensions. *Physical Review Letters*, 98(19):198305, 2007.

[179] Amy L Rechenmacher. Grain-scale processes governing shear band initiation and evolution in sands. *Journal of the Mechanics and Physics of Solids*, 54(1):22–45, 2006.

[180] Kazuyoshi Iwashita and Masanobu Oda. Micro-deformation mechanism of shear banding process based on modified distinct element method. *Powder Technology*, 109(1):192–205, 2000.

[181] CJ Lee, JC Huang, and TG Nieh. Sample size effect and microcompression of mg 65 cu 25 gd 10 metallic glass. *Applied Physics Letters*, 91(16):161913–161913, 2007.

[182] YH Lai, CJ Lee, YT Cheng, HS Chou, HM Chen, XH Du, CI Chang, Jacob C Huang, SR Jian, JSC Jang, et al. Bulk and microscale compressive behavior of a zr-based metallic glass. *Scripta Materialia*, 58(10):890–893, 2008.

[183] Francisco Gallego-Gomez, Víctor Morales-Florez, Alvaro Blanco, Nicolas de la Rosa-Fox, and Cefe Lopez. Water-dependent micromechanical and rheological properties of silica colloidal crystals studied by nanoindentation. *Nano Letters*, 12(9):4920–4924, 2012.

[184] Namiko Mitarai and Franco Nori. Wet granular materials. *Advances in Physics*, 55(1-2):1–45, 2006.

[185] Jan Schroers and William L Johnson. Ductile bulk metallic glass. *Physical Review Letters*, 93(25):255506, 2004.

[186] RT Qu, ZQ Liu, RF Wang, and ZF Zhang. Yield strength and yield strain of metallic glasses and their correlations with glass transition temperature. *Journal of Alloys and Compounds*, 637:44–54, 2015.

[187] Timothy J. Rupert. Solid solution strengthening and softening due to collective nanocrystalline deformation physics. *Scripta Materialia*, 81:44–47, June 2014.

[188] Jason R. Trelewicz and Christopher A. Schuh. The HallPetch breakdown in nanocrystalline metals: A crossover to glass-like deformation. *Acta Materialia*, 55(17):5948–5958, October 2007.

[189] Victor V. Kozey and Satish Kumar. Compression behavior of materials: Part I. Glassy polymers. *Journal of Materials Research*, 9:2717–2726, 1994.

[190] Nathan C. Keim and Paulo E. Arratia. Yielding and microstructure in a 2D jammed material under shear deformation. *Soft Matter*, 9:6222, 2013.

[191] D Deng, A S Argon, and S Yip. Simulation of Plastic Deformation in a Two-Dimensional Atomic Glass by Molecular Dynamics IV. *Philosophical Transactions of the Royal Society of London. Series A, Mathematical and Physical Sciences*, 329(1608):613–640, December 1989.

[192] J. D. Eshelby. The Determination of the Elastic Field of an Ellipsoidal Inclusion, and Related Problems. *Proceedings of the Royal Society A: Mathematical, Physical and Engineering Sciences*, 241:376–396, 1957.

[193] Toshio Mura. *Micromechanics of Defects in Solids*, volume 3. Springer, 1987.

[194] Jacques Desrues and René Chambon. Shear band analysis and shear moduli calibration. *International Journal of Solids and Structures*, 39(13-14):3757–3776, June 2002.

[195] Y. F. Gao, L. Wang, H. Bei, and T. G. Nieh. On the shear-band direction in metallic glasses. *Acta Materialia*, 59:4159–4167, 2011.

[196] A.S. Argon and L.T. Shi. Development of visco-plastic deformation in metallic glasses. *Acta Metallurgica*, 31:499–507, 1983.

[197] Eric R. Homer and Christopher A. Schuh. Mesoscale modeling of amorphous metals by shear transformation zone dynamics. *Acta Materialia*, 57(9):2823–2833, May 2009.

[198] Eric R. Homer, David Rodney, and Christopher A. Schuh. Kinetic Monte Carlo study of activated states and correlated shear-transformation-zone activity during the deformation of an amorphous metal. *Physical Review B*, 81, 2010.

[199] A. S. Argon and M. J. Demkowicz. Atomistic simulation and analysis of plasticity in amorphous silicon. *Philosophical Magazine*, 86(25-26):4153–4172, 2006.

[200] P B Bowden and S Raha. The formation of micro shear bands in polystyrene and polymethylmethacrylate. *Philosophical Magazine*, 22(177):463–482, 1970.

[201] A. S. Argon, R. D. Andrews, J. A. Godrick, and W. Whitney. Plastic Deformation Bands in Glassy Polystyrene. *Journal of Applied Physics*, 39(3):1899, 1968.

[202] Gilberto Brambilla and David N. Payne. The ultimate strength of glass silica nanowires. *Nano Letters*, 9:831–835, 2009.

[203] Dennis M Dimiduk, Chris Woodward, Richard LeSar, and Michael D Uchic. Scale-free intermittent flow in crystal plasticity. *Science*, 312(5777):1188–1190, 2006.

[204] Nir Friedman, Andrew T Jennings, Georgios Tsekenis, Ju-Young Kim, Molei Tao, Jonathan T Uhl, Julia R Greer, and Karin A Dahmen. Statistics of dislocation slip avalanches in nanosized single crystals show tuned critical behavior predicted by a simple mean field model. *Physical Review Letters*, 109(9):095507, 2012.

[205] Xinyu Zhao, Daniel J Strickland, Peter M Derlet, Mo-rigen He, You-Jung Cheng, Jue Pu, Khalid Hattar, and Daniel S Gianola. In situ measurements of a homogeneous to heterogeneous transition in the plastic response of ion-irradiated¡ 111¿ ni microspecimens. *Acta Materialia*, 88:121–135, 2015.

[206] Ferenc F Csikor, Christian Motz, Daniel Weygand, Michael Zaiser, and Stefano Zapperi. Dislocation avalanches, strain bursts, and the problem of plastic forming at the micrometer scale. *Science*, 318(5848):251–254, 2007.

[207] Karin A Dahmen, Yehuda Ben-Zion, and Jonathan T Uhl. Micromechanical model for deformation in solids with universal predictions for stress-strain curves and slip avalanches. *Physical Review Letters*, 102(17):175501, 2009.

[208] Christian Greiner, Jonathan R. Felts, Zhenting Dai, William P. King, and Robert W. Carpick. Local nanoscale heating modulates single-asperity friction. *Nano Letters*, 10:4640–4645, 2010.

[209] Robert H Webb. Confocal optical microscopy. *Reports on Progress in Physics*, 59(3):427, 1996.

[210] Alexander Stukowski et al. Visualization and analysis of atomistic simulation data with ovito–the open visualization tool. *Modeling and Simulation in Materials Science and Engineering*, 18(1):015012, 2010.

[211] John C Crocker and David G Grier. Methods of digital video microscopy for colloidal studies. *Journal of Colloid and Interface Science*, 179(1):298–310, 1996.

[212] Yongxiang Gao and Maria L Kilfoil. Accurate detection and complete tracking of large populations of features in three dimensions. *Optics Express*, 17(6):4685–4704, 2009.

[213] Minh Triet Dang, Dmitry Denisov, Bernd Struth, Alessio Zaccone, and Peter Schall. Reversibility and hysteresis of the sharp yielding transition of a colloidal glass under oscillatory shear. *The European Physical Journal E*, 39(4):1–11, 2016.

[214] SI Henderson, TC Mortensen, Sylvia M Underwood, and William van Megen. Effect of particle size distribution on crystallisation and the glass transition of hard sphere colloids. *Physica A: Statistical Mechanics and its Applications*, 233(1):102–116, 1996.

[215] Gary L Hunter and Eric R Weeks. The physics of the colloidal glass transition. *Reports on Progress in Physics*, 75(6):066501, 2012.

[216] E Bartsch, T Eckert, C Pies, and H Sillescu. The effect of free polymer on the glass transition dynamics of microgel colloids. *Journal of Non-Crystalline Solids*, 307:802–811, 2002.

[217] Morrel H Cohen and David Turnbull. Molecular transport in liquids and glasses. *The Journal of Chemical Physics*, 31(5):1164–1169, 1959.

[218] David Turnbull and Morrel H Cohen. On the free-volume model of the liquid-glass transition. *The Journal of Chemical Physics*, 52(6):3038–3041, 1970.

[219] Corinna Cortes and Vladimir Vapnik. Support-vector networks. *Machine Learning*, 20(3):273–297, 1995.

[220] R Kurita, DB Ruffner, and ER Weeks. Measuring the size of individual particles from three-dimensional imaging experiments. *Nature Communications*, 3:1127, 2012.

[221] SS Schoenholz, ED Cubuk, DM Sussman, E Kaxiras, and AJ Liu. A structural approach to relaxation in glassy liquids. *Nature Physics*, 12:469–471, 2016.

[222] Gavin C Cawley and Nicola LC Talbot. On over-fitting in model selection and subsequent selection bias in performance evaluation. *Journal of Machine Learning Research*, 11(Jul):2079–2107, 2010.

[223] Neil YC Lin, Matthew Bierbaum, Peter Schall, James P Sethna, and Itai Cohen. Measuring nonlinear stresses generated by defects in 3d colloidal crystals. *Nature Materials*, 2016.

[224] Neil YC Lin and Itai Cohen. Relating microstructure and particle-level stress in colloidal crystals under increased confinement. *Soft Matter*, 12(44):9058–9067, 2016.

[225] Dhananjay Dendukuri and Patrick S Doyle. The synthesis and assembly of polymeric microparticles using microfluidics. *Advanced Materials*, 21(41):4071–4086, 2009.

[226] Fan Li, David P Josephson, and Andreas Stein. Colloidal assembly: the road from particles to colloidal molecules and crystals. *Angewandte Chemie International Edition*, 50(2):360–388, 2011.

[227] Sawyer B Fuller, Eric J Wilhelm, and Joseph M Jacobson. Ink-jet printed nanoparticle microelectromechanical systems. *Journal of Microelectromechanical Systems*, 11(1):54–60, 2002.

[228] Martin Heule, SGLJ Vuillemin, and Ludwig J Gauckler. Powder-based ceramic meso-and microscale fabrication processes. *Advanced Materials*, 15(15):1237–1245, 2003.

[229] Masaru Palakurthi Rao, AJ Sanchez-Herencia, GE Beltz, RM McMeeking, and FF Lange. Laminar ceramics that exhibit a threshold strength. *Science*, 286(5437):102–105, 1999.

[230] John H Holtz, Janet SW Holtz, Calum H Munro, and Sanford A Asher. Intelligent polymerized crystalline colloidal arrays: novel chemical sensor materials. *Analytical Chemistry*, 70(4):780–791, 1998.

[231] Guang Lu, Omar K Farha, Lauren E Kreno, Paul M Schoenecker, Krista S Walton, Richard P Van Duyne, and Joseph T Hupp. Fabrication of metal-organic framework-containing silica-colloidal crystals for vapor sensing. *Advanced Materials*, 23(38):4449–4452, 2011.

[232] André C Arsenault, Daniel P Puzzo, Ian Manners, and Geoffrey A Ozin. Photonic-crystal full-colour displays. *Nature Photonics*, 1(8):468–472, 2007.

[233] Jonathan S Lindsey. Self-assembly in synthetic routes to molecular devices. biological principles and chemical perspectives: a review. *New Journal of Chemistry*, 15(2-3):153–179, 1991.

[234] Jiyun C Huie. Guided molecular self-assembly: a review of recent efforts. *Smart Materials and Structures*, 12(2):264, 2003.

[235] Andreas Walther and Axel HE Muller. Janus particles: synthesis, self-assembly, physical properties, and applications. *Chemical Reviews*, 113(7):5194–5261, 2013.

[236] James E Smay, Joseph Cesarano, and Jennifer A Lewis. Colloidal inks for directed assembly of 3-d periodic structures. *Langmuir*, 18(14):5429–5437, 2002.

[237] Jennifer A Lewis. Direct ink writing of 3d functional materials. *Advanced Functional Materials*, 16(17):2193–2204, 2006.

[238] Rachel R Collino, Tyler R Ray, Rachel C Fleming, Camille H Sasaki, Hossein Haj-Hariri, and Matthew R Begley. Acoustic field controlled patterning and assembly of anisotropic particles. *Extreme Mechanics Letters*, 5:37–46, 2015.

[239] Rachel R Collino, Tyler R Ray, Rachel C Fleming, James D Cornell, Brett G Compton, and Matthew R Begley. Deposition of ordered two-phase materials using microfluidic print nozzles with acoustic focusing. *Extreme Mechanics Letters*, 8:96–106, 2016.